Experimental Investigation of Wheelhouse flow using PIV

Sai Krishna Ramani

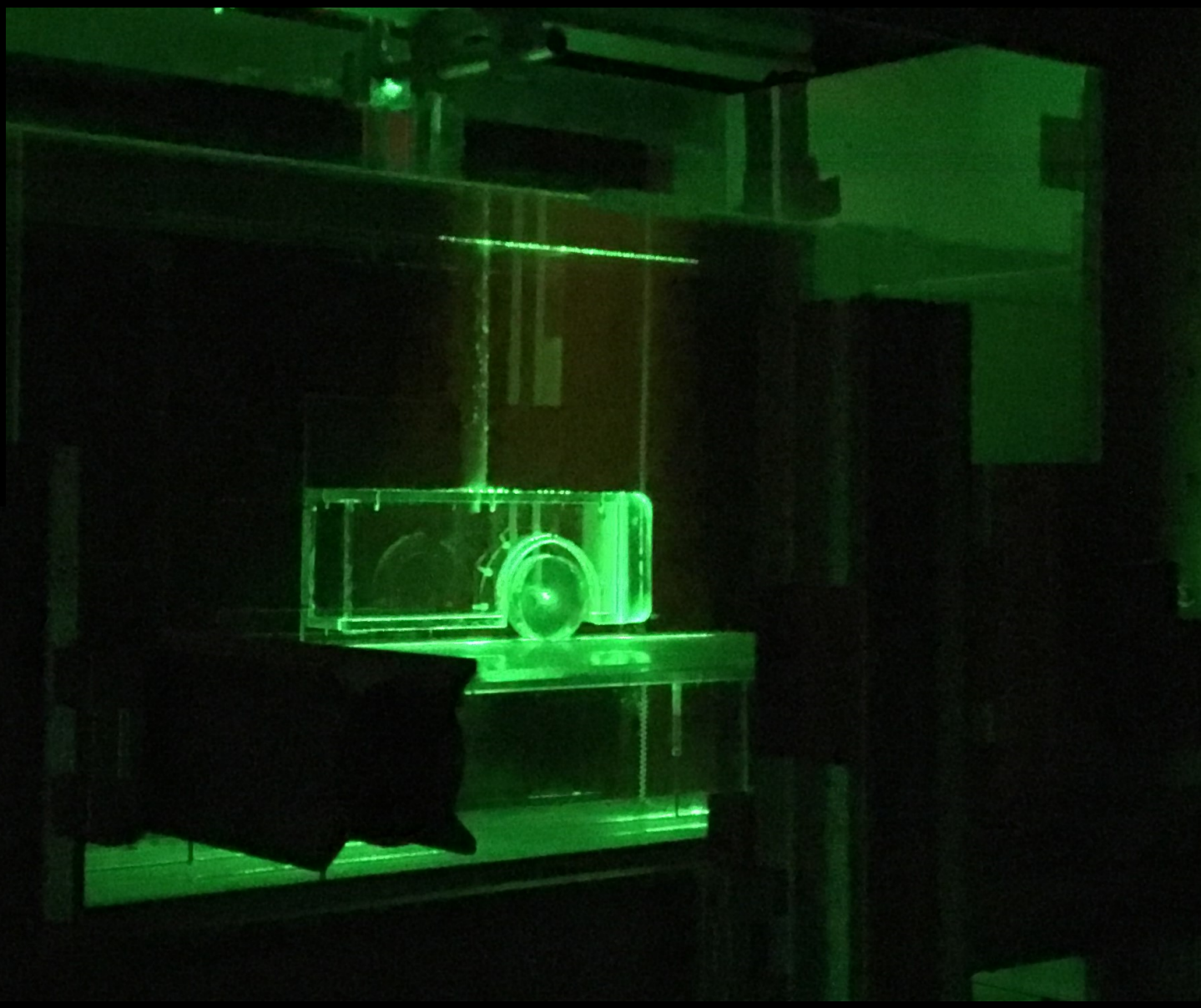

Technische Universiteit Delft

Experimental Investigation of Wheelhouse flow using PIV

by

Sai Krishna Ramani

in partial fulfillment of the requirements for the degree of

Master of Science
in Mechanical Engineering

at the Delft University of Technology,
to be defended on Monday January 15, 2018 at 02:00 PM.

P & E Report Number : 2872

Supervisors:	Dr. ir. G.E. Elsinga	TU Delft
	Dr. ir. M.J.B.M. Pourquie	TU Delft
Thesis committee:	Prof. dr. ir. J. Westerweel,	TU Delft
	Dr. A. Sciacchitano,	TU Delft

TU Delft Delft University of Technology

Acknowledgments

I would like to thank my supervisors *Dr. Gerrit Elsinga* and *Dr. Mathieu Pourquie* for giving me an opportunity to pursue a thesis under them. Thank you for being approachable and for your guidance during this thesis. Thank you also for taking the time to proofread my thesis and provide feedback on it. Furthermore, I would like to thank *Prof. Jerry Westerweel* and *Dr. Andrea Sciacchitano* for agreeing to be part of my thesis defence.

I am also deeply grateful to the support staffs whose assistances were a big factor in the completion of this thesis. *Jasper Ruijgrok*: Thank you for fabricating the model for me and helping me in the initial stages of the experimental setup. *Jan Graafland*: Thank you for ordering the driving belt and helping me in setting up of the motor. *Edwin Overmars*: Thank you for your guidance in the setup of my experiments and for sharing your knowledge related to PIV measurements.

I would like to thank my friends *Veera*, *Naren*, *Keerthi* and *Antaran* for their support during this thesis and for all the fun I had with them along with *Adi*, *Vaibhav* and *Digjivay*. Finally, none of this would have been possible without my parents. Thank you for your love, encouragement and support.

Sai Krishna
Delft, January 2018

Abstract

Aerodynamics has become increasingly important these days in the design of automobiles due to the increased constraints placed on the emissions. In the past the focus has been primarily on the shaping of the upper body. However, due to practical requirements, further scope of improvements to the upper body has been greatly reduced. The focus has thus shifted towards the optimization of the underbody which includes the wheel and the wheelhouse. The contribution of the wheel and the wheelhouse to the total drag and lift coefficient of a body has been estimated at 30% and 40% respectively. Therefore, understanding the behavior of the flow in the wheelhouse would potentially result in reducing the drag coefficient of an automobile.

In the present study, the wheelhouse flow has been investigated experimentally using Particle Image Velocimetry (PIV). A generic simplified car body with a wheel and a wheelhouse has been designed and used for this purpose. The study has been done for a rotating wheel and stationary ground configuration. Planar PIV and Stereo PIV have been used to study the flow inside the wheelhouse and in the wake of the wheel respectively. The study was undertaken for the Reynolds number, based on wheel diameter, of 9000 and 72000. Measurements were taken at planes inside and outside the wheelhouse as well as upstream and downstream of the wheel. In addition to providing data for the Large Eddy Simulation (LES), the results from the PIV measurements showed that the behavior of the flow depended on the Reynolds number. Velocity profiles in the wake of the wheel highlighted a three dimensional flow in the wheelhouse.

Finally, the effect of a Vortex Generator (VG) on the flow was investigated. The VG was found to have an effect at the low Reynolds number wherein the flow inside the wheelhouse and in the underbody was found to be quite different compared to the configuration without a VG.

Contents

List of Figures

List of Tables

Chapter 1

Introduction

1.1 Background

Automobiles have evolved quite a lot since the time the first car was made. They have taken on several shapes and forms depending on the purposes they were intended for. A common objective for the designers is to minimize the aerodynamic forces acting on the automobile. This is because, the aerodynamic loads acting on an automobile can be quite significant.

The main aerodynamic forces acting on an automobile are the drag and the lift force. The magnitude of these forces acting on an automobile determines the performance. For example, in a passenger car, if the drag force is high, a lot of power is required to overcome this force, which results in a poor fuel efficiency. Similarly for a racing car the drag force can severely affect the top speed that can be achieved by the vehicle. The same applies for the lift force. The lower the lift force, or in other words, the higher the downforce, the more the automobile stays planted on the road in a straight line at high speeds while also enabling higher cornering speeds.

The mechanism by which these aerodynamic forces act are through the pressure and shear stress distribution over the entire surface of the body. Typically for an automobile, the contribution to the aerodynamic force from pressure far exceeds the shear stress contribution [1]. The distribution is such that the pressure at the front surface of the body is higher compared to the base surface of the body. This creates a net force in the direction of the flow which is referred to as the drag force. The lower pressure one the base surface is due to flow separation at the surface of the body. The flow separation is a consequence of an adverse pressure gradient in the direction of flow or a sharp corner of the surface. When the adverse pressure gradient is sufficiently large, the flow is unable to remain attached to the surface and eventually separates from it. The separated region consists of reverse flow and the region of recirculating flow behind a body is commonly referred to as the wake region. Similarly for the lift force, the pressure is higher on the lower body surface relative to the upper body surface. By changing the pressure distribution on the surface of the body, we can minimize the aerodynamic forces acting on the body. This change could be brought about either by reducing the pressure at the front surface of the body or increasing the base surface

pressure, for drag reduction and likewise for lift reduction. A reduction in these forces would translate into either higher savings in terms of fuel costs by achieving better fuel efficiency or a faster car in motorsports. However, in order to propose changes such that the pressure distribution is altered favorably, it is important to have a good understanding of the flow in the region of interest.

Aerodynamicists do not deal with these forces directly. Rather, these forces are represented through aerodynamic coefficients namely drag (c_D) and lift (c_L) coefficient shown in Equation, which are non-dimensional quantities that allows one to compare the design between different models. Despite a lot of progress in the area of aerodynamic drag reduction, the drag coefficient of the total vehicle has plateaued, on an average, at around 0.3 [2].

$$C_D = \frac{D}{\frac{1}{2}\rho U_\infty^2 A} \tag{1.1}$$

$$C_L = \frac{L}{\frac{1}{2}\rho U_\infty^2 A} \tag{1.2}$$

where D is the drag force, L is the lift force, ρ is the density of the fluid, U_∞ is the velocity of the vehicle and A is frontal surface area of the vehicle.

1.1.1 Wheelhouse Aerodynamics

As mentioned earlier, aerodynamics plays an important role in the design of automobiles. With increasing restrictions being placed on emissions, any potential gain in terms of minimizing the aerodynamic forces is worth exploring. In the past, the focus has primarily been on shaping the upper body without much attention given to the underbody. However, due to practical requirements, further scope of improvement to the upper body has been greatly reduced.

It is estimated that the underbody, which includes the wheel and the wheelhouse, accounts for 50% of the total drag acting on the vehicle [3]. The wheel and the wheelhouse alone contribute to 30% of the total drag [4]. In terms of lift, the contribution of the wheel and wheelhouse is around 40% [4]. The main reason for the large amount of drag and lift is because of the energy loss in the underbody flow occurring due to various flow structures forming in and around the wheel and the wheelhouse. It is evident from these estimations that there are potential gains possible in this region of the vehicle.

The contribution of the wheel and wheelhouse to the overall drag and lift of a body is dependent on many factors such as the geometry of the wheelhouse, profile of the tire among others. Several investigations have been done in the past, both experimentally and numerically, in the region around the wheel and the wheelhouse to understand the mechanisms that contribute to such large amount of drag and lift. However, it still remains to be fully understood. The difficulty arises in recreating the conditions experienced by the wheel in an actual environment either due to wind tunnel restrictions or inaccurate CFD models. Additional challenges involve recreating the contact patch

between the wheel and the road, including components such as wheel rim, suspension systems, inlet for engine cooling etc., which add complexities in simulating it. The problem is even more compounded when simulating numerically due to meshing issues especially, at the contact patch and the high resolution that is required to capture the flow features. The computational resources thus required rises rapidly.

Large Eddy Simulation (LES) has recently become a suitable method to study the structure of the flow field numerically for its capability in resolving the flow features. However to simulate a condition that is representative of the actual car, the computational resources required are tremendous, which places a restriction on the Reynolds number that could be simulated.

As is the case for any CFD simulation and particularly those involving turbulence modeling, experimental data is required to ensure the validity of the results. This experimental data for the wheelhouse flow is lacking presently, atleast in the open literature. It is therefore decided, in this thesis, to investigate experimentally, a simplified geometry with wheel and wheelhouse in order to obtain an understanding of the basic flow features. This could then be used to validate LES and also serve as a reference case for future studies.

The context for the present investigation apart from the potential gains available, as mentioned earlier, is the mismatch in the wheel torque values between the numerical simulation and the on-track data experienced by the Nuon Solar Team of TU Delft. Although the geometry used by them is completely different from the present simplified geometry, the objective is to obtain a basic understanding of the flow features and shed some light on the phenomena occurring in the wheelhouse while simultaneously providing experimental data to validate LES.

1.1.2 Add-ons: Vortex Generators

One of the means of reducing the aerodynamic forces acting on a body is through the use of add-on devices. Their function is to alter the flow conditions favorably resulting in a reduction in drag and lift. There are many add-on devices that are commonly used in the automobile industry (spoilers, gurney flaps etc. [5]) with vortex generators being one of them.

Vortex generators (VGs) are simple devices that are attached to a body. It has been primarily used to control boundary layer separation and can be seen on wings of aircrafts and also on the rear of a passenger car body. However, it could also be used in the underbody although in this case its intended purpose is not to control boundary layer separation, rather create a vortex that induces low pressure in the downstream section of the vortex generator [5].

In the present study Vortex Generators are used. The idea is to position these upstream of the wheel, near the entry to the wheelhouse, such that vortices are shed with the objective of reducing the pressure in front of the wheel thereby reducing the drag force acting on it. Since pressure measurements are not acquired in the present study, the effect of the VG on the flow will be studied by comparing the flow field between the configuration with and without the VG. The particular focus is on the vortices shed

from the wheel contact patch (the point of contact of the wheel with the ground) as these are, as will be discussed in the next chapter, a major source of drag on the wheel.

1.1.3 Objectives

In this thesis, the flow around a wheel in a wheelhouse is studied experimentally using Particle Image Velocimetry (PIV). The objectives of the present study are:

(i) to design and fabricate a simplified car body with a wheel and a wheelhouse along with a ground plane

(ii) to investigate the flow field in the region around the wheel and in the wake of the wheel and provide experimental data for the validation of Large Eddy Simulation (LES)

(iii) to study the effect of a Vortex Generator located upstream of the wheel on the flow field.

1.1.4 Outline

The structure of this thesis is as follows: Chapter 2 provides a detailed literature review related to the aerodynamics of isolated wheels and a wheel in a wheelhouse. The flow mechanisms observed so far in the literature will be discussed in this chapter. Chapter 3 describes the experimental setup and methodology used for the present study. The results of the experimental investigation are presented and discussed in Chapter 4. This includes the basic flow field and the effect of the addition of a VG. This is followed by the conclusions and the recommendations for future study in Chapter 5.

Chapter 2

Literature Review

This chapter provides a review of the studies conducted, both experimentally and numerically, on an isolated and shrouded wheel (wheel inside a wheelhouse) under rotating and stationary configurations. Through this, the behavior of the flow and the differences between different configurations can be understood.

2.1 Isolated Wheels

Before dwelling into the studies on a wheel in a wheelhouse, the isolated wheel is a simplified case that provides a basic understanding of the flow phenomenon occurring around a wheel. The major difficulty encountered by people investigating the flow around a wheel is in recreating the contact patch between the tire and the ground accurately especially when the ground is moving. The very initial studies conducted in this area involved either a small gap between the wheel and the ground or sealing these gaps using appropriate materials. The results obtained from these measurements were inaccurate with some observing downforce due to the gap, when in theory a lift is expected. It also became difficult to quantify the extent of these errors.

Fackrell and Harvey [6] were the first experimentalists to be successful in recreating the actual conditions. Their experimental setup included pressure taps located in the centerline of the wheel allowing them to provide force data through pressure integration. The experiments were conducted at a Reynolds number of 2.0 x 10^5 for two different edge profiles of the wheel. They observed different pressures at the base of the wheel for the two profiles, suggesting the influence the tire profile has on the pressure distribution on the wheel. This is shown in Figure 2.1, indicated by the legend 'Wheel 1' and 'Wheel 2'.

The most striking feature observed was the sharp rise in the pressure coefficient in front of the contact patch (C_p >1) as shown in Figure 2.1. Fackrell and Harvey attributed this rise to the strong viscous action and stated that it is only valid in a small region near the contact patch where the viscous forces are dominant. The fluid is then forced out by the two converging boundaries (ground and wheel) to the downstream region along the side of wheel. This phenomenon is commonly referred to as the 'jetting effect'.

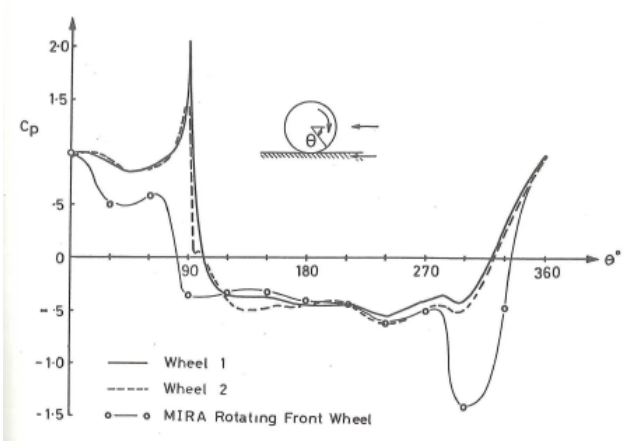

Figure 2.1: C_p distribution along the centerline of rotating wheel obtained by Fackrell and Harvey [6]. The flow is from right to left with the contact patch located at 90°.

The experiments were also performed for stationary wheels. The main differences observed were lower pressures both in front of the contact patch and in the base region of the wheel for the stationary wheel. They explained the lower pressures as a direct consequence of absence of the rotation and the boundary layer being attached to the wheel for much larger angles. This shows that the jetting effect is present only in the case of rotating wheels. Also, in the case of a rotating wheel, the direction of rotation is opposite to that of freestream fluid over the top of the wheel. This causes earlier boundary layer separation unlike for a stationary wheel, where it remains attached for a much larger angle. Since the separation occurs much later for a stationary wheel compared to a rotating wheel, a greater suction effect is observed in a stationary wheel, leading to higher lift compared to a rotating wheel.

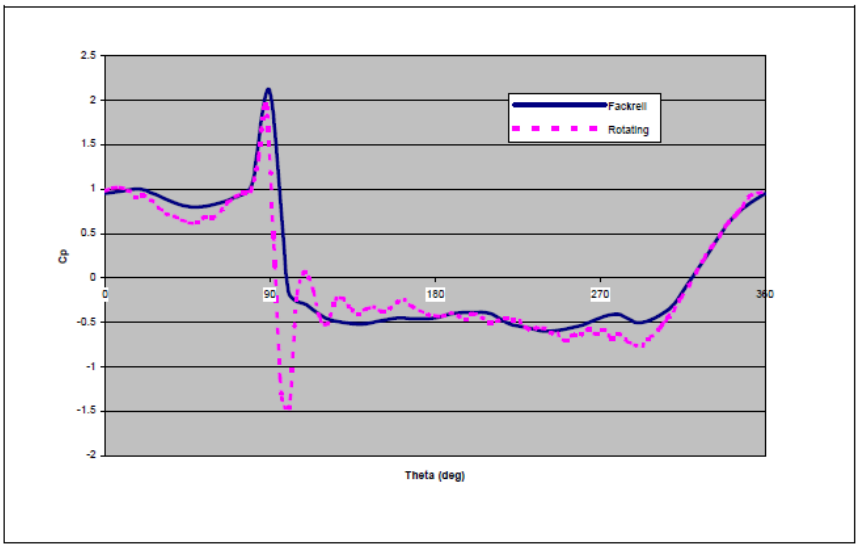

Figure 2.2: C_p distribution along the centerline of rotating wheel obtained by Mears et al [7].

Mears et al. [7] conducted an experimental investigation on an isolated racing wheel with a specially designed radio telemetry system, to transfer the pressure data from the wheel to a PC. The results showed good agreement with those of Fackrell and Harvey.

They were also able to observe the negative pressure peak immediately following the contact patch that Fackrell and Harvey had postulated but did not observe. This is shown in Figure 2.2. It can be seen that the pressure behind the contact patch does not fully recover to the value ahead of the contact patch resulting in a net pressure force against the direction of moving vehicle. Thus, this region is a major source of drag on the wheel.

2.1.1 Flow field description

A description of the vortex structures formed in the case of a stationary isolated wheel and a rotating isolated wheel was provided by Wäschle [8] as shown in Figure 2.3. The dominating vortex for the stationary isolated wheel was identified as the wake horseshoe vortex (① in Figure 2.3 (left)), which is primarily responsible for the higher drag in stationary exposed wheels. The flow along the side of the wheel was found to provide energy to the flow coming from the top of the wheel creating a strong downwash region behind the tire which, upon impinging the ground forms a counter-rotating vortex pair behind the tire [9]. This vortex was found to be significantly reduced in the presence of wheel rotation. In this case, the wheel rotation causes earlier separation near the top of the wheel and the flow along the side of the wheel is unable to provide sufficient energy to the flow coming from the top of the wheel, resulting in a weaker vortex.

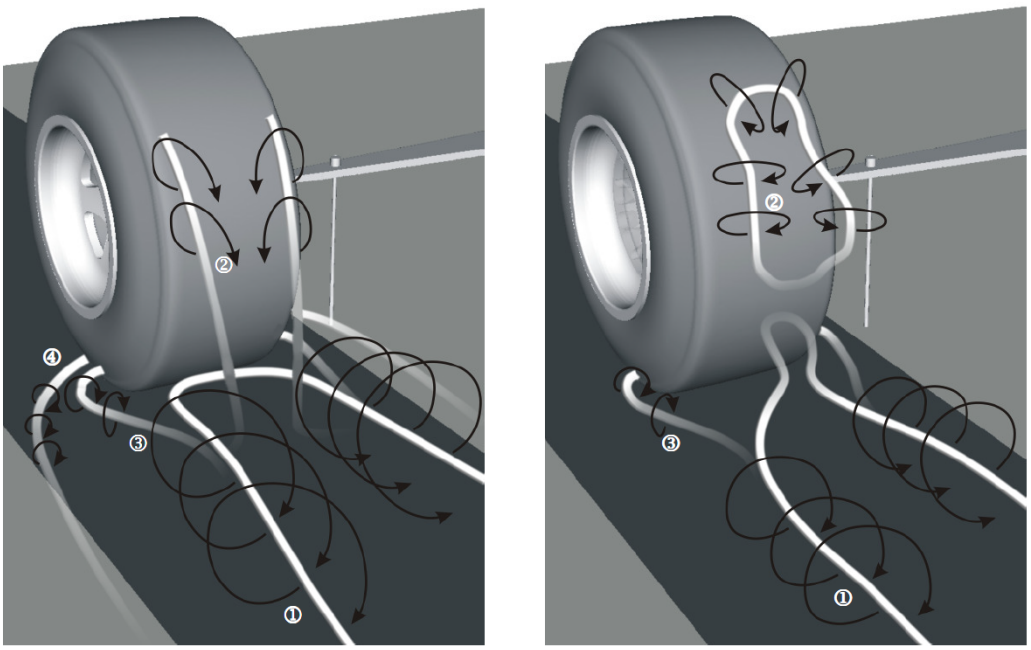

Figure 2.3: Vortex structures in stationary isolated wheel (left) and rotating isolated wheel (right)

.

Another pair of vortices can be seen in the upper rear half of the tire (② in Figure 2.3 (left)) formed due to the flow separation from the shoulder of the tire. Due to the suction created by the low pressure region behind the wheel, flow along the side of

wheel gets entrained, resulting in separation along the tire shoulders [10]. It is reasoned by these authors that these vortices cause acceleration of the flow at the top of wheel by keeping the flow attached. This local acceleration is responsible for the higher lift observed in stationary isolated wheel compared to the rotating isolated wheel. However, when the wheel is rotating, this vortex pair is formed from the tire tread rather than the tire shoulder increasing both the base pressure and pressure at the top, consequently reducing the drag and lift. However Saddington et al. [11] and Axerio [9] have shown that these upper vortices are also formed from the shoulders themselves rather than the tread, similar to the stationary case.

Besides these, a vortex pair is also formed near the contact patch ((③ in Figure 2.3 (left)) in both the stationary and rotating cases although the 'jetting' phenomena, mentioned earlier, is present only in the case of rotating tire. In the stationary tire, these vortices are formed due to the inability of the flow to follow the contour of the tire. In the rotating tire, these vortices are formed as a result of the convergence of two boundaries, which squeezes the air and pushes it towards the sides. The smaller size of these vortices for the rotating tire is a result of the additional energy being added to the flow by the rotation of the tire.

Finally, another vortex that is observed only for the stationary tire is the horseshoe vortex in front of the contact patch (④ in Figure 2.3 (left)). The structure of this vortex has been explained by Axerio et. al [9] in their LES simulation on a stationary tire as shown in Figure 2.4. The head of this vortex was found to be squeezed down due to the flow impinging the tire in front of the contact patch, with the legs extending far along the side of the wheel as can be seen in Figure 2.3 also. The legs were also found to be lifting upwards due to the presence of the counter-rotating vortex pair behind the tire, which had an upward velocity away from the side of the wheel. This was, however, not observed in the case of a rotating tire.

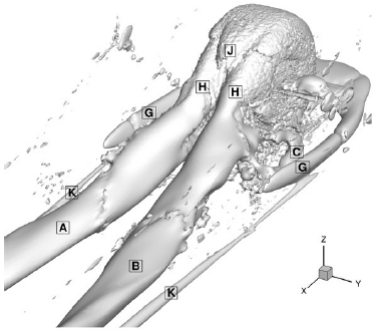

Figure 2.4: Iso-surfaces of vortex structures identified in the LES simulation on a stationary isolated wheel by Axerio et.al [9]. The structure labelled 'G' is the horseshoe vortex identified only for a stationary isolated wheel

.

2.1.2 Wake region

A few authors also studied the wake of an isolated tire to understand the dynamics of the vortices shed at the tire. Mears et al. [7] made observations comparing the

wake for both the stationary and rotating tire. The observations revealed that the ground vortices were lower and wider for the stationary tire, compared to a higher and narrower vortices for the rotating tire. This difference was mainly due to the upwash effect created by the rotation of the tire, which lifted the wake upwards and the additional energy imparted by the wheel rotation resulted in a narrower wake. Also, the presence of a strong horseshoe vortex behind the stationary tire contributed to a wider wake region.

Saddington et al. [11] observed that the counter-rotating vortices near the ground were much larger and well defined than the upper vortices shed from the shoulder of the tire. The upper vortices were also found to merge with the counter-rotating vortices near the ground, within 1d (where d is the wheel diameter) downstream of the wheel axis.

2.1.3 Deformation and Hub effect

Apart from the idealized tire geometry, a few investigations have also been conducted on non-idealized geometry which includes hubs, brake assembly, tire deformation etc. Saddington et al. [11] performed Laser Doppler Anemometry (LDA) on an isolated tire which included a hub similar to the one used in Formula One, a brake rotor and suspension. They did not observe any vortices shed from the hub that were postulated in the literature.

In another investigation conducted by Axerio et al. [9], an entire brake assembly was added to the isolated wheel that also allowed the air to pass through the hub. This resulted in the weakening of the outboard vortex pair near the ground, due to the additional mass flow exiting through the hub. Issakhanian et al. [12] investigated experimentally, using PIV, the flow around a Formula One tire that included full race geometry including hubs, brakes and cooling passages. The tire used was also deformable unlike previous investigations. The deformation was achieved through appropriate loading to recreate typical racing conditions. The counter-rotating pair of vortices near the ground was heavily affected due to the flow through the ducts from inboard to outboard direction, causing the size of the inboard vortex pair to be larger than the outboard vortex. The upper vortex pair observed in the previous investigations remained. The effect of deformation of the tire was not discussed in this work, but Sprot et al. [13] showed, in his experimental study, that higher levels of deformation result in smaller wake structures and vice-versa. In their study, tire deformation was achieved by setting the axle height.

2.2 Shrouded Wheels

The addition of a wheelhouse to a wheel increases the overall complexity of the system of vortices compared to the case of an isolated wheel. As a result, there is a significant change to the drag and the lift force of the vehicle through the addition of wheelhouse. This section deals with the past studies undertaken on shrouded wheels to provide an understanding of the flow behavior.

Studies have been performed on shrouded wheels to investigate the effect of a wheelhouse on the total drag and lift force of a body. Compared to an isolated wheel, it has been found that a shrouded wheel experiences less drag and lift [14]. In a comparison between stationary and rotating shrouded wheels, the drag acting on the rotating wheel was found to be higher than that of the stationary wheel [15]. However, the drag of the body increases when wheel and wheelhouse are added [16]. Although the stationary wheel experiences less drag than the rotating wheel, the total drag on the body is less in the case of a rotating wheel compared to a stationary wheel. Eloffson et. al [17] explained the mechanism for the reduction in drag of a vehicle due to wheel rotation and moving ground. The main cause was identified to be the interference of the wake from the rear wheel with the wake of the vehicle itself. It was thus established that achieving wheel rotation is important for any investigation on the drag acting on a vehicle. Another observation by Eloffson et al. [17] was that ground simulation alone without wheel rotation had only a small impact on the drag of the total vehicle highlighting the dominant role played by wheel rotation.

Axon [18] also provided information about the pressure distribution inside the wheelhouse cavity as well as on the surface of the wheel itself. The pressure coefficients were such that, on the front face of the wheelhouse they were negative and increased to positive values on the rear face of the wheelhouse. Negative pressures were also observed at the top of the wheelhouse. The pressure distribution on the front face of wheelhouse for the stationary wheel was identical to the rotating wheel. The pressures on the rear face of the wheelhouse, however, were found to be much higher in the stationary wheel compared to the rotating wheel. As for the pressure distribution around the wheel surface, he found the pressure coefficient at the wheel centerline to be greater than 1 in front of the contact patch similar to the isolated wheel. Away from the centerline the pressure coefficient distribution were much lower near the contact patch, however they were more identical beyond the upstream point of the wheel (90°) as shown in Figure 2.5.

2.2.1 Flow field description

Regert and Lagos [4] provided a detailed description of the flow field inside a wheelhouse using RANS and URANS modelling as shown in Figure 2.6. The representation of the averaged vortex structures shown in the figure was obtained through the use of a vortex skeleton model. As can be seen in the figure, there are two vortices, L and R, that are formed near the ground. These are the jetting vortices that have been discussed before. A vortex is formed due to flow separation at the leading edge of the wheelhouse. This is shown as 'H' in the figure. It was observed that the sense of rotation of this vortex is in the same direction as that of the wheel.

At the upstream edge of the wheelhouse, vortex C was found to develop. This vortex separates at a higher point along the upstream edge and upon interaction with the side flow is deflected in the direction of the flow. The flow along the inner side of the wheel is deflected downwards by the wheelhouse in the downstream section and separates along the downstream inner edge of the wheel. The vortex 'E' is thus formed and it continues along the underbody and towards the wake region of the wheel.

The flow entering the wheelhouse is in the direction opposite to the rotation of the

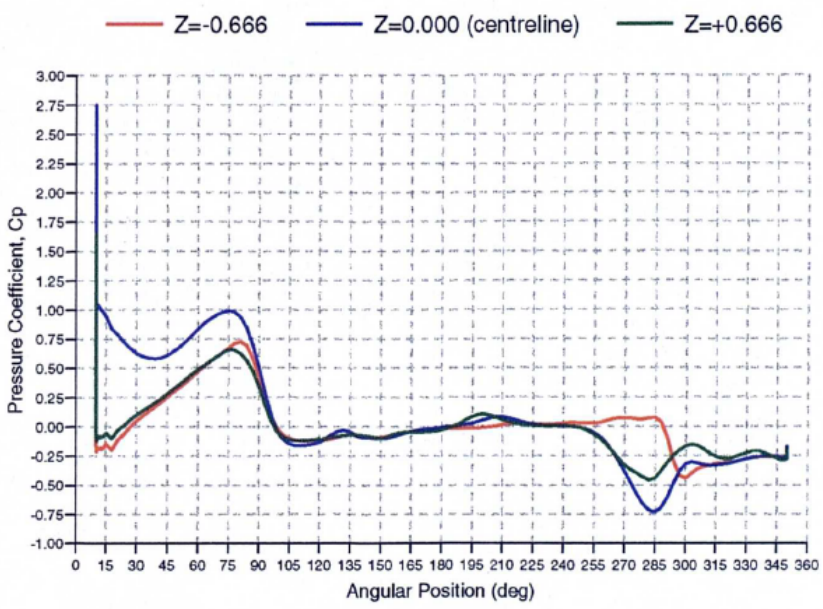

Figure 2.5: Pressure coefficient distribution around the wheel surface [18]. The angular notation is such that the contact patch is at 90^0 and measured clockwise.

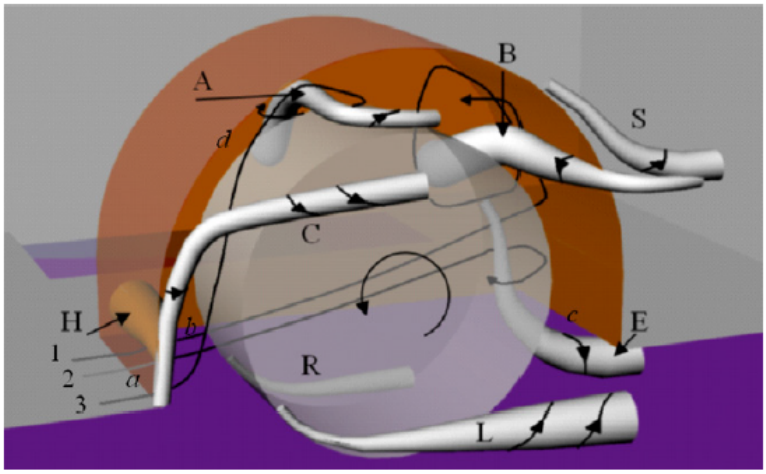

Figure 2.6: Main vortices observed in wheelhouse flow field by Regert and Lajos [4].Flow is from left to right

wheel. As a result, separation occurs over the upper part of the wheel. The vortex thus formed, 'A', was found to move towards the inner part of the wheelhouse and upon encountering the inner wall flows in the opposite direction to the side of the model. This is then deflected along the side of the model, towards the rear of the vehicle body in the direction of outside flow.

The flow along the inner part of the wheel could also be deflected upwards in the downstream part of the wheelhouse. This creates a recirculation zone, which forms the vortex 'B'. The sense of rotation of this vortex was also found to be the same as that of the rotation of wheel. The authors mentioned that the existence of this vortex depended on the presence of the wheel axis.

Outflow occurs between the wheel and wheelhouse in the downstream part of the wheelhouse. Due to flow separation at the downstream edge, vortex S is formed. The size of this vortex was found to be depended on the presence of vortex B. Similarly, vortices A and B were found to depend on the flow conditions. In the presence of yaw, defined as the outward deflection of the incoming flow with respect to the freestream, Vortex B was found to predominate over Vortex A, which became negligible. In the absence of yaw, vortex A was found to predominate over vortex B.

Krajnovic et al. [19] also provided a description of the flow within the wheelhouse using LES. In a representation similar to Regert and Lajos [4], shown in Figure 2.7, they also observed the same vortices shown in Figure 2.6, but with the addition of two vortices near the ground namely L_1 and R_1. The detection of these vortices can be attributed to the higher temporal resolution possible under LES. The direction of rotation of these vortices was observed to be opposite to that of the ground vortices L and R.

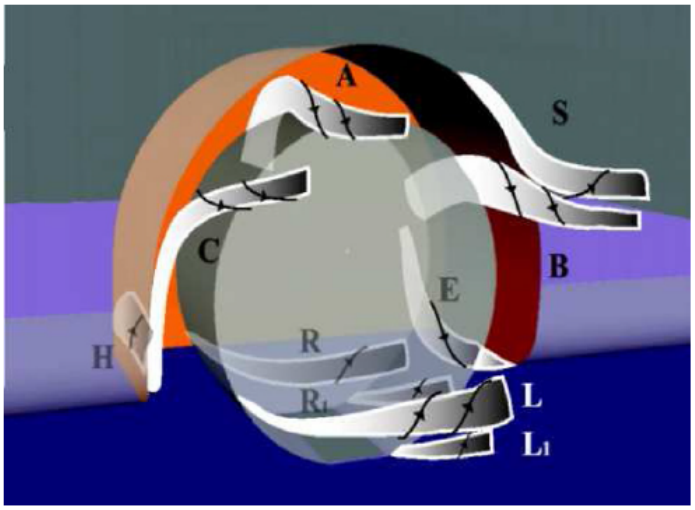

Figure 2.7: Description of the flow field inside a wheelhouse through LES by Krajnovic [19]

2.2.2 Drag reduction mechanisms

The drag acting on the wheel and wheelhouse can be reduced favorably, as mentioned earlier, through the use of add-on devices like wheel spoilers among others. These devices are typically placed in front of the wheels. Axon et al. [18] observed that the addition of a wheel spoiler leads to significant reduction in the wheel drag. The lowest wheel drag was achieved for the configuration of maximum wheel spoiler height. The mechanism for the reduction in the drag was explained by Dimitriou and Klussmann [14] who investigated the forces acting on both enclosed and exposed rotating wheels and used a wheel spoiler for the enclosed wheel configuration to determine its effect on the flow field. The favorable effect on the aerodynamic forces through the use of wheel spoiler was due to the formation of a vortex from the tip of the spoiler, referred to as 'spoiler-tip vortex' in their work, which induced underpressure behind it affecting

the flow pattern into the wheelhouse. This effect translated directly into the lower pressures around the centerline of the wheel compared to the configuration without the wheel spoiler.

Schwarczkopf [20] also investigated the effect of these add-on devices on the forces acting on the body. These devices included baffles, trapezoidal shaped vortex generators and wheel spoilers. The baffles were positioned in front of both the front and rear wheels. But it was observed that the drag acting on the front wheelhouse increased while decreasing the drag slightly on the rear wheelhouse. However the overall impact on the body was negligible. Similarly, with the use of trapezoidal shaped vortex generators, an increase in drag on the wheelhouse and wheel was observed, but the authors mention that through appropriate positioning of the vortex generator the drag could be improved.

Another means of favorably impacting the aerodynamic forces acting on the wheels is through the opening of the rims in the wheel. Schwarczkopf [20] found this configuration to have the most significant effect on the aerodynamic forces acting on the body. The configuration worked best in the presence of yawed flow. The authors explain this effect by noting that the area perpendicular to the flow direction is reduced under yaw making the flow more streamlined. The effect is similar to the case of flow through a hub observed in an isolated wheel. However, the authors also state that in the presence of yawed flow the rear wheel should have no rim opening to maximize the reduction in the aerodynamic forces.

2.2.3 Parameters influencing flow field

The flow inside the wheelhouse is highly sensitive and is dependent on several parameters such as the radius and depth of the wheelhouse and the wheel width among other things. Variation of these parameters has been found to have different effects on the aerodynamic forces. A few studies have been conducted to determine the effect of such parameters and these will be presented here.

Fabijanic [16] conducted an experimental study on wheelhouse flows investigating the effect of wheelhouse depth and radius on the flow field. The wheelhouse radius seemed to affect predominantly the drag over the lift with the wheelhouse depth having the opposite effect. Skea et al. [3] investigated the influence of wheel width on the flow characteristics and observed the pressure distribution on the centerline of the wheel to be dependent on the wheel depth. The wheel width also had an effect on the vortices formed, with their size reducing with an increase in wheel width at a plane immediately behind the wheel.

Similarly, Mavuri and Watkins [2] conducted an extensive parametric study on the effect of wheelhouse shape on the performance of a vehicle using CFD. The main observations for the front wheelhouse were that a clearance gap around the wheel, except at the top, would aid in drag and lift reduction. Skirting around the front wheelhouse improves the aerodynamic performance of the entire vehicle. A higher projection of body in front of the wheel was found to lower the drag. Positioning the wheel into the wheelhouse cavity was found to be effective in achieving only lift reduction while bringing the wheel closer to the front of wheelhouse results in drag

reduction at the cost of high lift. Axon [15] found the pressure coefficient at the centerline of wheel, for a given wheel width, to be dependent primarily on the geometry of the wheelhouse cavity and independent of the Reynolds number of the flow.

Besides these geometric parameters, the yaw angle of the incoming flow to the wheel also influences the forces. Landström [21] investigated the effect of ground simulation on the aerodynamic force coefficients in a yawed flow of a production car. The experimental investigation was undertaken on an actual car which included cooling air inlets. It was found that without the cooling air inlet, the drag acting on a car in yaw was higher with active ground simulation compared to a stationary ground. This is significant as typically, in real conditions, an automobile is often under yawed conditions. Also, the wheels are placed increasingly closer to the front of the car body in the modern cars to maximize the cabin space for passenger comfort, thereby exposing them to yawed conditions for majority of the time. The higher drag was a consequence of the stronger outboard wake with active ground simulation compared to a stationary ground plane. The drag was found to decrease slightly for the configuration with the cooling air inlet. The lift values were found to generally decrease, although the extent of the reduction depended on cooling and wheel configurations.

2.2.4 PIV Studies

Very few experimental studies have been undertaken with PIV for a shrouded wheel. Part of the reason for this is the challenging experimental setup, especially when the flow inside the wheelhouse needs to be visualized. Emmanuelle et al. [22] investigated the flow around a rotating wheel using PIV. Due to the poor spatial resolution, velocity fields could not be fully resolved. However, they could still confirm the results found in the previous work such as the larger wake area for a stationary floor compared to a moving belt, the increase in wake thickness with increasing wheelhouse radius, the formation of jetting vortices for rotating wheel conditions, establishing the scope for PIV

Gulyas et al. [23] investigated experimentally using PIV the flow around a modified Ahmed body with wheels. The investigation was undertaken for the front wheelhouse with rotating wheels and stationary ground. 2D-2C PIV measurements were taken in different planes both from the side and top of the body. The flow in the underbody or inside the wheelhouse was not visualized. The observed flow features were found to be similar to the features observed previously in the literature.

Chapter 3

Experimental Setup and Methodology

This chapter provides description of the experimental setup adopted and the manner in which Particle Image Velocimetry (PIV) has been used for the investigation on the flow inside the wheelhouse.

3.1 Water tunnel model

For the present study, the water tunnel facility available at the Aero and Hydrodynamics laboratory is used. The water tunnel is a closed loop recirculation tunnel driven by a pump. The test section has a length of 50 m and a cross section of 60 cm x 60 cm. It has an open top i.e. the water has a free surface that is exposed to the atmosphere. With water being the working fluid, Plexiglas or PMMA was the natural choice for the test model fabrication due to its refractive index being close to that of water. This reduces optical distortion. The geometry of the model used for the present study is shown in Figure 3.1. The dimensions of the model are given in Table 3.1.

Table 3.1: Dimensions of the current model

	Dimensions (mm)		**Dimensions (mm)**
L	400	Fr	28
H	140	Sr	14
W	105	c	16
r	45	W_d	40
R	61.5	Wh_d	56

The geometry is an adaptation of the model used by Fabijanic [16, 19] with a few modifications to suit the current experimental needs. The length of the fore-body has been reduced for practical reasons since modern day cars have very short fore-body length. The diameter of the wheel and the wheelhouse are different, as standard size

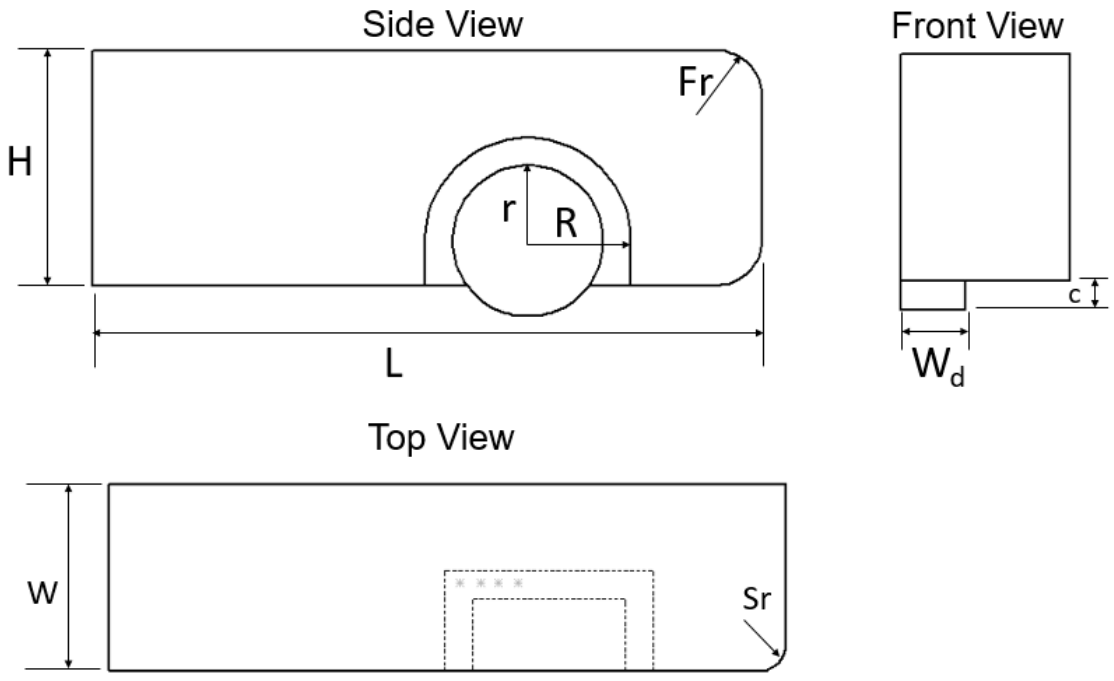

Figure 3.1: Schematic of the model used for the current study. The flow direction is from right to left as seen from the side and top views.

Plexiglas rods and tubes are used to minimize machining operations to retain the optical quality of the material, making visualization using PIV easier.

Figure 3.2 shows a photo of the model used for the current study, along with the other components. The model consists of two parts; the nose section and the main body with the wheelhouse and wheel. The nose section is bolted onto the main body thus allowing it to be easily replaced if studies with longer or shorter fore body length or different radii of curvature needs to be undertaken. The model is suspended by a strut which is clamped on to a horizontal beam above the test section. The wheel is rotated by a belt driven by a motor. The speed of the motor is controlled through LabVIEW 2014 via a computer. The motor is capable of achieving a maximum speed of approximately 250 rpm. The rotational speed of the motor can be monitored by ESCON Studio v2.2 software. It is to be noted here that the rotational speed of the wheel is not monitored and only that of the motor is monitored. A cover for the belt is used to protect it from the incoming water flow.

The geometry used is a half model to reduce the blockage effects which, for the present conditions is 4.5% (Blockage ratio is defined as ratio of cross section of the model to the cross section of the water tunnel). A symmetry plane is used to prevent cross flow from the side of the model to the wheelhouse area. As a result, the model is placed close to the side wall of the tunnel. The symmetry plane is also made of Plexiglas with dimensions of 450 mm x 200 mm x 10 mm and is bolted to the side of the model as well as to the ground plate. A sketch of this is shown in Figure 3.3

Since the ground plane is stationary, the wheel rotation is achieved by immersing the wheel 2 mm into the ground plane. This is done by drilling a rectangular hole in

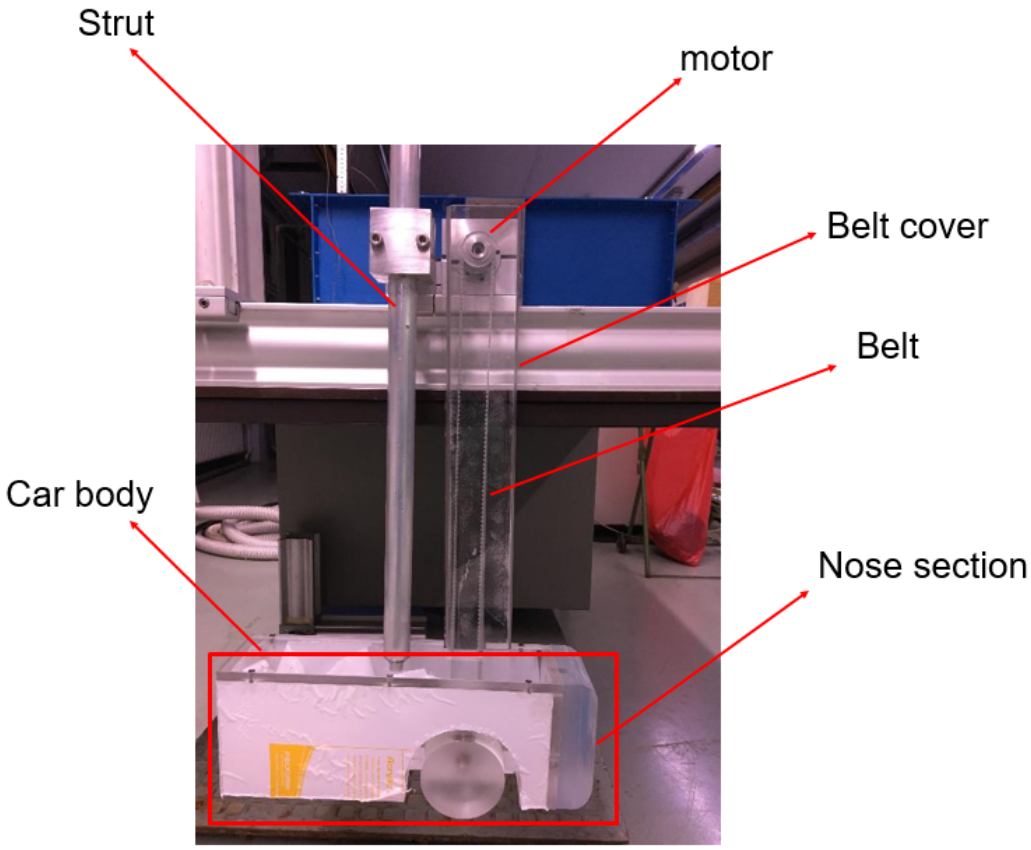

Figure 3.2: Photo of the model used for the present study

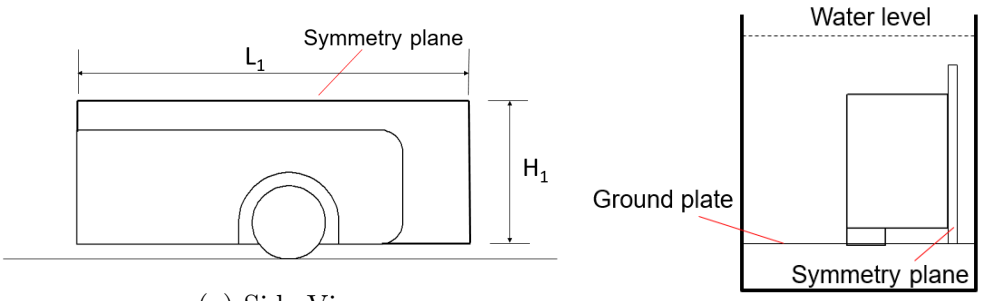

(a) Side View

(b) Front View

Figure 3.3: Side and front views of the model with the symmetry plane. Model is not drawn to scale.

the region around the wheel contact patch. This way, the approach adopted in the LES simulation of wheelhouse by Viswanathan [1] is replicated. The hole is then filled with rockwool, before finally covering the rectangular hole with black duct tape. The duct tape ensured that there were no leakages into this rectangular hole, ensuring the integrity of the contact patch as well as the rockwool underneath it.

The leading edge of the ground plate is positioned at a distance of 500 mm from the inlet of the test section, with the front of the model placed a further 180 mm from the leading edge of the ground plate. The boundary layer thickness along the side wall at

this distance is about 15 mm and hence the symmetry plate is positioned at a distance of 35 mm from the side wall.

3.1.1 Assumptions and Simplifications

The following assumptions and simplifications have been made for the current investigation

(i) The wheel is a solid cylinder with a sharp edge profile and is also non-deformable.

(ii) The edges of the model apart from the nose section are sharp and not rounded.

(iii) The effect of boundary layer growth over the ground plate on the flow is not considered. Although a boundary layer suction system was considered it has not been used. Details of this can be found in the Appendix.

(iv) Any losses from the belt drive system are assumed negligible

(v) The flow is assumed to be isothermal

3.2 PIV Measurement System

Particle Image Velocimetry (PIV) is used for the current investigation of flow inside the wheelhouse. The working principle of PIV is described below.

Seeding particles or tracers are added to the flow, which represent the fluid particles of the flow if these are sufficiently small. These particles are illuminated in the region of interest by a laser light which is emitted in the form of high energy pulse for a very short duration. The tracer particles scatter this laser light, which is then captured by high resolution cameras. The displacement of the particles between the successive frames i.e. successive illuminations is then computed through cross-correlation of the two images. This is done by diving the recorded images into small sub-windows, called interrogation areas. The interrogation area in the first image is compared with the interrogation area at the same location in the second image and through a cross-correlation technique, the average displacement of the particle in that interrogation area is determined. The velocity of the particles are then computed from this displacement and the time separation between the two laser pulses. The PIV technique is illustrated in Figure 3.4.

Planar and Stereoscopic PIV have been used in the present investigation. Both techniques provide planar measurements but the difference between the two is that, in the stereoscopic PIV system, two cameras are employed (instead of one) which record simultaneous off-axis views of the same domain of interest. Because of the two independent off-axis measurements, the out of plane component of velocity could be extracted from the in-plane velocity components. Therefore, the three components of velocity are obtained at a given plane.

The flow is seeded with Sphericell tracer particles which have a nominal diameter of 13 μm and are nearly neutrally buoyant in water. Planar PIV is used to take measurements in planes parallel to the streamwise direction and Stereoscopic PIV

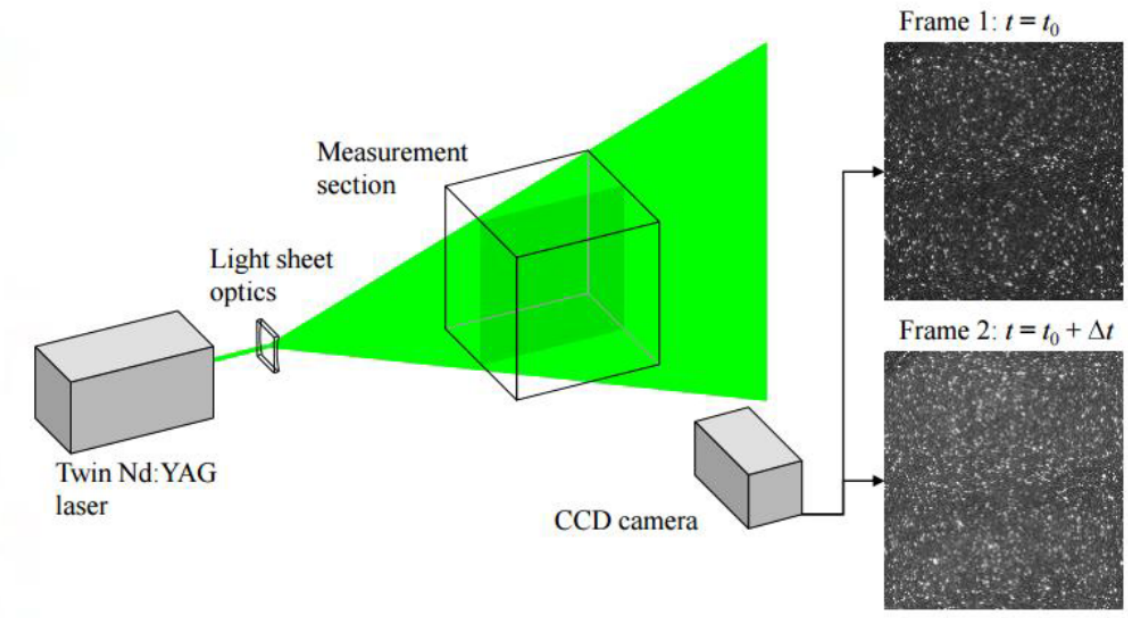

Figure 3.4: Illustration of PIV technique

is used for measurements in planes perpendicular to the streamwise direction. For both cases, the planes were illuminated by a twin cavity double pulsed Nd:YAG laser (Spectra-Physics Quanta Ray). The laser has a maximum repeatable frequency of 10 Hz. The plane is illuminated for a very short duration of 10 ns. The thickness of the light sheet was approximately 1 mm. This was achieved by using a long focal length of 1000 mm cylindrical lens. The time separation between the two laser pulses were 2800 μs and 450 μs for freestream velocity of 0.1 m/s and 0.8 m/s respectively for the planar PIV and 1600 μs and 200 μs for freestream velocity of 0.1 m/s and 0.8 m/s respectively for the stereoscopic PIV. These correspond to a particle displacement of 8 pixels between frames at freestream velocity. The lower Δt in stereo PIV is because, the plane is perpendicular to the streamwise direction meaning that the out of plane component of velocity is high. In order to ensure that the particles remained within the plane of illumination, the Δt was lowered.

The particle images are recorded using Image Pro LX (16M) cameras distributed by the LaVision company with a sensor size of 6.7 μm and pixel format of 4.9k x 3.7k. For planar PIV, the camera was equipped with a Nikon 105 mm focal length lens and images were captured at $f_{\#} = 5.6$. For the stereoscopic PIV, the cameras were equipped with 200 mm focal length lens and images were captured at $f_{\#} = 11$. The f-stop is higher in stereo PIV because, the stereo PIV is quite sensitive to the alignment of the light sheet with the calibration plane (plane of interest) and having a larger f-stop number increases the depth of focus making sure that particles remain in focus over the entire field of view. Scheimpflug adapters are used for the cameras in stereo PIV to ensure that the field of view is in focus. Images were captured and post-processed using the Davis v8 software package. A multi-pass interrogation technique with a final interrogation window size of 32 x 32 pixels, having an overlap of 50%, was used to compute the velocity vectors. This corresponds to a spatial resolution,

based on interrogation area size of 1.04 mm for the planar PIV. The spatial resolution for the stereo PIV varied from 0.86 - 1.12 mm depending on the plane. In total 700 image pairs were recorded at frame rate of 1.44 Hz and 0.78 Hz for the planar and stereoscopic PIV respectively.

3.3 Test Conditions

For the planar PIV, the measurements were performed for two freestream velocities of 0.1 m/s and 0.8 m/s. The Reynolds number, based on wheel diameter are Re = 9000 and Re = 72000 respectively. It is important to match the rotational speed of the wheel with the freestream velocity to simulate the case of vehicle moving through still air. The wheel rpm for the freestream velocities mentioned are approximately 21 and 170. These test conditions are summarized in Table 3.2. The measurements at 0.1 m/s were done to provide data for validation of the LES work undertaken by Viswanathan [1]. The coordinate system is defined such that X-coordinate corresponds to the streamwise direction, the Y-coordinate corresponds to the wall normal direction perpendicular to the flow and positive upwards and the Z-coordinate corresponds to the spanwise direction and positive into the plane. The origin of the coordinate system for the planar PIV is at the center of the wheel. Figure 3.5 depicts the flow direction and the coordinate system adopted for the present study. The flow is from right to left.

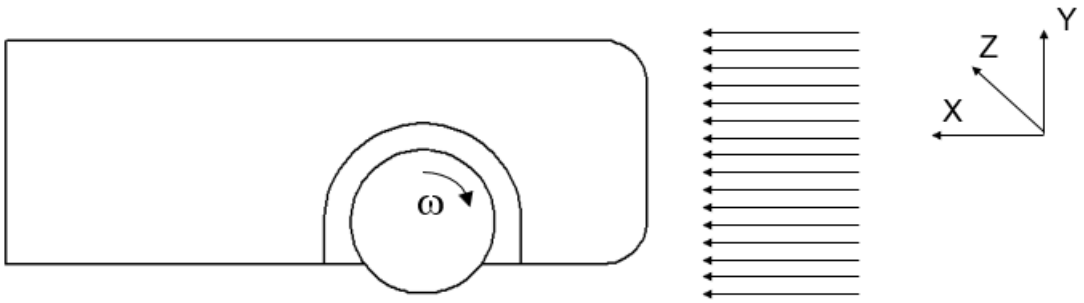

Figure 3.5: Flow direction and the coordinate system adopted in the current study

Table 3.2: Test conditions for Planar PIV

Test Conditions		
U_∞ (m/s)	0.1	0.8
Re	9000	72000
Wheel rotation (rpm)	21	170

There were no significant vibrations from the setup at the freestream velocities investigated. However, the rotation of the wheel was slightly eccentric arising from fabrication. As a result, there was a small pitching moment which was measured using a dial gauge indicator. The amplitude of the oscillations remained the same at 50 μm, but the frequency of oscillations was higher at higher RPM. The different planes,

where the measurements are recorded for both the stereoscopic and planer PIV, are shown in Figure 3.6. The resulting field of view for both the planar and stereoscopic PIV are shown in Figure 3.7. The field of view for the planar PIV is 150 mm in the streamwise direction and 100 mm in the wall normal direction. The field of view for the stereoscopic PIV is 70 mm in the wall normal direction and 120 mm in the spanwise direction except for the '0.6D' plane where the field of view in the spanwise direction is 60mm. A 3rd order polynomial function was used to calibrate the stereoscopic PIV system except for the '-1D' plane. For this '-1D' plane, even though the traversing system ensured that the calibration plate moved by 0.5 mm, the displacement seen by the two cameras was different due to unexplainable reasons. Thus, pinhole model was used for this plane instead of 3rd order polynomial function. Linear mapping was used for planar PIV.

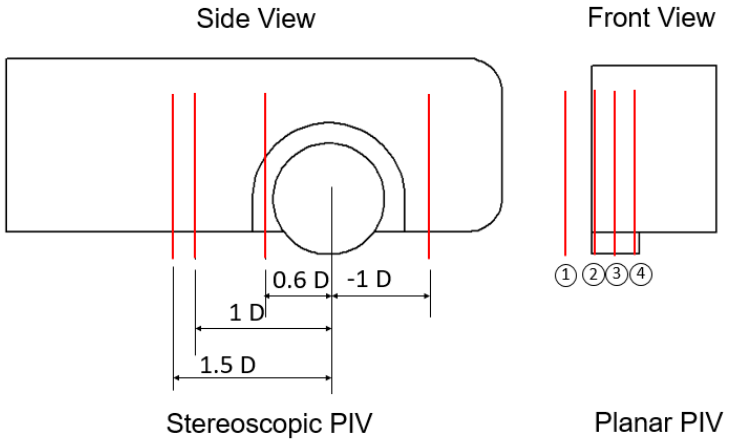

Figure 3.6: Measurement planes for Stereoscopic and Planar PIV. For planar PIV,① corresponds to a plane 1.5cm from the side of the body, ② corresponds to the outer edge of the wheel, ③ corresponds to mid-plane of the wheel and ④ corresponds to the inner edge of the wheel.

Typically the light sheet is spread by the lens from the center of the field of view, as illustrated in Figure 3.4. However, the presence of a strut interfered with the spreading of the light sheet in this traditional manner. Thus, the light sheet had to be spread at an angle to obtain the required illumination of the field of view for the planar PIV configuration. This is illustrated in Figure 3.8.

The measurement plane for planar PIV was illuminated from the top of the water tunnel for the planar PIV measurement. Since the water tunnel has a free surface, waves can occur, especially at high freestream velocities, as shown in Figure 3.9, which can severely distort the light sheet and affect the resulting measurements. In order to prevent these waves from distorting the light sheet, a quadrilateral shaped object made of Plexiglas has been used as shown in Figure 3.11. The sharp edge is aligned with the streamwise direction to have minimal wave generation as well as reduce the forces acting on the object. The bottom face is immersed just below the water surface such that there are no waves in the plane illuminated by the laser light. The light sheet is made to pass through the region indicated as 'cavity' which is filled with water and open only at the top. This provides the light sheet with an undisturbed surface. This

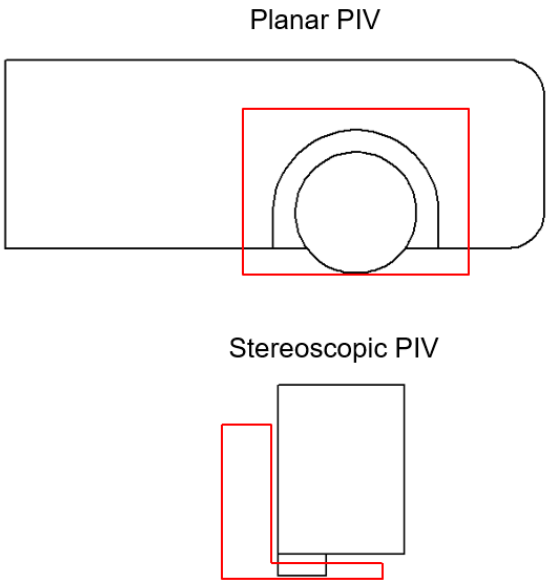

Figure 3.7: Field of view for planar and stereoscopic PIV

object is also used at low speed since, in this case, surface ripples are formed which are still strong enough to cause distortion of the light sheet.

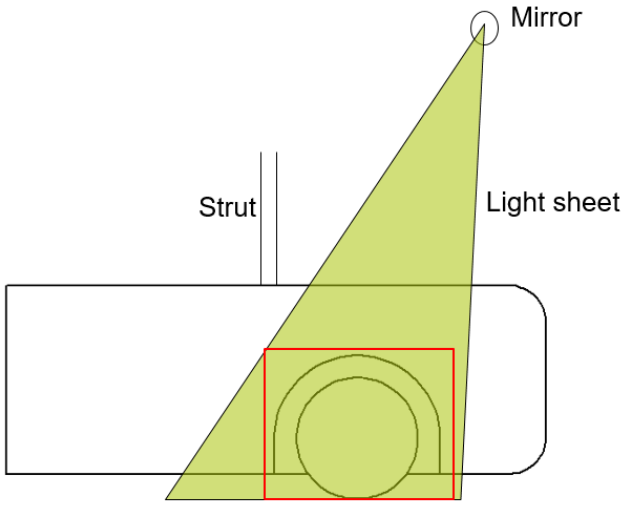

Figure 3.8: Spreading of light sheet for planar PIV configuration

Figure 3.9: Waves from free surface at high speed

The light sheet for the stereoscopic PIV was illuminated through the side wall of the water tunnel as shown in Figure 3.10 and hence was not subject to the interference from

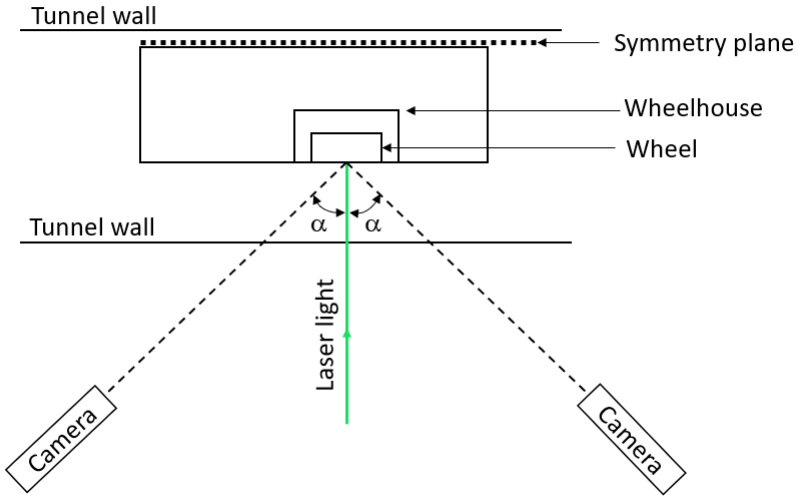

Figure 3.10: Schematic of the setup for stereo PIV as seen in the XZ plane. $\alpha = 35°$

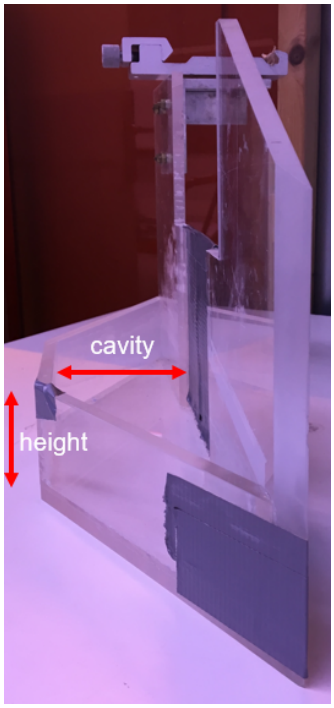

Figure 3.11: Quadrilateral shaped object to prevent light sheet distortion from surface waves

the surface waves or having to go through the model. Since the two cameras viewed the plane of interest at an angle, the wall of the water tunnel is no longer parallel to the camera lens. This creates an optical distortion for the light rays scattered by the seeding particles towards the cameras. Therefore, prisms filled with water was used to reduce this effect.

3.4 Uncertainty Analysis

Uncertainty analysis provides an estimate of the error in a measurement technique. The uncertainty in the mean streamwise velocity measured using PIV is given by Equation 3.1.

$$\epsilon_u = \frac{\sigma_u}{\sqrt{N}} \tag{3.1}$$

where σ is the maximum standard deviation of the velocity in each measurement plane and N is the number of samples. It is assumed here that the samples are uncorrelated and the errors follow a normal distribution. Based on Equation 3.1, the uncertainty in the streamwise velocity at the different planes and Reynolds number are presented in Table 3.3.

Table 3.3: Uncertainty in streamwise velocity at the different planes and Reynolds number

Plane	**Re**	**Uncertainty (m/s)**	**Re**	**Uncertainty (m/s)**
Z/D= 0	9000	2.1×10^{-4}	72000	3.0×10^{-3}
Z/D= 0.02	9000	9.2×10^{-4}	72000	7.2×10^{-3}
Z/D= 0.04	9000	7.7×10^{-4}	72000	6.8×10^{-3}
Z/D= -0.015	9000	11×10^{-4}	72000	8.2×10^{-3}
X/D = -1	9000	7.1×10^{-4}	72000	5.0×10^{-3}
X/D = 0.6	9000	13×10^{-4}	72000	15×10^{-3}
X/D = 1	9000	1.5×10^{-4}	72000	12×10^{-4}
X/D = 1.5	9000	2.0×10^{-4}	72000	1.5×10^{-3}

The uncertainty in the mean wall normal and the mean spanwise velocity are calculated in a manner similar to Equation 3.1 and are found to be of the same order of magnitude as the uncertainty in the mean streamwise velocity. Thus, it can be seen that the uncertainty in the velocity at each measurement plane is quite low. This gives confidence in the results presented in Chapter 4.

Chapter 4

Results and Discussions

This chapter presents and discusses the results from the PIV experiments conducted on the wheelhouse flow for the Reynolds number of 9000 and 72000. The results of $Re = 9000$ and $Re = 72000$ will henceforth be referred to as *Case1* and *Case2* respectively. The results include evaluation from both the planar (2-component) and the stereo PIV and all results presented in this chapter are time-averaged values.

4.1 Planar PIV

This section presents the results from the planar PIV measurements. The measurements were performed on 4 different planes (3 inside and 1 outside the wheelhouse region) parallel to the streamwise direction as shown in Figure 3.6. Before presenting the results from the different planes, an issue that was experienced with illuminating the entire domain of interest is discussed first. Figure 4.1 shows the contour of velocity magnitude at the mid-plane of the wheel. Since the measurement plane was illuminated from the top, the light had to pass through the Plexiglas model, which includes the curved surface of the wheelhouse. This resulted in the shadow regions in the upstream and the downstream part of the wheel indicated by 'S1' and 'S2' in the figure respectively. Thus, information on the flow field is not available in these regions. These shadow regions are observed in all the planes inside the wheelhouse and are therefore masked from computation.

Similarly, strong reflections from the surface of the ground plate caused problems in obtaining reliable velocity data very close to the ground plane. Therefore, this region is removed from all the plots shown for planar PIV.

4.1.1 Flow inside the wheelhouse

Mean Velocity

Figure 4.2 shows the contour of velocity magnitude, non-dimensionalized with the freestream velocity and superimposed with streamlines at the different planes inside the wheelhouse. The locations of these planes are shown in Figure 3.6. Venturi effect

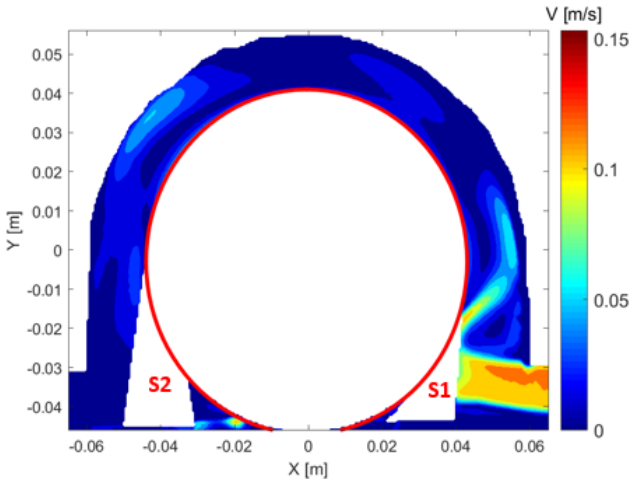

Figure 4.1: S1 and S2 are the shadow regions observed in the domain of interest. The flow is from right to left.

results in the acceleration of the flow in the underbody before entering the wheelhouse. The behavior of the flow beyond this point differs depending on the location of the plane and the Reynolds number of the flow.

Figure 4.2a shows the behavior of the flow at the mid-plane of the wheel for $Re = 9000$. As the flow enters the wheelhouse, flow separation occurs at the upstream edge of the wheelhouse and forms a vortex with a sense of rotation similar to the rotation of the wheel. This vortex is indicated as 'H' in the figure and is the same vortex identified in the literature and discussed in Section 2.2.1. The flow then decelerates upon encountering the rolling face of the wheel and gets deflected towards the inner face of the wheelhouse. The flow enters the wheelhouse in a direction that is opposite to the direction of rotation of the wheel. The resulting shear between the flow and the wheel causes the formation of the 'M1' vortex. Beyond this vortex region, there appears to be no flow towards the top of the wheelhouse suggesting that it either flows into or out of the wheelhouse. Near the uppermost point of the wheel, a bifurcation in the flow is observed wherein, one part of the flow follows the rotation of the wheel towards the 'M1' vortex and the other going in the opposite direction. The latter rolls up to form the 'M2' vortex in a manner similar to the formation of the 'M1' vortex.

Figure 4.2b shows the behavior of flow at the mid-plane for $Re = 72000$. Similar to *Case1*, vortices 'H', 'M1' and 'M2' are observed although the location of 'H' and 'M1' has been shifted downstream. This is an effect of the Reynolds number since the geometry of the wheelhouse is the same. Another difference observed between the two cases was in the flow into the top of the wheelhouse. Unlike in *Case1*, there is flow towards the top of the wheelhouse. This could also be explained as a consequence of higher Reynolds number, where the higher ratio of inertial to viscous forces in *Case2* carries the flow into the top of the wheelhouse. In addition, another vortex 'M3' is observed in the lower downstream region of the wheel. The formation of this vortex could be due to flow separation at the inner edge of the wheel from the flow along the side of the wheelhouse. The reason for the absence of this vortex, in *Case1*, could be because the cross flow resulting from the separation at the lower Reynolds number is not strong enough to reach the mid-plane of the wheel.

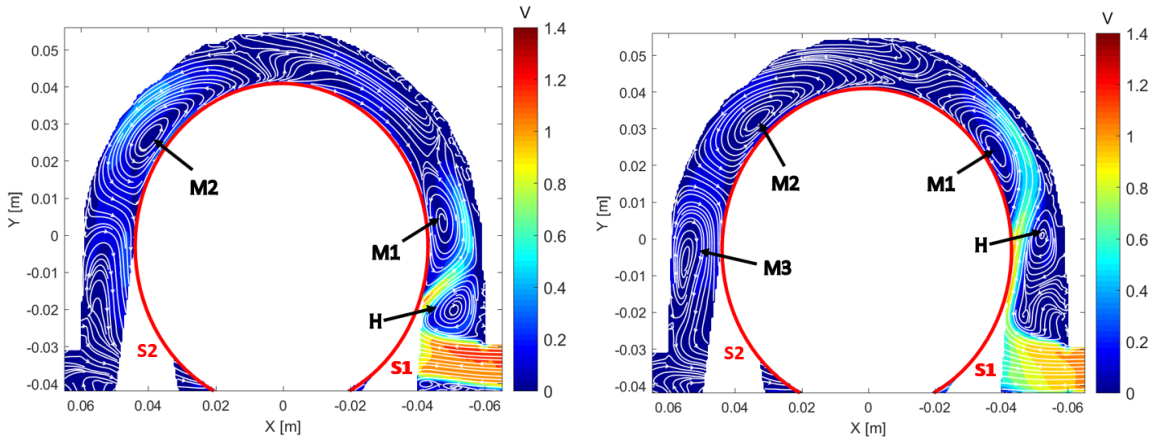

(a) Mid-plane, $Re = 9000$

(b) Mid-plane $Re = 72000$

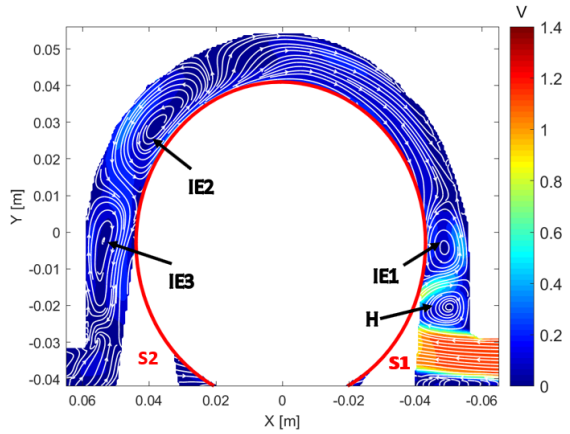

(c) Inner Edge, $Re = 9000$

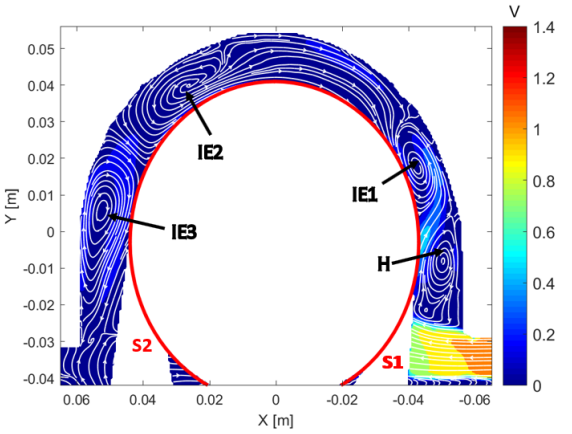

(d) Inner Edge, $Re = 72000$

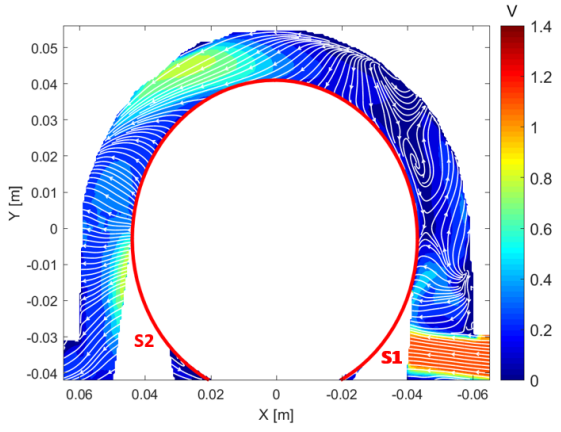

(e) Outer Edge, $Re = 9000$

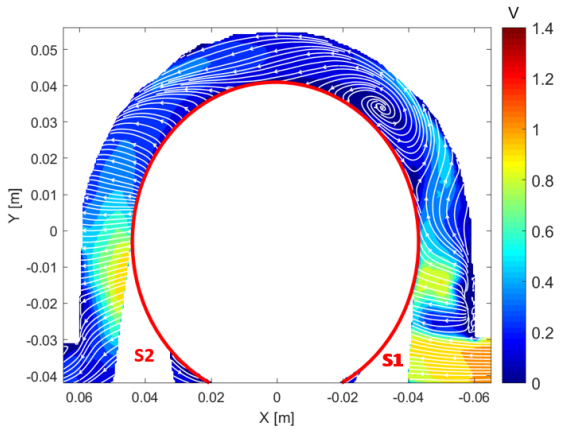

(f) Outer Edge, $Re = 72000$

Figure 4.2: Contours of velocity magnitude non-dimensionalized with the freestream velocity and superimposed with streamlines. The flow is from right to left.

Another observation in *Case2* is that the deflection, i.e. the deviation of the flow after it impinges the wheel, is much steeper after the flow comes into contact with the rolling face of the wheel. This could again be an effect of the Reynolds number. The distribution of the velocity magnitude in *Case2* is similar to *Case1* at the top of the wheelhouse and downstream of the wheel except near the 'M2' vortex, where in *Case1*,

the velocity magnitude is nearly half of the freestream velocity while in *Case2* it is much lower.

Figures 4.2c and 4.2d show the contour of velocity magnitude, non-dimensionalized with the freestream velocity and superimposed with streamlines at the wheel inner edge plane for $Re = 9000$. For *Case1*, shown in Figure 4.2c four vortices are observed. The formation of three of these vortices namely 'H','IE1' and 'IE2' are similar to that explained in the mid-plane of the wheel for 'H','M1' and 'M2' respectively. The vortex 'IE3' which was not present for *Case1* at the wheel mid-plane is observed at the wheel inner edge plane. This supports the previous hypothesis that the formation of this vortex is due to the flow separating at the inner edge of the wheel. Upstream of the wheel, near the 'H' vortex, the velocity magnitude is lower when compared to the wheel mid-plane. The point where the flow bifurcates is moved further downstream from the uppermost point on the wheel in *Case1* when compared to the mid-plane. A higher velocity near the 'IE2' vortex is observed in *Case1* compared to *Case2* similar to the mid-plane.

For *Case2*, shown in Figure 4.2d, characteristics similar to those of the mid-plane are observed wherein the 'H' and 'IE1' vortex is shifted downstream compared to *Case1*. However, unlike in the mid-plane, beyond the 'IE1' vortex, there is no flow towards the top of the wheelhouse, rather the flow moves in the direction of the wheel towards the 'IE1' vortex from the top of the wheelhouse. This could be a result of the influence from the flow along the inner side of the wheelhouse. It can be expected that, along the inner side of the wheelhouse, the flow undergoes acceleration before entering the wheelhouse similar to the other planes inside the wheelhouse. Since there is no wheel in this region, the flow probably follows an oblique path and impinges on the downstream face of the wheelhouse where it gets deflected upwards and flows in the direction of the rotating wheel. This description of the flow in the inner side of the wheelhouse is not new and has already been observed by [4, 1] in their numerical simulation of the wheelhouse flow field.

Figure 4.2e and Figure 4.2f shows the contour of velocity magnitude non-dimensionalized with the freestream velocity and superimposed with the streamlines at the outer plane of the wheel for the two Reynolds number. It can be seen that the different vortices observed in the previous planes are not present in this plane. Also, the velocity distribution inside the wheelhouse is different from that observed in the mid-plane and the inner edge plane. The velocity magnitude is relatively higher in the downstream part of the wheel in both the cases compared to their respective cases at the mid and inner edge plane. In Figure 4.2e, it can be seen that the flow does not enter the wheelhouse and flow upwards. This could be because of the yaw angle of the flow as it approaches the wheel, which carries it towards the outer side of the model and encounter the freestream flow. The vortices that were observed in the different parts of the wheel in the mid and inner edge plane are not observed here. In the upper downstream part of the wheel, a region of higher velocity is observed. Also, from the direction of the streamlines, it appears that there is no flow from the top of the wheel towards the ground, suggesting that there could be either an inflow or an outflow. As will be shown in Section 4.2.1, it turns out that there is a strong outflow from the wheelhouse.

For *Case2* (Figure 4.2f) the velocities are much higher in the upstream part of the

wheel compared to *Case1*. A vortex is formed in the upper upstream part of the wheel in a manner similar to the mid plane and inner edge plane. Once the flow reaches the top of the wheelhouse, there appears to be no flow towards the ground again suggesting a strong outflow similar to *Case1*. A region of high velocity can also be seen in the lower downstream region of the wheel for *Case2* whereas for *Case1*, a region of high velocity is seen in the upper downstream part of the wheel in addition to the lower downstream part of the wheel.

A similarity between all the planes inside the wheelhouse in *Case1* is that, there is region of relatively high velocity near the upper downstream part of the wheelhouse. The cause for this behavior is not clear from the current PIV results.

Turbulence Intensity

Figure 4.3 shows the turbulence intensity, defined here as the ratio of the root mean square of the velocity fluctuations to the freestream velocity, for the two Reynolds numbers.

$$TI_x = \frac{u_{rms}}{u_\infty} \tag{4.1}$$

$$TI_y = \frac{v_{rms}}{u_\infty} \tag{4.2}$$

$$TI_z = \frac{w_{rms}}{u_\infty} \tag{4.3}$$

Figure 4.3a and Figure 4.3b show the turbulence intensity at the mid-plane for the two cases respectively. It can be seen from the figure that, in both the cases, the turbulence intensity shows a local maxima near the entry to the wheelhouse (X-0.06 m). The reason for the sudden rise can be explained by looking at the location highlighted by the white rectangle in Figure 4.4, which shows a raw image at the wheel mid-plane. It can be seen that, in the highlighted region, seeding particles are not visible. This is because the light sheet is unable to penetrate this small region which result in a large uncertainty locally explaining the peaks in the turbulence intensity contour near the entry to the wheelhouse.

It can be seen from Figure 4.3 that the rms of the streamwise velocity fluctuations upstream of the wheel is higher in both the cases. This is associated with the shear layer formed as a result of the jet-like flow entering the wheelhouse and flowing towards the top in a direction opposite to that of the rotation of the wheel. The unsteadiness of the jet results in a large velocity fluctuations. Also, near the 'H' vortex, the turbulence intensity is higher for *Case1*, compared to *Case2*.

Figure 4.3c shows the turbulence intensity at the wheel inner edge for *Case1*. There is a region of high shear stress near the 'H' vortex similar to the mid-plane indicated by the high turbulence intensity. The turbulence intensity in the upstream region of the wheel is lower in *Case2* (Figure 4.3c) compared to *Case1*. Also, comparing the turbulence intensity at the inner edge plane and the mid-plane, it can be see that the turbulence intensity is considerably lower in the inner edge plane for *Case2*. The

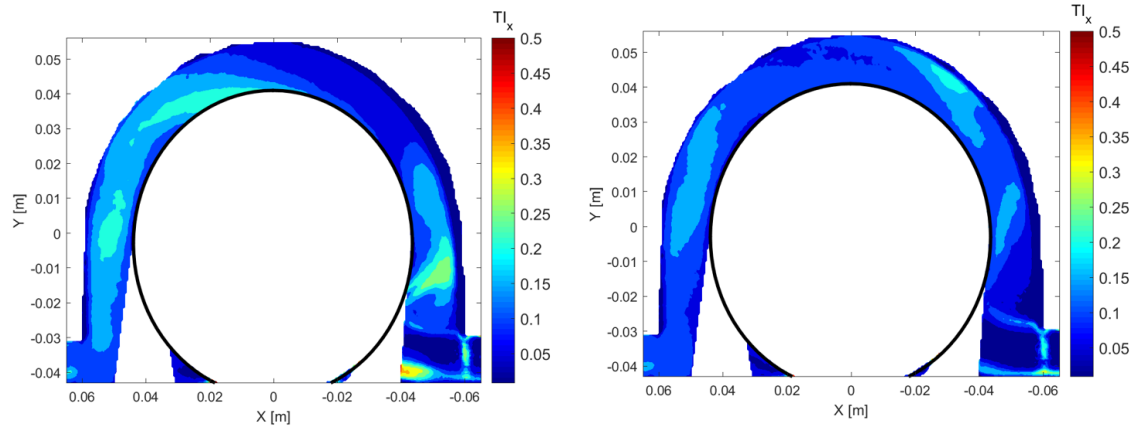

(a) Mid-plane, $Re = 9000$

(b) Mid-plane, $Re = 72000$

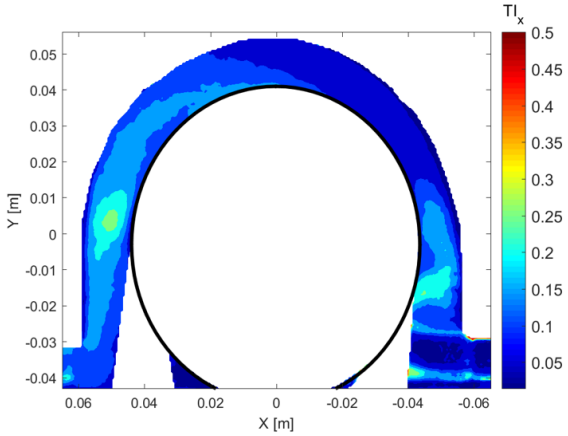

(c) Inner Edge, $Re = 9000$

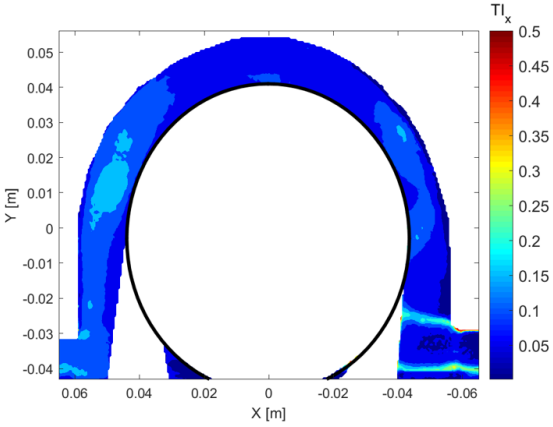

(d) Inner Edge, $Re = 72000$

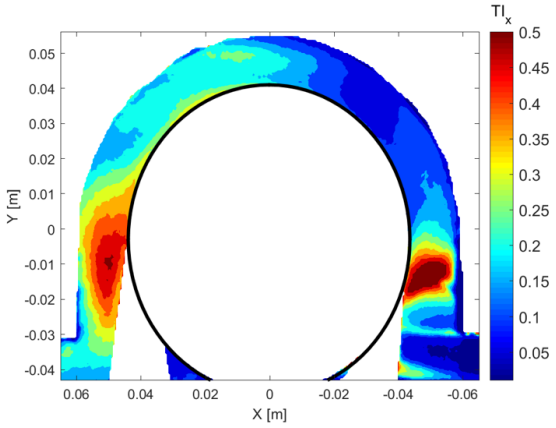

(e) Outer Edge, $Re = 9000$

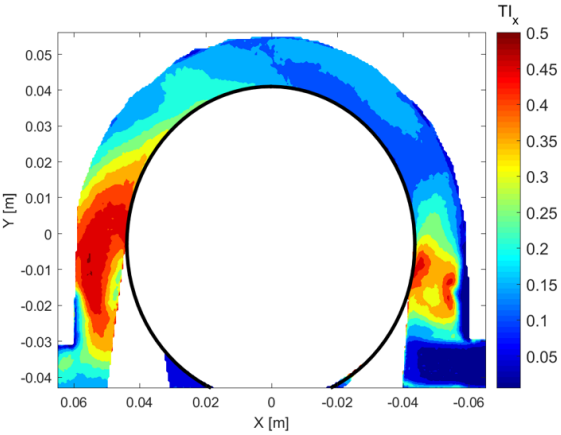

(f) Outer Edge, $Re = 72000$

Figure 4.3: Contours of Turbulence Intensity (TI) in the x direction based on freestream velocity. The flow is from right to left.

difference in the length and strength of the shear layer between the two planes for *Case2* could explain the observed difference.

Figure 4.3e and Figure 4.3f shows the turbulence intensity at the wheel outer edge. It can be seen that a high turbulence intensity is present near the leading and trailing edge of the wheelhouse, in both the cases arising probably from the unsteady outflow.

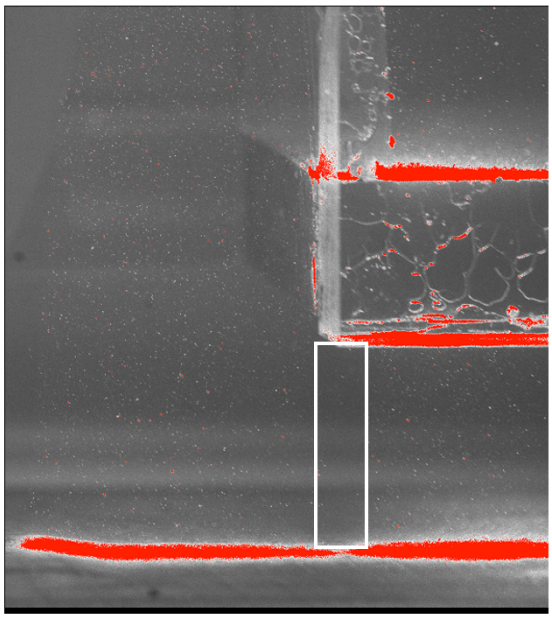

Figure 4.4: Raw image of the wheel-mid plane. The bright red regions are high intensity counts due to the reflections from the ground. The flow is from right to left

Figure 4.5 shows the rms of the wall normal velocity fluctuations for the two Reynolds numbers. The turbulence intensity is again normalized by the respective freestream velocities. Figure 4.5a and Figure 4.5b show the turbulence intensity for *Case1* and *Case2* respectively at the mid-plane. It can be seen from the figure that the turbulence intensity, in both the cases, is high in the upstream region of the wheel. This can again be due to the strong shear layer observed in the velocity magnitude contour plot (Figure 4.2a and Figure 4.2b). In the downstream region, *Case1* has higher turbulence intensity in the wall normal direction compared to *Case2*. The higher mean velocity near the M2 vortex could explain this observation. The higher mean velocity gradients causes stress which could explain the higher turbulence intensity in the wall normal direction.

Figure 4.5d shows the turbulence intensity in the wall normal direction for *Case2*. It can be seen that the turbulence intensity in wall normal direction is concentrated in one region upstream of the wheel, which is related to the shear layer present here. However, compared to*Case2* in the mid-plane, the size of this region is reduced which is a result of the shorter and weaker shear layer observed in the inner edge plane. The turbulence intensity in the wall normal direction is higher in the downstream region of the wheel for *Case1* compared to *Case2* and this is similar to the mid-plane. At the outer plane (Figure 4.5e and Figure 4.5f), the turbulence intensity upstream of the wheel is high as is the case in all the planes inside the wheelhouse .

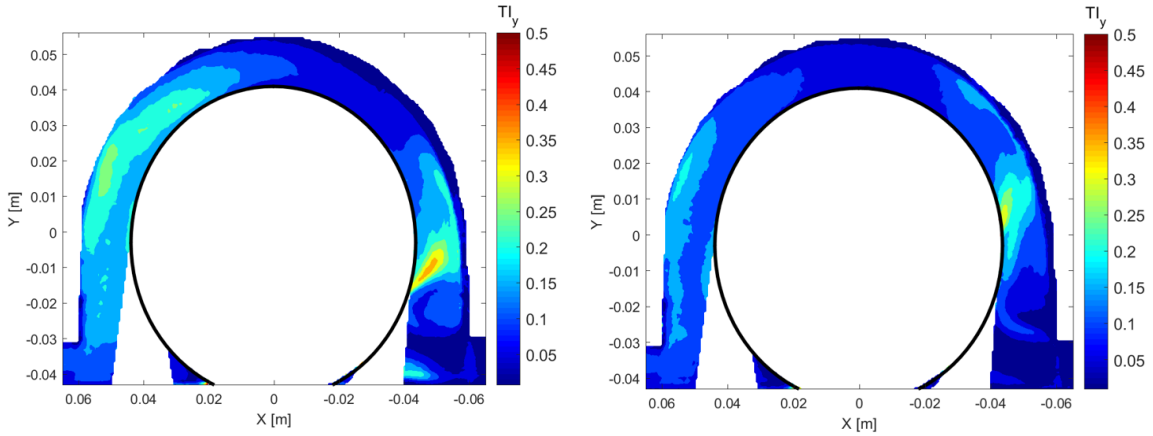

(a) $Re = 9000$ (b) $Re = 72000$

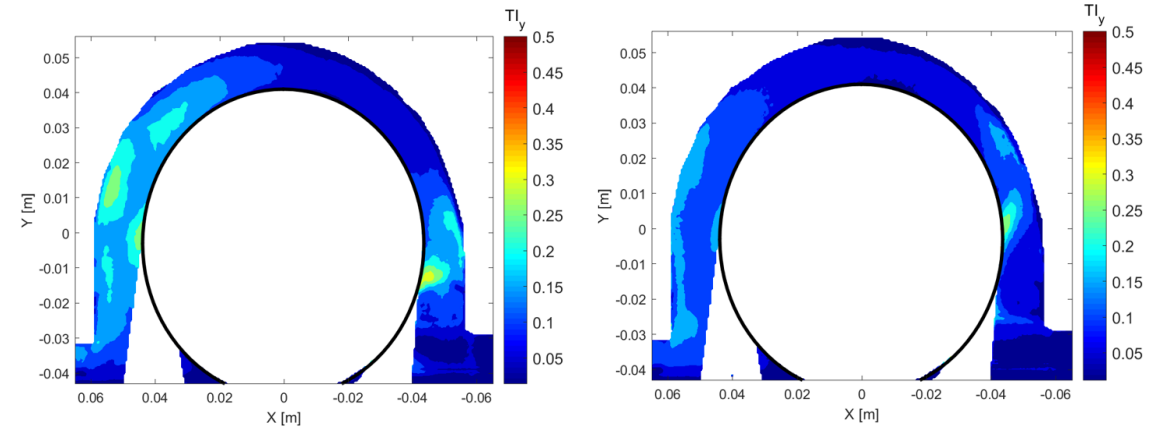

(c) $Re = 9000$ (d) $Re = 72000$

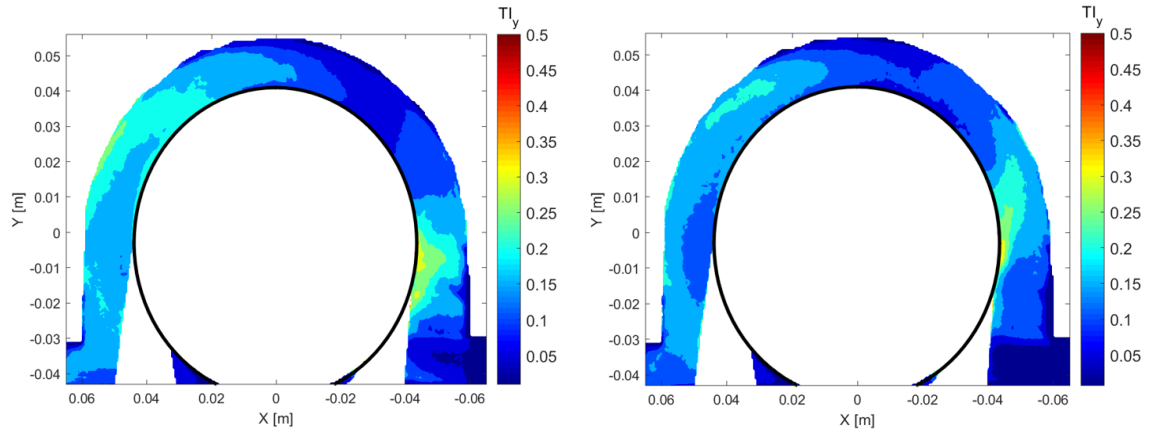

(e) $Re = 9000$ (f) $Re = 72000$

Figure 4.5: Contours of Turbulence Intensity (TI) in the y direction based on the freestream velocity. The flow is from right to left.

4.1.2 Flow outside the wheelhouse

Mean velocity

Figure 4.6 shows the contour of velocity magnitude non-dimensionalized with the freestream velocity and superimposed with streamlines at the outer plane as shown in

Figure 3.6, which is at a distance of 1.5 cm from the side of the model. In Figure 4.6a, i.e. *Case1*, two separation regions are present; one in the upper right of the figure ('SR1') and the other in the lower left ('SR2'). The separation region at 'SR1' is located over the side of the model, while the separation region in 'SR2' is the imprint of the jetting vortex from the wheel contact patch which induces flow away from the ground plate. The flow separation from the side of the model is quite large in size. In between these separation regions, a region of high velocity is observed; also the path of the mean flow is oblique. In *Case2* (Figure 4.6b), the size of the above mentioned separation regions are reduced consistent with the higher Reynolds number of the flow.

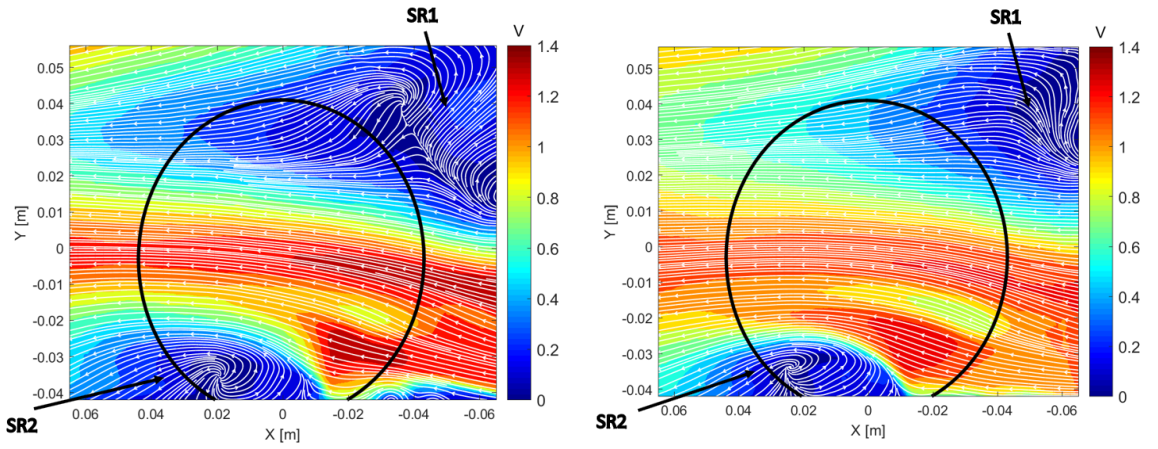

(a) $Re = 9000$

(b) $Re = 72000$

Figure 4.6: Contours of velocity magnitude at the outer plane non-dimensionalized with freestream velocity and superimposed with streamlines. The flow is from right to left.

Another difference that could be observed between the two cases is in the streamline pattern ahead of the contact patch (X-0.04 m, Y-0.04 m). The streamline is wavy in *Case1*, whereas in *Case2*, this waviness is not present. Axerio et. al [9] observed the presence of an additional horseshoe vortex for a stationary wheel in front of the contact patch and explained it as a result of the flow impinging the surface of the wheel. The reasoning was based on the analogy of a flow impinging a vertical cylinder in contact with the ground. Baker [24] showed in his experimental study on a vertical cylinder that, with an increase in the Reynolds number the horseshoe vortex moved closer to the cylinder. In the present study, *Case1* is at lower Reynolds number compared to *Case2*. Therefore, it can be expected that the horseshoe vortex would be closer to the wheel for *Case2* and cannot be resolved by the present PIV measurement. Hence, the waviness in the streamlines observed at this plane for *Case1* is not present in *Case2*

Turbulence Intensity

Figure 4.7 shows the contour of turbulence intensity in the streamwise direction for the two Reynolds numbers. A high turbulence intensity is observed in a region that is upstream of the wheel in Figure 4.7a and also near the separation region near the ground. The sharp curve near the upper separation region showing a sudden drop in

the turbulence intensity is unphysical and caused by the reflection from the wheelhouse edge. In *Case2* (Figure 4.7b) the turbulence intensity is similar to *Case1* in the lower right half of the figure. However, in the upper half, the turbulence in the streamwise direction is higher in *Case2* when compared to *Case1*. The shear layer observed near the lower separation region in the ground, extends further downstream in *Case2* when compared to *Case1* and is also thinner.

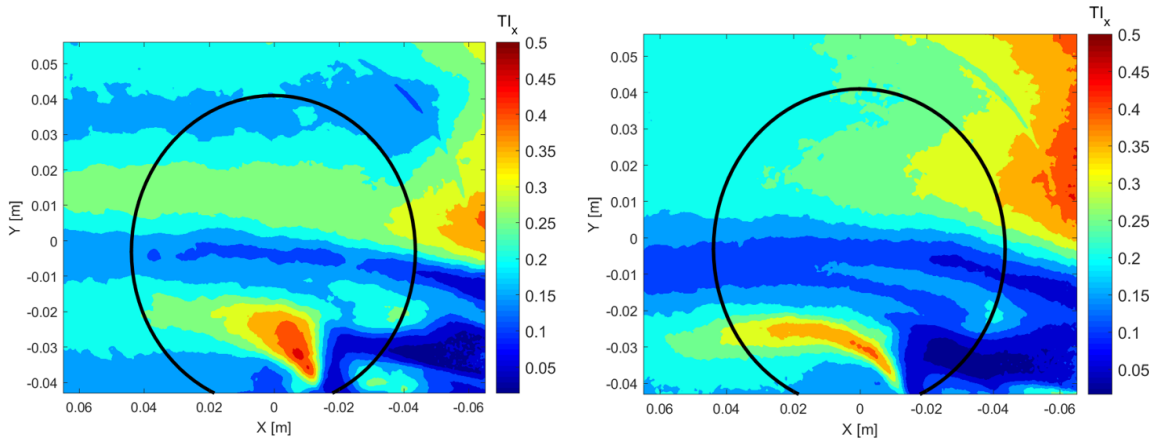

(a) $Re = 9000$ (b) $Re = 72000$

Figure 4.7: Contours of Turbulence Intensity (TI) in the x direction based on freestream velocity. The flow is from right to left. The black circle indicates the region where the wheel is present.

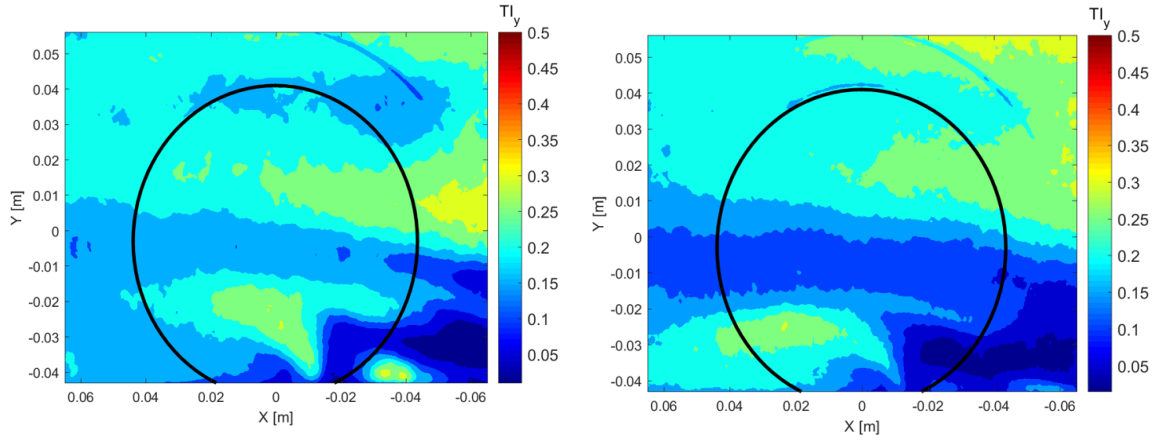

(a) $Re = 9000$ (b) $Re = 72000$

Figure 4.8: Contours of Turbulence Intensity (TI) in the y direction based on the freestream velocity. The flow is from right to left.

Figure 4.8 shows the contour of turbulence intensity in the wall normal direction for the two Reynolds numbers. A higher turbulence intensity is observed near the separation regions similar to the turbulence intensity in the streamwise direction. Similar to the turbulence intensity in the streamwise direction, the sharp curve near the upper separation region showing a sudden drop in the turbulence intensity is unphysical and caused by the reflection from the wheelhouse edge However, another region of high turbulence intensity is observed upstream of the contact patch in *Case1* which is not

present in *Case2*. This could be because of the impingement effect explained earlier in Section 4.1.2.

4.2 Stereo PIV

This section presents the results from the stereo PIV measurements. Stereo PIV has been used to study the flow behavior in the wake of the wheel for the two Reynolds numbers. Planar PIV cannot be used for this purpose since the camera cannot be placed behind the car body without disrupting the flow. Another advantage of using stereo PIV is that, all three components of velocity can also be obtained at the measurement plane. The measurements were performed on 4 different planes (1 upstream and 3 downstream of the wheel) perpendicular to the streamwise direction as shown earlier in Figure 3.6. Similar to the planar PIV measurements, strong reflections were present in certain regions in the measurement plane and these were removed from computation.

4.2.1 Mean flow

Upstream of the wheel

***X/D* = -1**

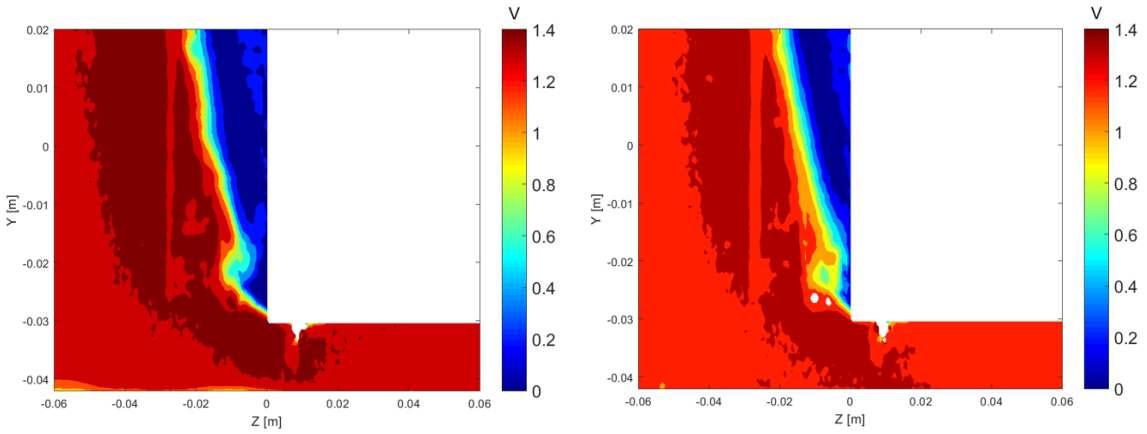

(a) $Re = 9000$ (b) $Re = 72000$

Figure 4.9: Contours of velocity magnitude non-dimensionalized with the freestream velocity at X/D = -1. The flow is into the plane.

Figure 4.9 shows the contour of velocity magnitude non-dimensionalized with the freestream velocity for the two Reynolds numbers. It can be seen that the flow undergoes acceleration in the underbody in both the cases. Measurements were taken at this plane specifically to determine the angle of the incoming flow as it approaches the wheel in the underbody region, based on which the vortex generator can be suitably aligned with respect to the flow. Figure 4.11 shows the angle of the incoming

flow along a horizontal line in the spanwise direction indicated in the schematic (Figure 4.10). It can be seen that the yaw angle is almost the same for both Reynolds numbers. Thus, it can be said that the yaw angle is independent of Reynolds number. The region where the angle goes below zero is unphysical and is caused by a strong reflection from the model leading to inaccurate velocity vectors. The region between $Z0$ and $Z0.04$ m corresponds to the width of the wheel. The angle at the edge of the model ($Z0$) is around 20°(neglecting the unphysical region increases till 1 cm in the positive spanwise direction) before steadily decreasing. In addition to the information on the incoming flow angle, a separation region along the side of the model can also be seen near the corner in Figure 4.9. This region is formed due to boundary layer separation along the side of the body which is visualized as a region of low velocity in Figure 4.9. The size of this separation region is slightly smaller in *Case2* compared with *Case1*.

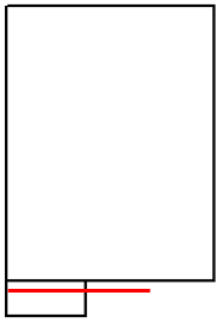

Figure 4.10: Schematic showing the line where the angle of the incoming flow is determined. The flow is into the plane.

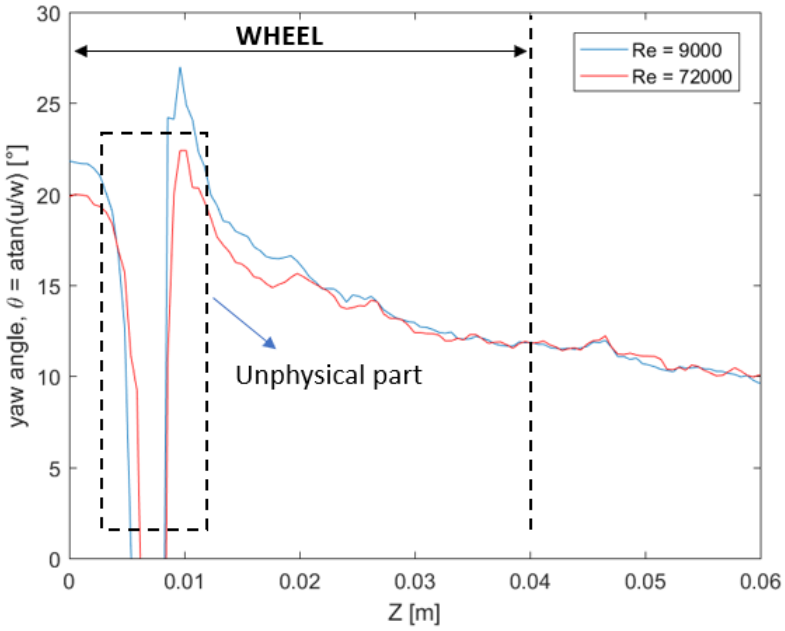

Figure 4.11: Angle of the incoming flow along the line shown in Figure 4.10. The region between $Z0$ and $Z0.04$ m correspond to the width of the wheel.

Wake flow

$X/D = 0.6$

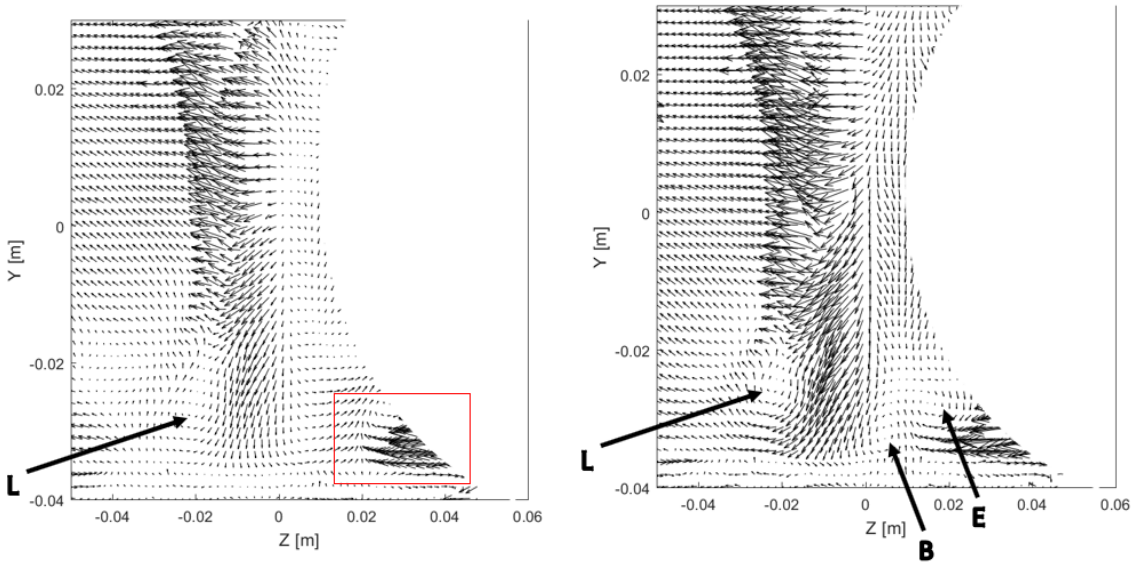

(a) $Re = 9000$

(b) $Re = 72000$

Figure 4.12: In-plane velocity vectors at $X/D = 0.6$, downstream of the wheel; which is partially inside the wheelhouse. The flow is into the plane. $Z0$ corresponds to the outer edge of the wheel. The blank white space correspond to part of the wheel.

Figure 4.12 shows the in-plane velocity vectors at the plane $X/D = 0.6$ for the two Reynolds number. The blank white space in the figure corresponds to part obscured by the wheel. This arises due to viewing the plane from the two cameras at an off-axis angle which after mapping results in a final image as shown in Figure 4.12. Figure 4.12a shows the in-plane velocity vectors for *Case1*. A vortex L can be seen near the ground. This is the vortex that is shed from the contact patch. Closer to the wheel outer edge ($Z0$), a strong outflow and downwash is observed. This supports the observation of strong outflow made earlier with planar PIV at the wheel outer edge plane, shown in Figure 4.2e.

Figure 4.12b shows the in-plane velocity vectors for *Case2*. Similar to *Case1* the ground vortex L is observed. In addition, two other vortices are observed near the ground indicated by B and E in the figure. The formation of the vortex E and B could be explained from the work of [1]. In this LES simulation of the wheelhouse flow field, the vortex E was found to be an extension of the H vortex formed at the upstream edge of the wheelhouse. A low pressure region along the inner edge of the wheel deflected the H vortex towards the inner edge. The sense of rotation of the vortex E was found to be similar to the ground vortex L.

The formation of the B vortex was explained in [1] in the following manner: the flow along the inner side of the wheelhouse impinges the downstream arch of the wheelhouse. The flow was then found to recirculate and move across the wheel in the downstream section where it separates to form a vortex. The vortex is then carried along the

underbody region closer to the outer edge of the wheel. The sense of rotation of the vortex B was found to be opposite to that of the ground vortex L.

Observing Figure 4.12b, it can be seen that the sense of rotation and the location of the vortices observed in the plane, matches with the simulation results. Considering that the simulation results of [1] were validated with the PIV results from this work (see also Section 4.4), it can be expected that the formation of these vortices are also similar. Also, the formation of the B and the E vortex in [1] is different from that of the previous LES simulation of wheelhouse flow by [19]. Therefore this experimental result validates the findings of [1].

The B vortex is not observed at this plane for *Case1*. This could be because the formation of the vortex B happens further downstream of the wheel in *Case1* and is simply not captured in this plane. Although vortex E is also not seen for *Case1* in the same manner observed in *Case2*, looking closely at the in-plane velocity vectors in the region highlighted by the red rectangle in Figure 4.12, the curling of the in-plane velocity vectors is observed. Thus, it is reasonable to expect that, with a wider field of view in the spanwise direction, vortex E could also be observed.

Comparison of mean velocity profile

In this section, the wake velocity profiles at different distances downstream of the wheel between the two Reynolds numbers are compared. This is done to determine whether any quantitative similarity exists between the two cases. Figure 4.13 shows the lines at which the different components of velocity are compared between the two cases.

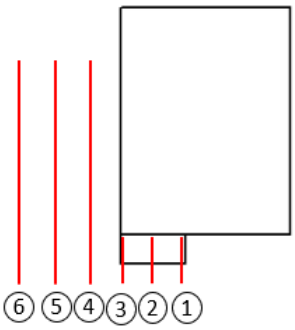

Figure 4.13: Schematic depicting the lines along which the velocity profiles are compared. Line ① is at a location corresponding to inner edge of the wheel, line ② at the centerline of the wheel, line ③ at the wheel outer edge. Line ④ is at a distance of 1 cm from the side of the body, line ⑤ is at 2 cm from the side of the body and line ⑥ is at 3 cm from the side of the body.

Figure 4.14 shows the streamwise velocity at the different lines shown in Figure 4.13 for the two cases. It can be seen that along the outer edge, the streamwise velocity is very small in both the cases. Towards the outer lines, the streamwise velocity increases. The value of the streamwise velocity at the lines 5-6 reaches the value of the freestream velocity at a height of y/d = 0 which corresponds to the mid of the

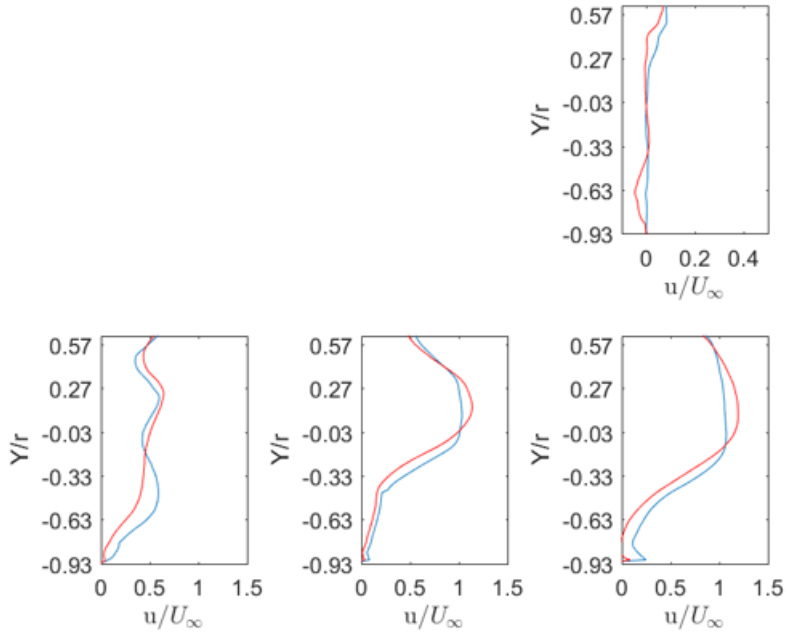

Figure 4.14: scaled u velocity along the different lines indicated earlier. The red line corresponds to $Re = 9000$ and blue line corresponds to $Re = 72000$. The upper right plot corresponds to line ③, the lower left plot corresponds to line ④, the lower middle plot corresponds to line ⑤ and the lower right plot corresponds to line ⑥. Information along line ① and ② are not plotted since at this plane data into the wheelhouse is not available.

wheel before decreasing again. This suggests that the flow along these lines beyond the height of y/d = 0 is affected by the flow from the wheelhouse.

Figure 4.15 shows the wall normal velocity at the different lines for the two cases. It can be seen that along the outer edge a negative wall normal velocity is observed indicating downward flow. This was observed earlier in Figure 4.12. However, the downwash is stronger in *Case2* compared to *Case1*. This can also be observed by comparing Figure 4.12a and Figure 4.12b. Saddington et. al [11] showed that the counter rotating vortices in the wake of the wheel (i.e. the jetting vortices) pull the flow towards the ground. The strength of the L vortex is higher in *Case2* when compared to *Case1* as shown in Figure 4.16. This could explain the stronger downwash observed in *Case2* compared to *Case1*. Along line 4, the velocites are similar in both the cases although there is a change in sign in the wall normal velocity at a height of around $Y0$ m where an upwash is observed. This could be explained by looking at Figure 4.6b. Above the separation region observed near the ground which is indeed the ground vortex L, a region of high velocity is observed which has an oblique path. The height at which it is observed is comparable to the height where the reversal in direction of wall normal velocity occurs. In lines 5 and 6 the wall normal velocity is higher in *Case1* compared to *Case2*.

Figure 4.17 shows the spanwise velocity along the different lines for the two cases. The profile of the spanwise velocity along the height is similar in both the cases. An

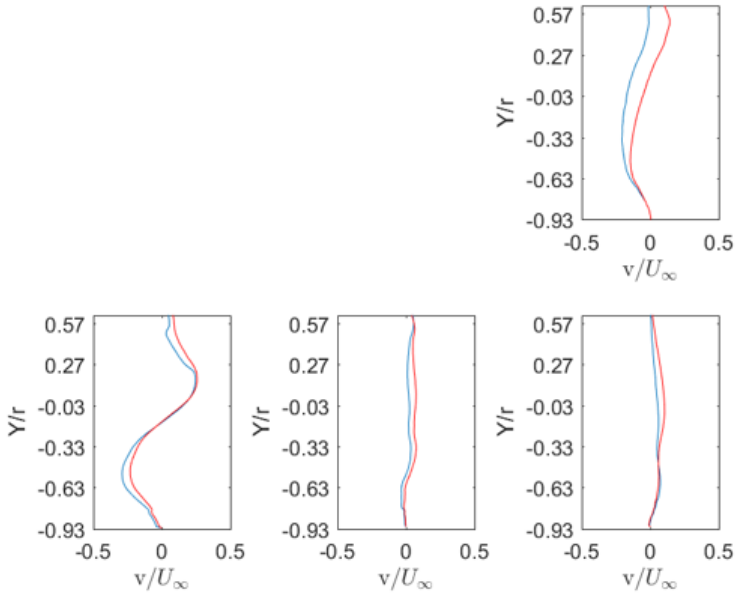

Figure 4.15: scaled v velocity along the different lines indicated earlier. The red line corresponds to $Re = 9000$ and blue line corresponds to $Re = 72000$. Refer Figure 4.14 for numbering.

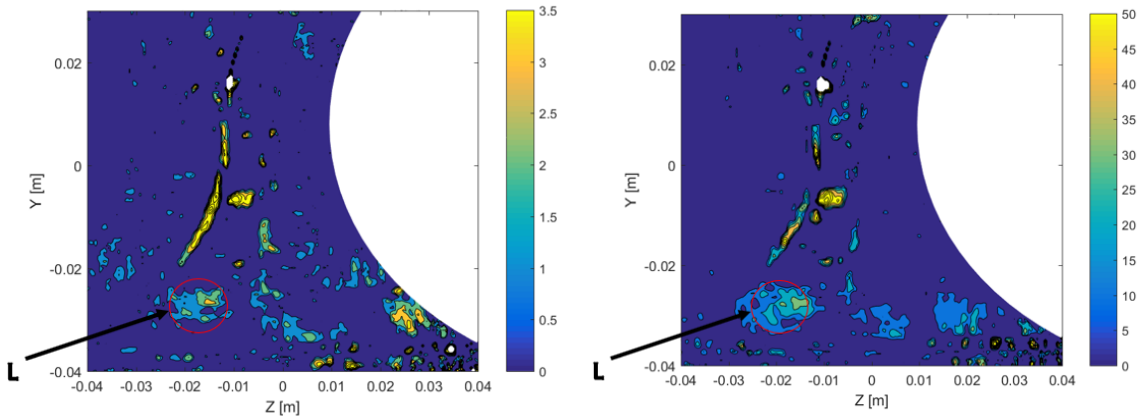

(a) $Re = 9000$ (b) $Re = 72000$

Figure 4.16: Contours of swirling strength at $X/D = 0.6$ for the two Reynolds numbers

interesting observation is that in lines 4-6, the spanwise velocity is highly negative in both the cases, indicating a very strong outflow from the wheelhouse. The magnitude of the spanwise velocity decreases with increase in distance from the side of the body. The above figures show that the flow is highly three dimensional in the wheelhouse.

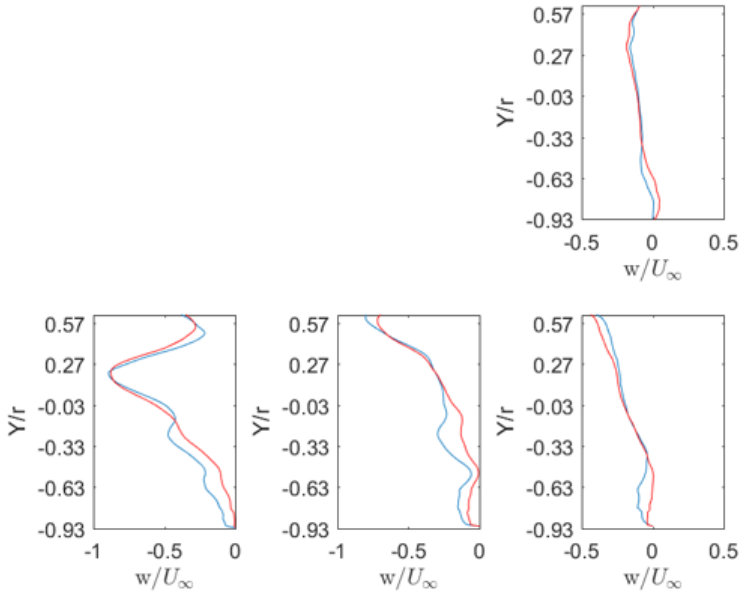

Figure 4.17: scaled w velocity along the different lines indicated earlier. The red line corresponds to $Re = 9000$ and blue line corresponds to $Re = 72000$. Refer Figure 4.14 for numbering.

$X/D = 1$

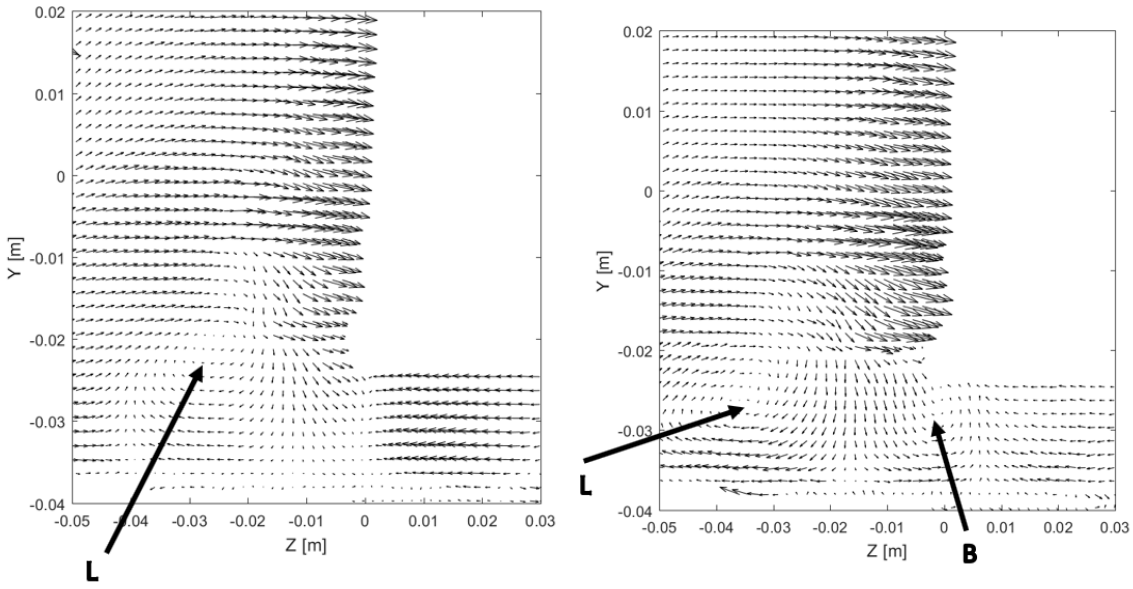

(a) $Re = 9000$

(b) $Re = 72000$

Figure 4.18: In-plane velocity vectors at $X/D = 1$ downstream of the wheel. The flow is into the plane.

Figure 4.18 shows the in-plane velocity vectors at $X/D = 1$ for the two Reynolds numbers. The ground vortex, L, is present in both the cases but the position of the vortex is closer to the body in *Case1* compared to *Case2*. It can be seen from

Figure 4.18 that Vortex E is not present in this plane, in both the cases, suggesting that it dissipated quickly in the underbody. Also, the B vortex is present only in *Case2* suggesting that the higher viscous effects in *Case1* probably caused the B vortex to dissipate quickly.

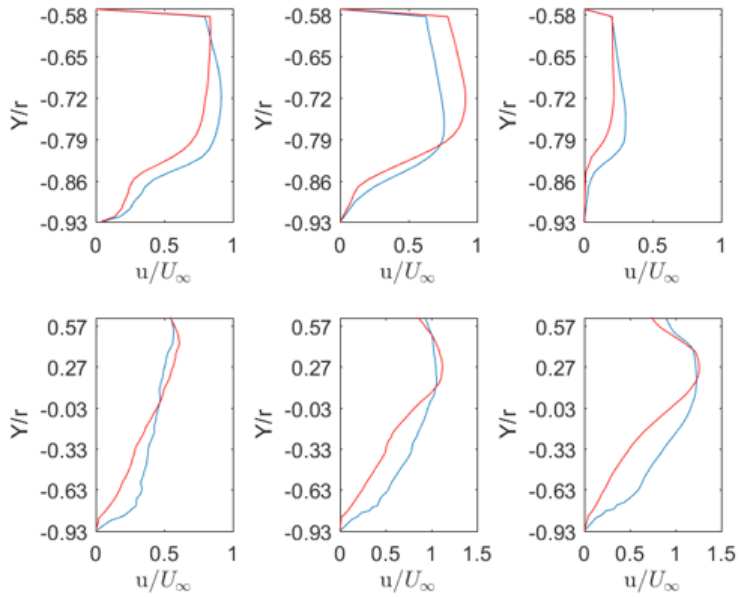

Figure 4.19: Scaled u velocity along the different lines indicated earlier. The red line corresponds to $Re = 9000$ and blue line corresponds to $Re = 72000$. Refer Figure 4.14 for numbering.

Figures 4.19-4.21 show a comparison of the 3 components of the velocity for the two cases along the different lines. Comparison of the streamwise velocity in Figure 4.19 shows that the maximum streamwise velocity is higher in *Case2* compared to *Case1* along the lines 1 and 3. However, along the line 2, the streamwise velocity is higher in *Case1* compared to *Case2*. Along the outer lines (line 4-6) the streamwise velocity profiles are similar although the magnitude is higher in *Case2* compared to *Case1* especially closer to the ground. A maximum in streamwise velocity is reached around a height of $Y0$ m.

The wall normal velocity, shown in Figure 4.20, is low along all the lines suggesting that the flow is primarily two-dimensional. Figure 4.21 shows the spanwise velocity. Along the line 2, a negative spanwise velocity is observed indicating an outflow. Along the line 3, a negative spanwise velocity is still observed for *Case1* but a positive spanwise velocity is observed for *Case2* especially closer to the ground. This could be because of the presence of the B vortex. Since the rotation of the B vortex is anti-clockwise, along the outer edge there is a positive spanwise velocity. Along the lines 4-6, the flow is angled towards the body indicated by the predominantly positive spanwise and streamwise velocity. The sharp gradients observed in Figures 4.19 - 4.21, especially near the underbody of the car are caused due to reflections from the body surface leading to inaccurate velocity vectors. The sharp gradient arises since the velocity is forced to zero at the wall if the velocity at the wall is not already zero due to the reflections from the surface. This is done for the other measurement planes as well.

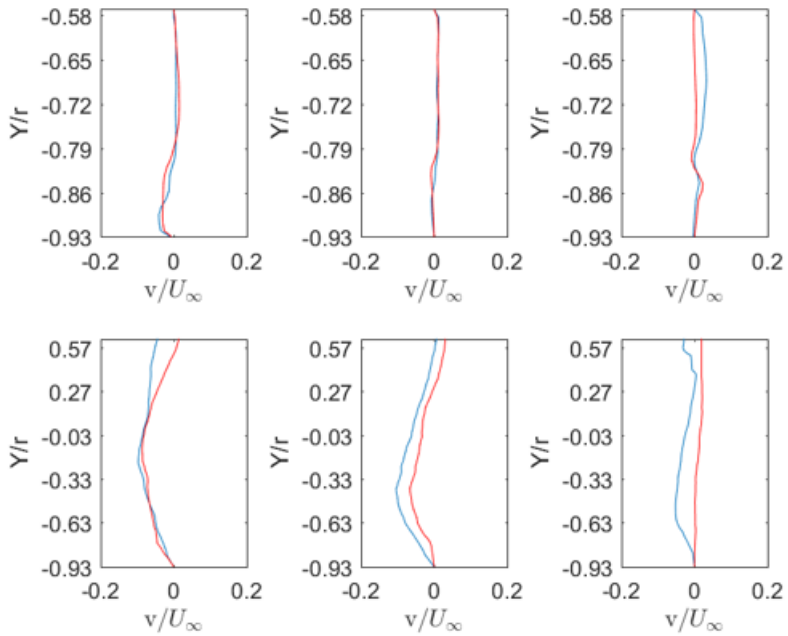

Figure 4.20: Scaled v velocity along the different lines indicated earlier. The red line corresponds to $Re = 9000$ and blue line corresponds to $Re = 72000$. Refer Figure 4.14 for numbering.

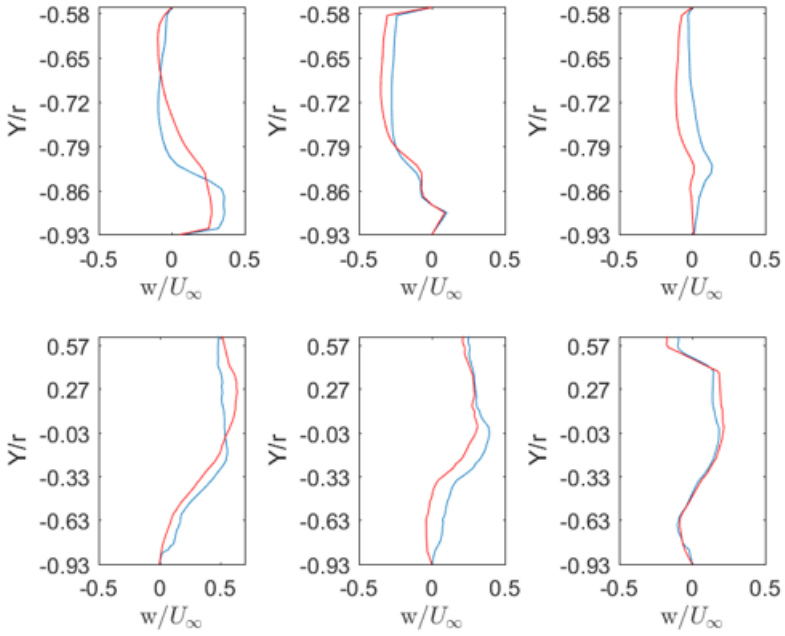

Figure 4.21: Scaled w velocity along the different lines indicated earlier. The red line corresponds to $Re = 9000$ and blue line corresponds to $Re = 72000$. Refer Figure 4.14 for numbering.

X/D = 1.5

Figure 4.22 shows the in-plane velocity vectors at $X/D = 1.5$ for the two Reynolds numbers. It can be seen that, similar to the plane $X/D = 1$, vortex L and B are

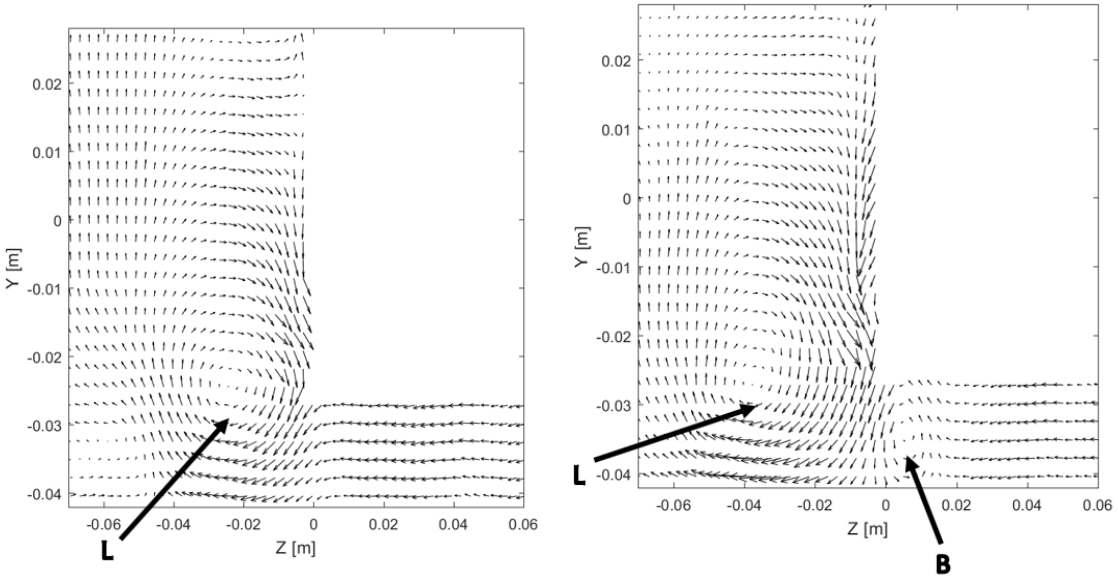

(a) $Re = 9000$ (b) $Re = 72000$

Figure 4.22: In-plane velocity vectors at $X/D = 1.5$ downstream of the wheel. The flow is into the plane.

observed in *Case2* while only L vortex is observed in *Case1*. However, the position of the L vortex in *Case2* has moved further away from the body compared with *Case2* at $X/D = 1$, whereas in *Case1*, the position of the L vortex remains more or less the same. From the observations at the three downstream planes in *Case2*, it appears that the L vortex with respect to the streamwise direction is at an outward angle. Figures 4.23-4.25 compares the velocity between the two Reynolds number along the different lines indicated.

Comparison of the streamwise velocity in Figure 4.23 shows that, in the lines 4-6, the streamwise velocity is higher for *Case2* compared to *Case1* near the ground, which is where the L vortex is present. The difference in velocity decreases with the increase in height upto $Y0$ m where maximum streamwise velocity is observed. Beyond this height, the velocity in *Case2* is slightly higher than *Case1*. In the underbody region (lines 1-3), the streamwise velocity is higher in *Case2* compared to *Case1* along the lines 1 and 3 but lower along line 2. The wall normal velocity, shown in Figure 4.24, is low along all the lines. In the lines 3 and 4, negative wall normal velocity is observed closer to the ground. This is due to the influence of the ground vortex in *Case1* and due to both the ground and B vortex in *Case2*. The spanwise velocity, shown in Figure 4.25, is higher in *Case1* compared to *Case2* in the underbody region in terms of the magnitude. This can be attributed to the absence of the B vortex in *Case1*. The negative spanwise velocity indicates movement of the flow towards the L vortex. In the outer regions, the spanwise velocity in both the cases are similar. The sharp gradients observed in Figures 4.24 and 4.25, especially near the underbody of the car are caused due to reflections from the body surface leading to inaccurate velocity vectors.

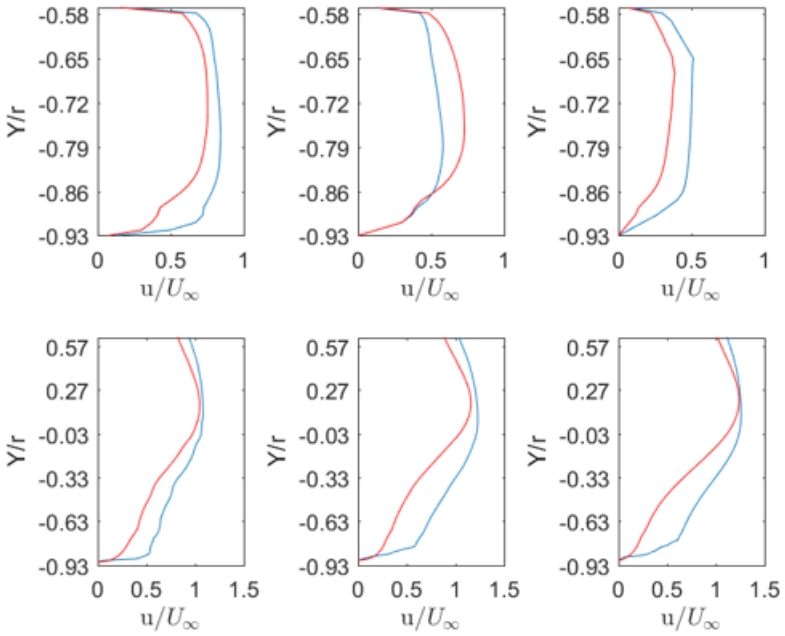

Figure 4.23: Scaled u velocity along the different lines indicated earlier. The red line corresponds to $Re = 9000$ and blue line corresponds to $Re = 72000$. Refer Figure 4.14 for numbering.

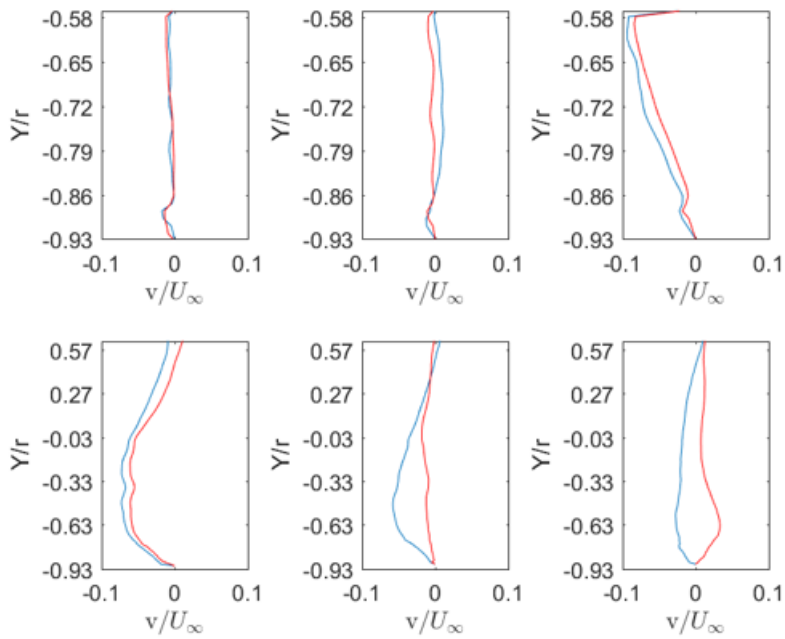

Figure 4.24: Scaled v velocity along the different lines indicated earlier. The red line corresponds to $Re = 9000$ and blue line corresponds to $Re = 72000$. Refer Figure 4.14 for numbering.

To summarize,

(i) While a quantitative similarity does not exist between the two cases a qualitative

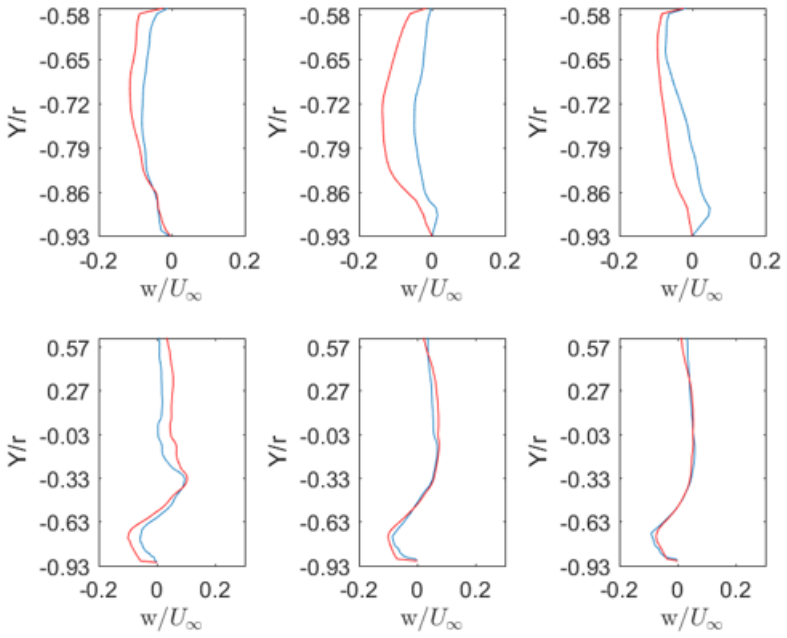

Figure 4.25: Scaled w velocity along the different lines indicated earlier. The red line corresponds to $Re = 9000$ and blue line corresponds to $Re = 72000$. Refer Figure 4.14 for numbering.

similarity in the velocity profiles can be observed.

(ii) Some differences in the velocity profiles between the two cases were present and this could be attributed to the presence of the B vortex in *Case2*.

(iii) The advection of the ground vortex L in the streamwise direction was found to be at an outward angle away from the body in *Case2* while in *Case1* the ground vortex L remained close to the body.

While the comparison of velocity profiles between the two cases was performed in the previous section, the comparison of the velocity profiles along different planes for a given Reynolds number will be considered in figures 4.26 - 4.28 and in Appendix C.

Figure 4.26 shows the streamwise velocity comparison for *Case1* at different distances downstream of the wheel. It can be seen that in the outer lines 5 and 6, the streamwise velocity profile is nearly similar in all the planes with maximum velocity observed at a height of y/d = 0. Above this height, the velocity decreases along the lines 4,5 and 6. This behavior could be explained by looking at Figure 4.6a obtained with planar PIV at a distance of 1.5 cm from the side of the body. It appears that the streak of high velocity observed in Figure 4.6a, which corresponds to a height of y/d = 0, extends to a similar profile downstream of the wheel up to the distance of $X/D = 1.5$. Above the height of y/d = 0, the velocity decreases, similar to Figure 4.6a.

Closer to the body (along line 4) the streamwise velocity is similar in $X/D = 0.6$ and $X/D = 1$ while the velocity at $X/D = 1.5$ is much higher. The streamwise velocity profile observed along this line is similar to the one along the outer lines (lines 5 and 6) with the magnitude being the only difference. The difference could be due to the influence of flow exiting the wheelhouse which is felt up to the $X/D = 1$ plane reducing

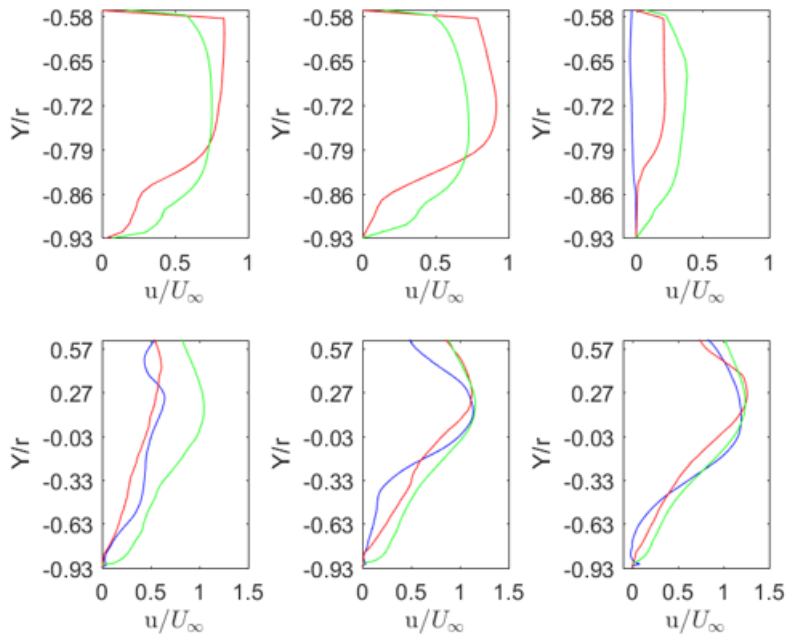

Figure 4.26: Scaled u velocity along the different lines indicated earlier for Re = 9000. The blue line corresponds to $X/D = 0.6$, red line corresponds to $X/D = 1$ and green line corresponds to $X/D = 1.5$. The blue line is not present for lines 1 and 2 since no information is available along these lines at $X/D = 0.6$. Refer Figure 4.14 for numbering.

the streamwise velocity. Also, looking at these profiles along lines 4-6, it can be said that a streak of high velocity exists at a height around the mid of the wheel extending quite far into the wake.

Figure 4.27 shows the wall normal velocity comparison for *Case1* at different distances downstream of the wheel. It can be seen that the wall normal velocity is low in magnitude except at $X/D = 0.6$ along line 4, where due to the three dimensional nature of the flow in the wheelhouse region, a high magnitude of wall normal velocity exists.

Figure 4.28 shows the spanwise velocity comparison for *Case1* at different distances downstream of the wheel. It can be seen that in the immediate wake of the wheel, along the outer lines 4-6 at $X/D = 0.6$, a significant spanwise velocity exists. The magnitude of the spanwise velocity decreases with increase in the distance from the side of the body. The significant outflow at $X/D = 0.6$ changes to inflow at $X/D = 1$ (reversal in the sign of spanwise velocity) and further downstream, the spanwise velocity becomes negligible at the outer lines. In the underbody region (lines 1-3) at the planes $X/D = 1$ and 1.5, a negative spanwise velocity is observed. This is because of the ground vortex near the side of the body which causes a suction towards it. The sharp gradients observed in Figures 4.26, 4.27 and 4.28, especially near the underbody of the car are caused due to reflections from the body surface leading to inaccurate velocity vectors.

The velocity profiles at different distances downstream of the wheel for *Case2* are

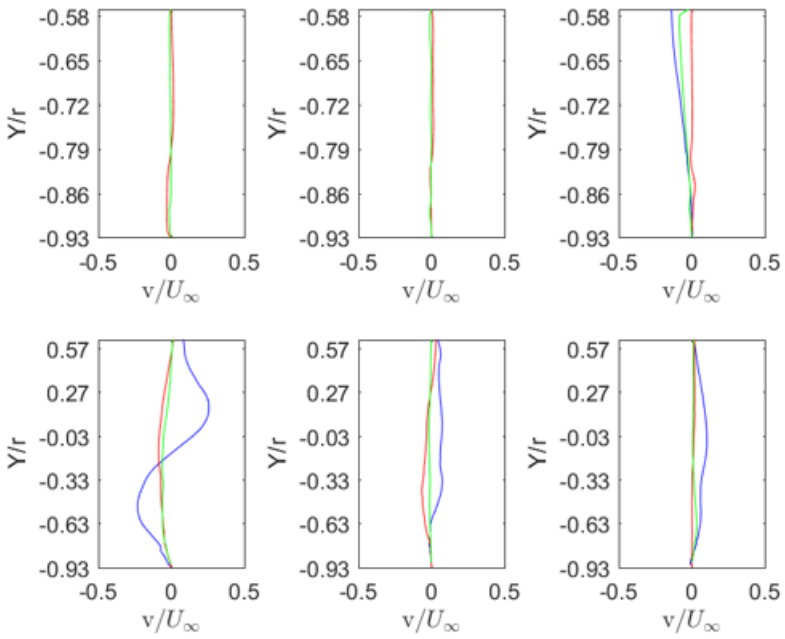

Figure 4.27: Scaled v velocity along the different lines indicated earlier for $Re = 9000$. The blue line corresponds to $X/D = 0.6$, red line corresponds to $X/D = 1$ and green line corresponds to $X/D = 1.5$. Note the different velocity scales. Refer Figure 4.14 for numbering.

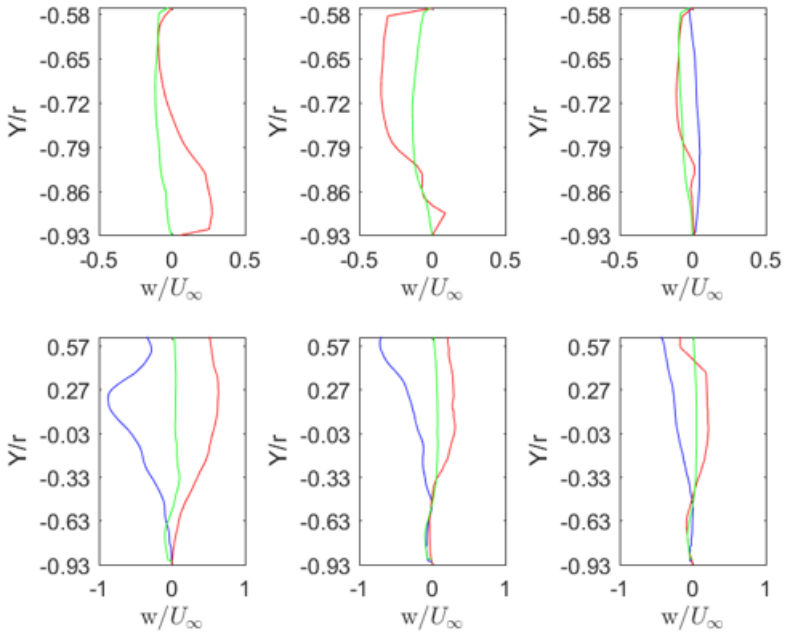

Figure 4.28: Scaled w velocity along the different lines indicated earlier for $Re = 9000$. The blue line corresponds to $X/D = 0.6$, red line corresponds to $X/D = 1$ and green line corresponds to $X/D = 1.5$. Refer Figure 4.14 for numbering.

found to be similar to *Case1* (refer Appendix C).

To summarize,

(i) A streak of high velocity exists at a height close to y/d = 0 that extends downstream until $X/D = 1.5$.

(ii) When considering the flow in the underbody, an outflow is observed across all the planes in the wake of the wheel. The same cannot be said for the flow along the outer lines (4-6).

(iii) Along the outer lines, the strong outflow observed at $X/D = 0.6$ turns into inflow at $X/D = 1$. Eventually, at $X/D = 1.5$, the spanwise velocity becomes negligible i.e. the flow is aligned with the freestream.

Turbulence Intensity

Figure 4.29 shows the root mean square of the spanwise velocity fluctuations at all the stereo planes. It is clear from the figure that the turbulence intensity in the spanwise direction is highest in the $X/D = 0.6$ which is in the immediate wake of the wheel. Downstream of this plane at $X/D = 1$,a high turbulence intensity is observed near the ground vortex L in both the cases. Further downstream at $X/D = 1.5$ the turbulence intensity is quite low. In the $X/D = 0.6$ plane, the turbulence intensity is higher closer to the outer edge ($Z0$) probably caused by the shear between the outflow from the wheelhouse and the freestream velocity. The discontinuity in the turbulence intensity observed in the shape of an arc between Z-0.01 m and Z-0.02 m at the measurement plane $X/D = 0.6$ is caused by the strong reflection from the outer edge of the wheel.

Figure 4.30 shows the root mean square of the wall normal velocity fluctuations for all the stereo planes. Similar to the turbulence intensity in the spanwise direction (Figure 4.29), the turbulence intensity is higher at $X/D = 0.6$ when compared to other planes downstream of the wheel. Also, the concentration of turbulence intensity in the shape of an arc between Z-0.01 m and Z-0.02 m at the measurement plane $X/D = 0.6$ is caused by a strong reflection from the outer edge of the wheel and thus is not physical.

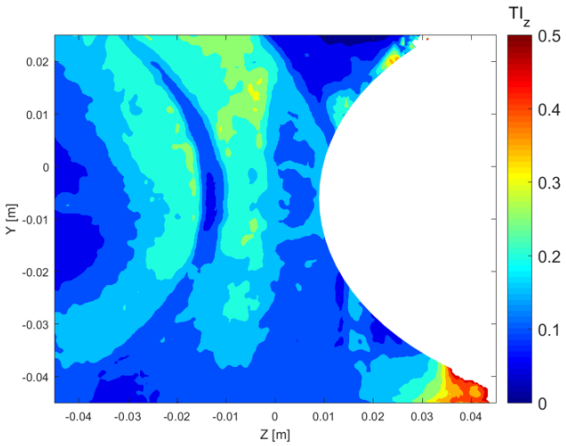

(a) $X/D = 0.6$, $Re = 9000$

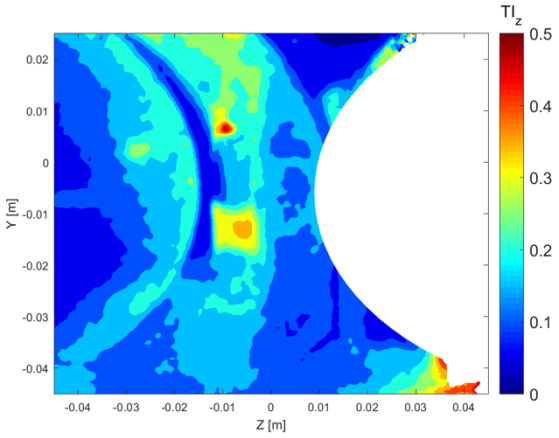

(b) $X/D = 0.6$, $Re = 72000$

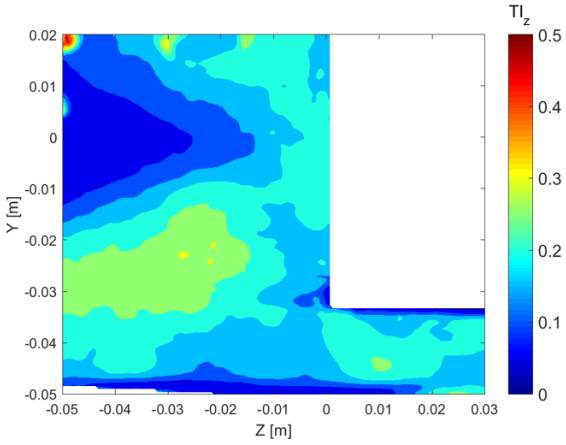

(c) $X/D = 1$, $Re = 9000$

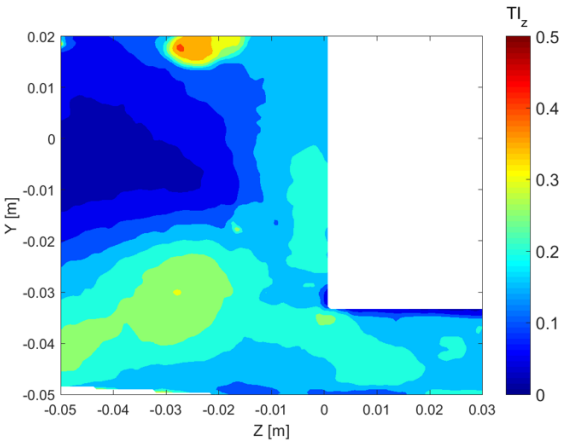

(d) $X/D = 1$, $Re = 72000$

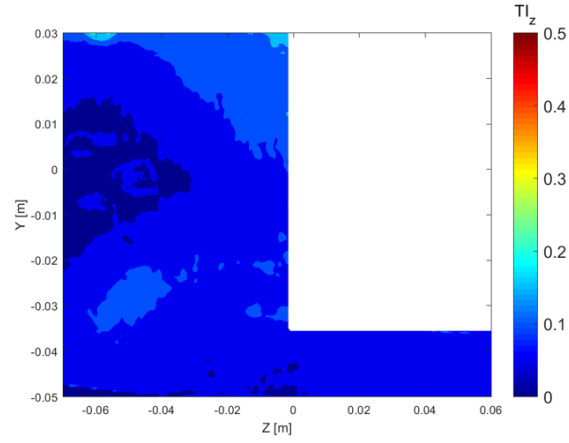

(e) $X/D = 1.5$, $Re = 9000$

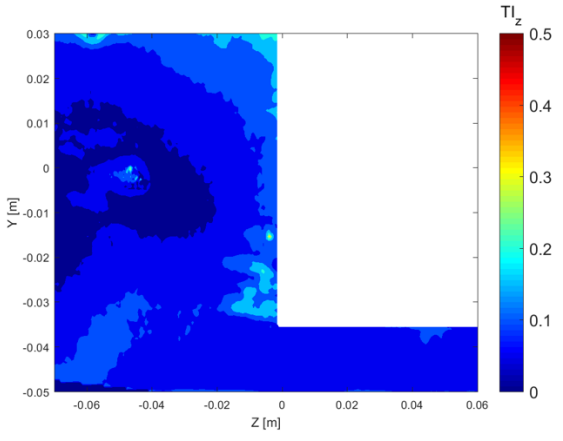

(f) $X/D = 1.5$, $Re = 72000$

Figure 4.29: Contours of Turbulence Intensity (TI) in the z direction based on freestream velocity. The flow is into the plane.

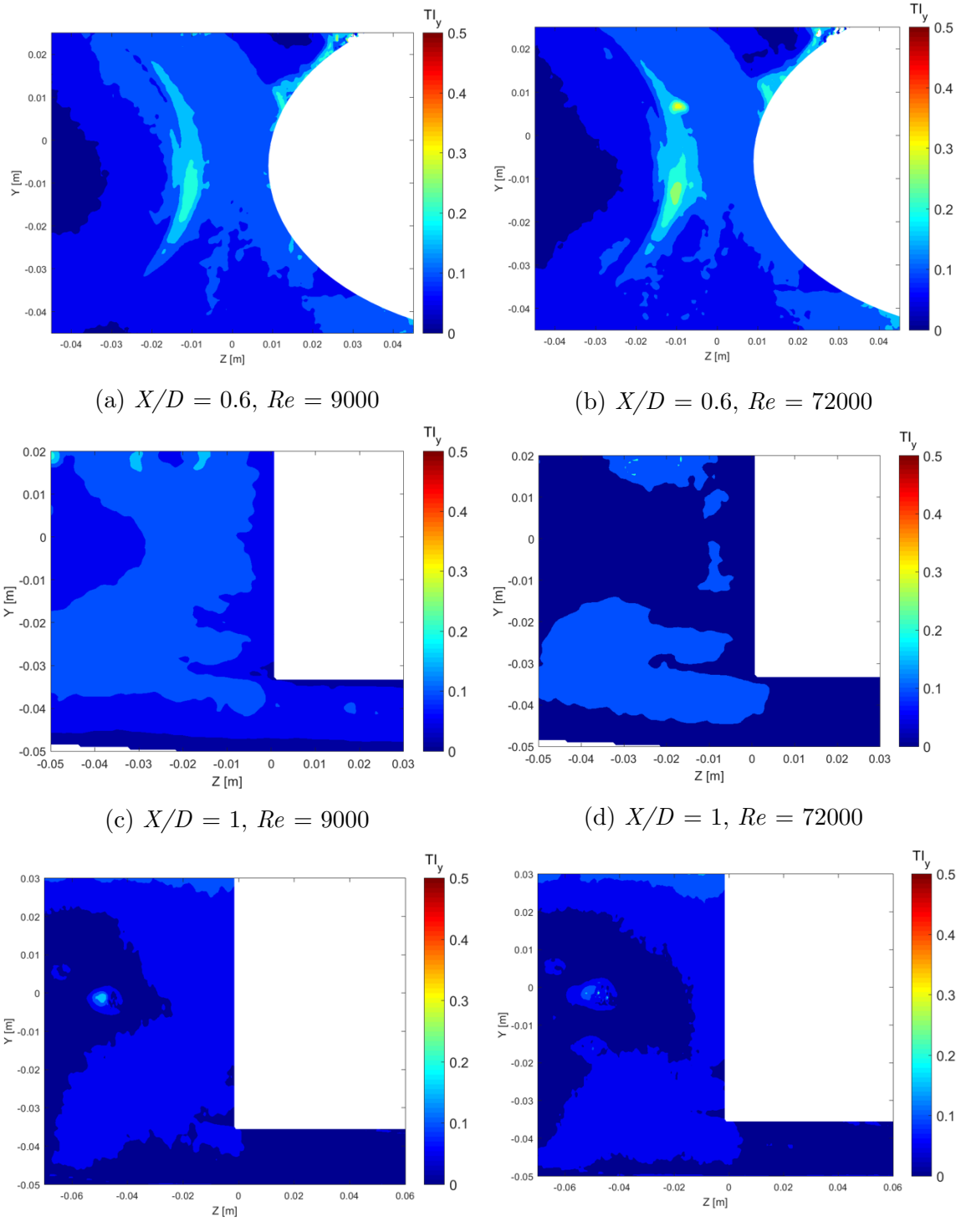

(a) $X/D = 0.6$, $Re = 9000$

(b) $X/D = 0.6$, $Re = 72000$

(c) $X/D = 1$, $Re = 9000$

(d) $X/D = 1$, $Re = 72000$

(e) $X/D = 1.5$, $Re = 9000$

(f) $X/D = 1.5$, $Re = 72000$

Figure 4.30: Contours of Turbulence Intensity (TI) in the y direction based on freestream velocity. The flow is into the plane.

4.3 Vortex Generator

A brief introduction into Vortex Generators (VG) was provided earlier in Chapter 1. In this section, the effect of the VG on the flow will be determined. This is done in the form of a comparison of velocity profiles along the lines shown in Figure 4.13. Measurements with a VG were taken at $X/D = 0.6$ and $X/D = 1.5$. The measurement at $X/D = 1.5$ was done for *Case1* only while the measurement at $X/D = 0.6$ was done for both *Case1* and *Case2*. The purpose of adding a VG, upstream of the wheel, is to influence the flow impinging on the wheel surface. The scope of using a VG in this work is to determine if there is any effect on the flow field from the vortices shed from the VG, particularly on the ground vortex shed from the contact patch. To investigate this effect, velocity fields between the configuration with and without VG are compared. Before dwelling into the results, the description of the VG, including its shape and position underneath the car body, is provided first.

4.3.1 VG Geometry

For the present investigation, the geometry of the VG was chosen to be rectangular which is the simplest amongst others. The geometry of the VG is shown in Figure 4.31. The dimensions of the VG are provided in Table 4.1. The length of the VG was chosen to be 5 times its height and the VG was positioned at an angle of 10°to the incoming flow (the angle of the incoming flow was shown in Figure 4.11). The leading edge of the VG was positioned at a distance of *-1D* upstream of the wheel center and 5 mm from the side of the body in the spanwise diretion. The VG was glued to the underbody of the car.

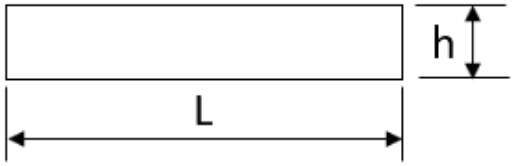

(a) Geometry of the VG

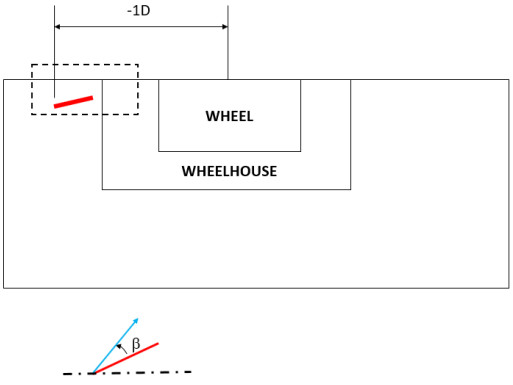

(b) Location of the VG

Figure 4.31: Geometry and position of the vortex generator. β refers to angle between the VG and the freestream. The flow is from left to right in (b).

Table 4.1: Geometry of the VG

VG dimensions	
L (mm)	15
h (mm)	3
β (°)	10
c (mm)	13

4.3.2 Velocity comparison

The velocity profiles between the configuration with and without VG are compared here at the planes $X/D = 0.6$ and 1.5 to determine the effect of the VG on the flow.

***X/D* = 0.6**

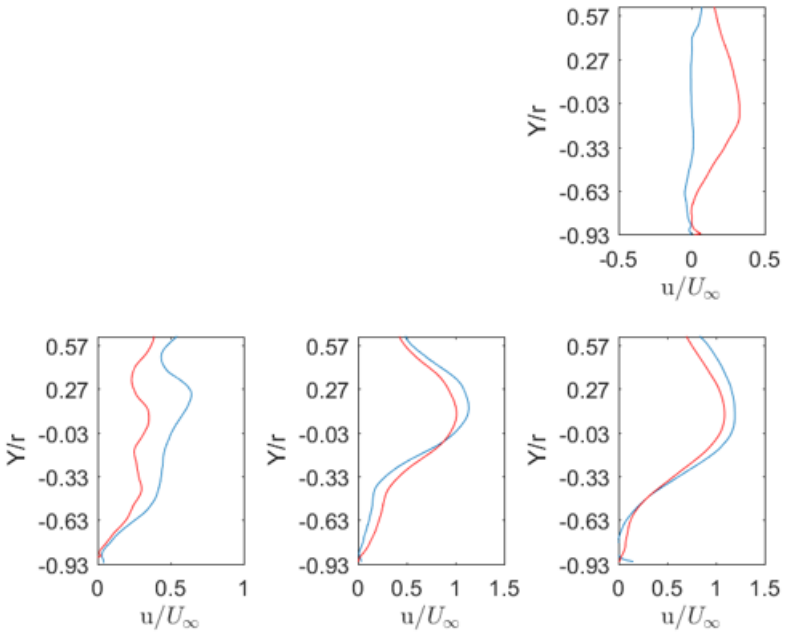

Figure 4.32: u velocity along the different lines indicated earlier for $Re = 9000$ at $X/D = 0.6$. The blue line corresponds to the measurement without VG and the red line corresponds to the measurement with VG. Refer Figure 4.14 for numbering.

Figure 4.32 shows the comparison of streamwise velocity for *Case1* between the configuration with VG and without VG at $X/D = 0.6$. It can be seen that along the lines 3 and 4, a significant difference in the streamwise velocity exists. While the configuration without VG shows a negligible streamwise velocity along the outer edge (line 3), the configuration with VG shows a higher streamwise velocity along the outer edge. Similarly, along the line 4, the streamwise velocity in the configuration with VG is lower compared to the configuration without VG. The streamwise velocity profiles are identical along the lines 5 and 6. The effect on only the lines 3 and 4 could suggest

that the flow inside the wheelhouse is quite different in the configuration with VG compared to the configuration without VG.

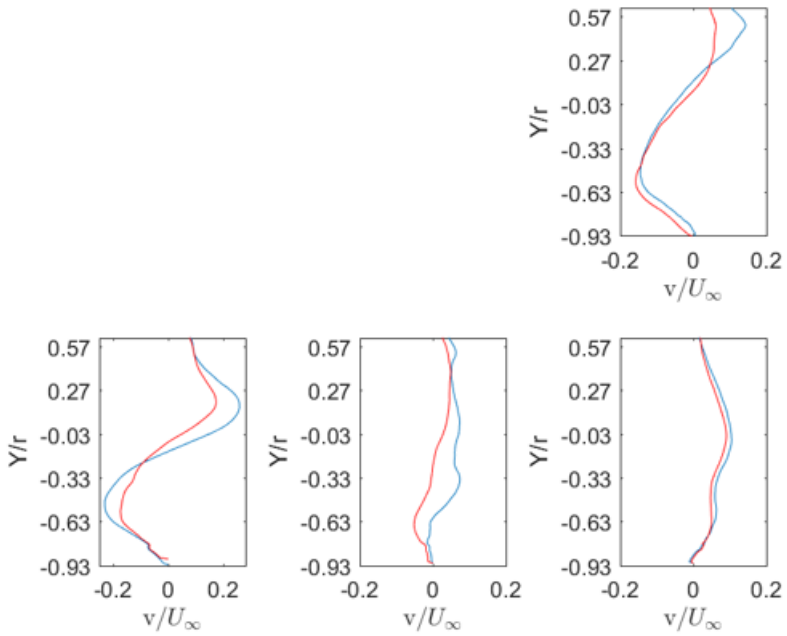

Figure 4.33: v velocity along the different lines indicated earlier for $Re = 9000$ at $X/D = 0.6$. The blue line corresponds to the measurement without VG and the red line corresponds to the measurement with VG. Refer Figure 4.14 for numbering.

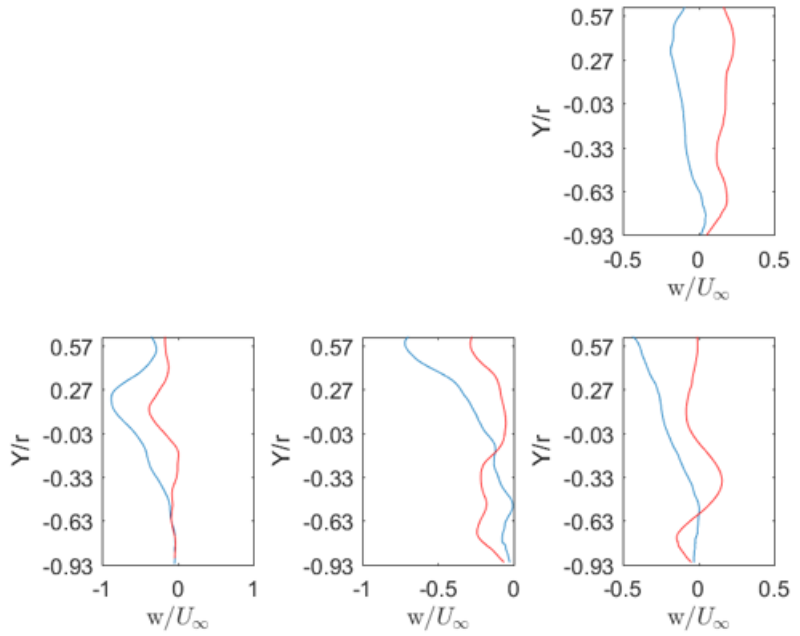

Figure 4.34: w velocity along the different lines indicated earlier for $Re = 9000$ at $X/D = 0.6$. The blue line corresponds to the measurement without VG and the red line corresponds to the measurement with VG. Refer Figure 4.14 for numbering.

Comparison of the wall normal velocity, shown in Figure 4.33, indicates that the wall normal velocity is nearly the same in both the configurations. However, the spanwise velocity, shown in Figure 4.34, differs between the two configurations. The particularly striking feature, in the configuration with VG, is that along the outer edge (line 3), there is inflow into the wheelhouse unlike in the configuration without VG where an outflow was observed. This points to a significant difference in the flow behavior inside the wheelhouse. Similarly, along the lines 4-6 the spanwise velocity in the configuration with VG is significantly lower compared to the configuration without VG.

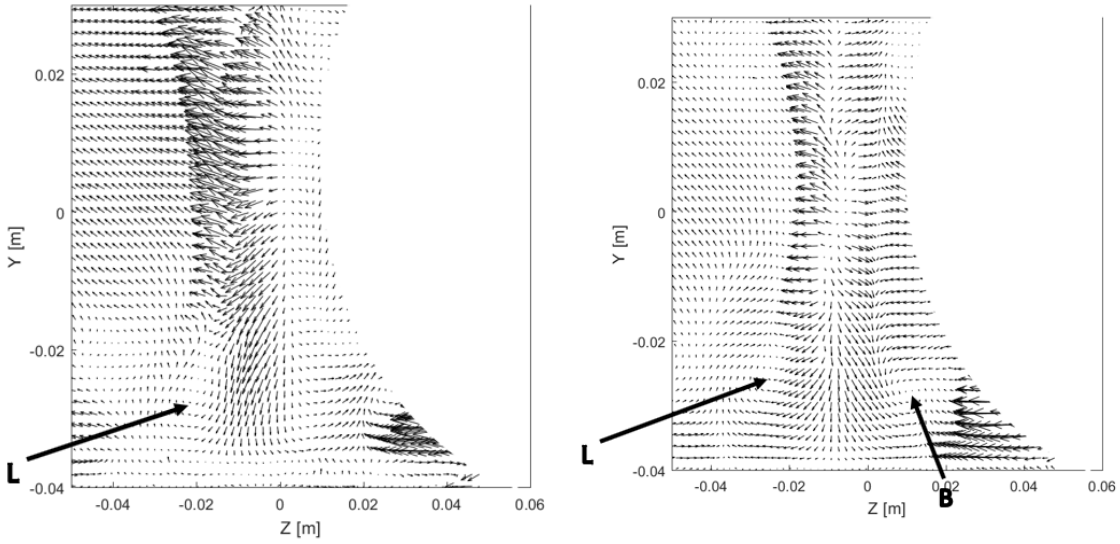

(a) Without VG

(b) With VG

Figure 4.35: In plane velocity vectors at $X/D = 0.6$ with and without VG

Comparing the in-plane velocity vectors, shown in Figure 4.35 between the configuration with and without VG, it can be seen that, in addition to the ground vortex, the B vortex (explained earlier) is also observed. The ground vortex, in the configuration with VG, is also slightly shifted to the left compared to the configuration without VG. The flow inside the wheelhouse (z > 0) in Figure 4.35b, is such that, below the height of Y0.0 m, the flow is downwards and above this height there is an upward flow possibly following the rotation of the wheel. Also, the velocity magnitude seen at the height Y > 0.02 m is greatly reduced with the addition of the VG. The effect on the flow inside the wheelhouse could be because of the incidence angle of the VG with respect to the incoming flow which, in this case is pointing inwards. Thus, more fluid is probably directed into the wheelhouse that could help explain the different behavior of the flow inside the wheelhouse.

Figure 4.36 shows the contours of swirling strength at $X/D = 0.6$. Swirling strength is defined as the absolute value of the imaginary part of the complex eigenvalue of the velocity gradient tensor [25]. A higher swirling strength corresponds to a stronger vortex. It is seen that the ground vortex L is displaced to the left with the addition of VG and also that the strength of the L vortex is slightly reduced with VG when compared to the configuration without VG.

The wake velocity profiles were also compared for *Case2* (Refer Appendix D). However,

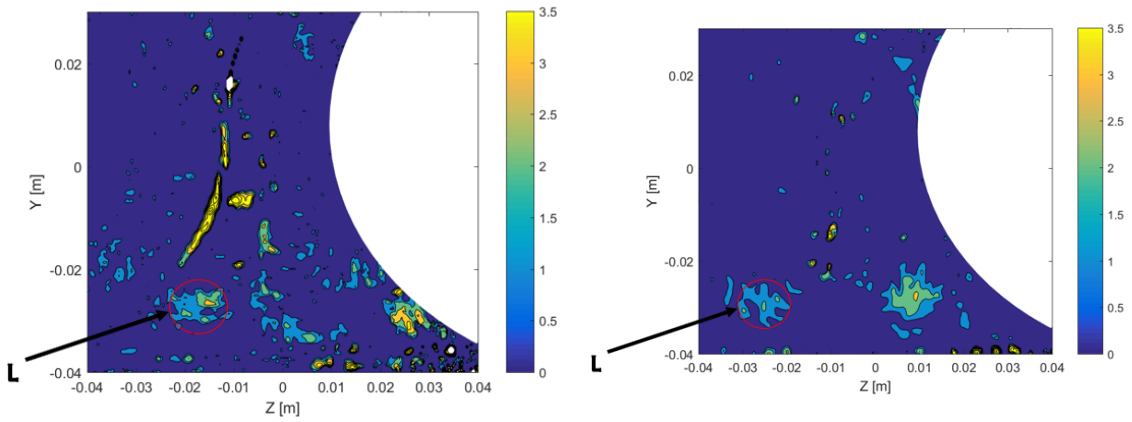

(a) Without VG

(b) With VG

Figure 4.36: Contours of swirling strength at $X/D = 0.6$ with and without VG

the velocity profiles were nearly the same between the configuration with and without VG.

$X/D = 1.5$

Figure 4.37 shows the streamwise velocity comparison for *Case1* along the different lines at $X/D = 1.5$. It is seen that, the streamwise velocities are almost similar along the outer lines 4-6. Comparing the velocity profiles at $X/D = 1.5$ with that of $X/D = 0.6$ (Figure 4.32) for *Case1*, it can be observed that the streamwise velocities along the lines 3 and 4 are similar at $X/D = 1.5$. However, with VG, the magnitude of the streamwise velocity is lower in the underbody region compared to the one without VG.

Comparing the wall normal velocity between the configurations, shown in Figure 4.38, similar behavior to streamwise velocity is observed (refer Figure 4.37). Without VG, the wall normal velocity was found to be negligible. However, with VG a small component of velocity in the underbody region was observed. The spanwise velocity shown in Figure 4.39 exhibits a different behavior. Along the line 2, an inflow is observed with VG and an outflow without VG indicated by the sign of the spanwise velocity. The sharp gradients observed in Figures 4.37, 4.38 and 4.39, especially near the underbody of the car are caused due to reflections from the body surface leading to inaccurate velocity vectors.

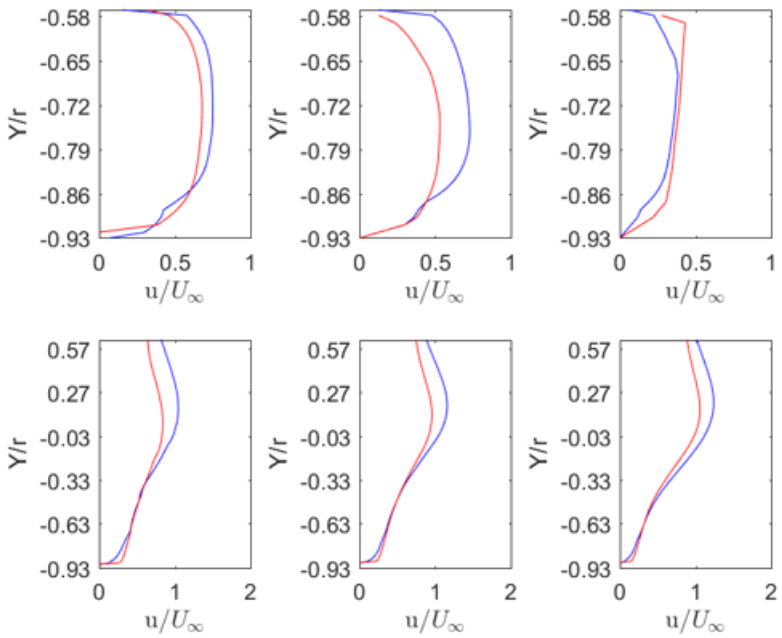

Figure 4.37: Streamwise velocity, u, along the different lines indicated earlier for *Re* = 9000 at $X/D = 1.5$. The blue line corresponds to the measurement without VG and the red line corresponds to the measurement with VG. Refer Figure 4.14 for numbering.

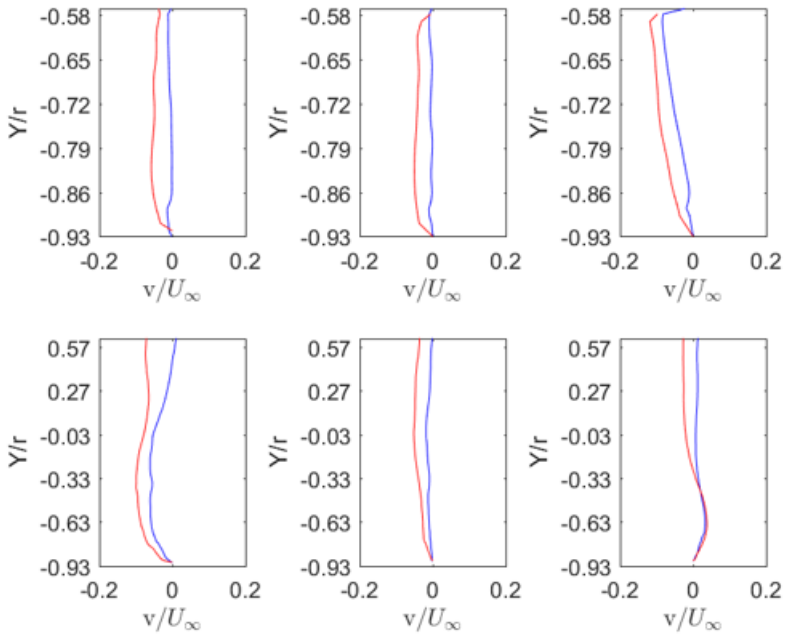

Figure 4.38: Wall normal velocity, v, along the different lines indicated earlier for *Re* = 9000 $X/D = 1.5$. The blue line corresponds to the measurement without VG and the red line corresponds to the measurement with VG. Refer Figure 4.14 for numbering.

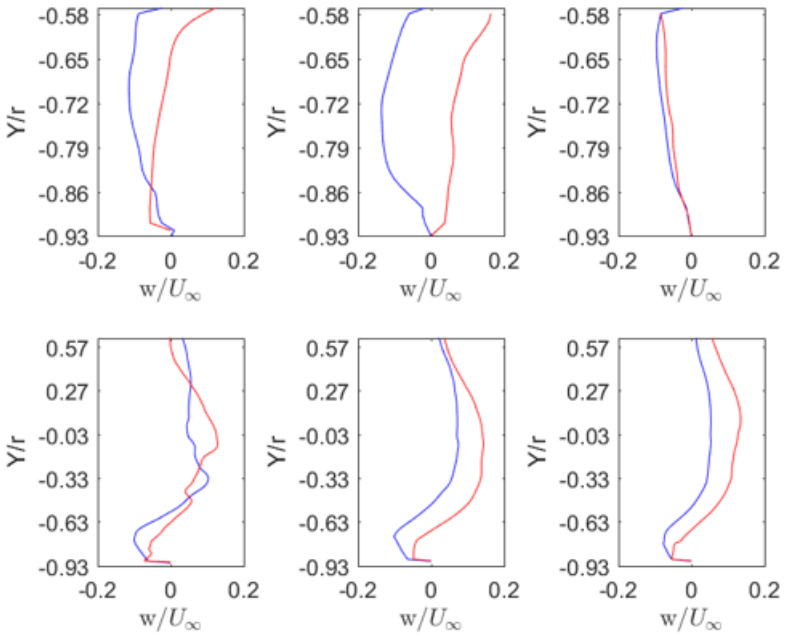

Figure 4.39: Spanwise velocity, w, along the different lines indicated earlier for Re = 9000 X/D = 1.5. The blue line corresponds to the measurement without VG and the red line corresponds to the measurement with VG. Refer Figure 4.14 for numbering.

Figure 4.40 shows the contour of swirling strength at X/D = 1.5 for both the configurations. By comparing the swirling strength, in the region around the L vortex, the configuration with VG is found to have a slightly higher swirling strength with respect to the configuration without VG. This is in contrast to the X/D = 0.6 plane where the configuration without VG had a slightly higher swirling strength. It appears that in between the X/D = 0.6 and 1.5 plane, the ground vortex has become stronger. Nonetheless, it can be concluded that the strength of the ground vortex is not significantly affected.

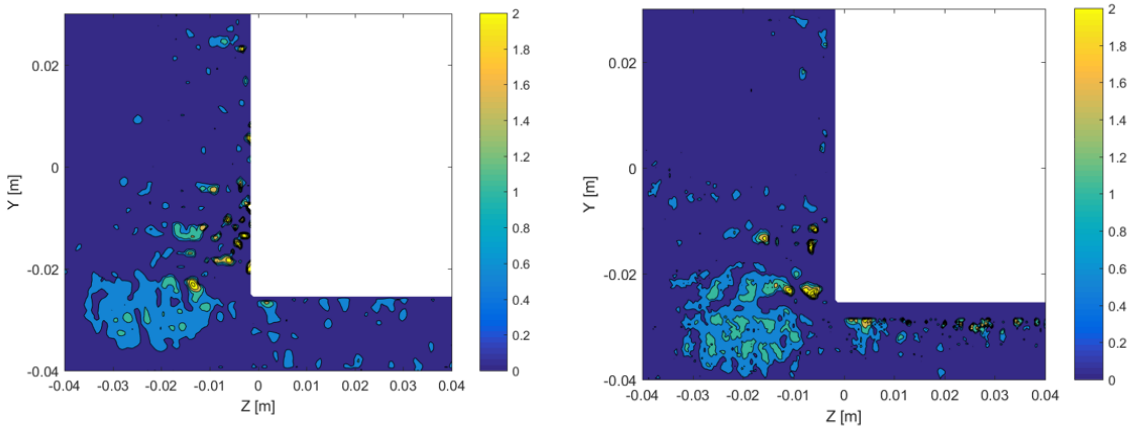

(a) Without VG

(b) With VG

Figure 4.40: Contours of swirling strength with and without VG for Re = 9000.

To summarize,

(i) The addition of VG did have an effect on the flow for *Case1* (Re = 9000).

(ii) At $X/D = 0.6$, the strong outflow that was observed for *Case1* without VG along the outer edge of the wheel (line 3), which became an inflow with VG.

(iii) The addition of VG was found to increase the streamwise velocity along the outer edge.

(iv) The spanwise velocity showed the largest difference when comparing the velocity profile with and without VG at $X/D = 1.5$.

(v) Comparison of the swirling strength of the ground vortex L did not show any significant difference.

4.4 Comparison with LES

One of the objectives of the present study is to provide data for the validation of LES. In this section, the results from the present study are compared with the LES results of [1]. The comparison is made for the Reynolds number of 9000. Measurements at the wheel mid-plane from planar PIV and at $X/D = 1.5$ from stereo PIV are used for a quantitative comparison of the velocities obtained at the above mentioned locations.

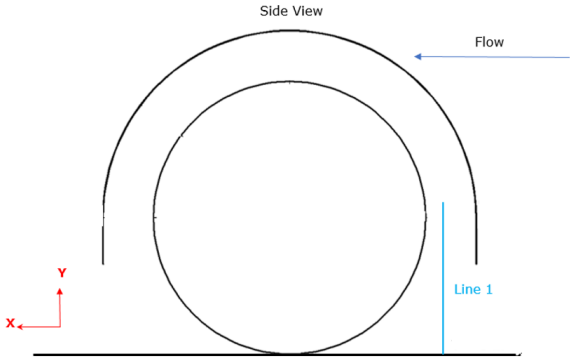

Figure 4.41: Schematic of the vertical line at wheel mid-plane along which the streamwise velocity and the velocity magnitude are compared. The figure is taken from [1]. Flow is from right to left.

For the measurement at the wheel mid-plane, a vertical line between upstream of the wheel and the wheelhouse is taken as shown in Figure 4.41 along which the streamwise velocity and the velocity magnitude are compared.

Figure 4.42 shows the comparison between the PIV and LES result for the streamwise velocity and velocity magnitude along the vertical line shown in Figure 4.41. The comparison shows a good agreement in the velocity profile between the experimental and simulation results. In the underbody region (-0.026 m $< Y <$ -0.042 m), the maximum deviation in the velocity magnitude between the PIV and LES result is 5%. However, around the height of Y = -0.01 m, the deviation is higher at approximately 25%. The higher velocity magnitude in the PIV at this height when compared to the

LES could be due to the slight eccentric rotation of the wheel in the experimental setup as mentioned earlier in Chapter 3. This could have caused the impinging flow to be more unstable compared to the LES resulting in a higher velocity.

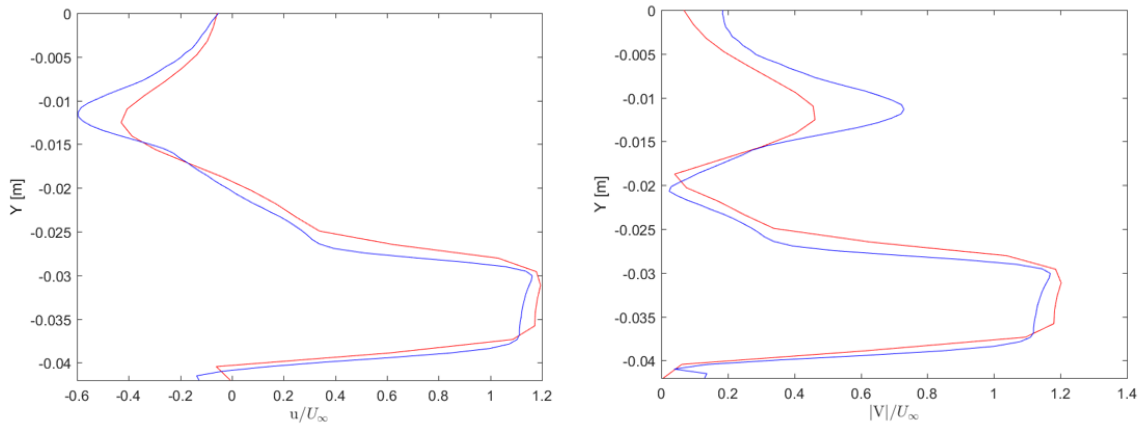

(a) Comparison of the streamwise velocity (b) Comparison of the velocity magnitude

Figure 4.42: Comparison of the streamwise velocity and velocity magnitude along the vertical line shown in Figure 4.41 between the PIV and LES results. The blue line represents the result from PIV and the red line represents the result from LES.

Figures 4.43-4.45 show the comparison of components of velocity at $X/D = 1.5$. The sharp gradients observed in these figures for the results from PIV, especially near the underbody of the car are caused due to reflections from the body surface leading to inaccurate velocity vectors.

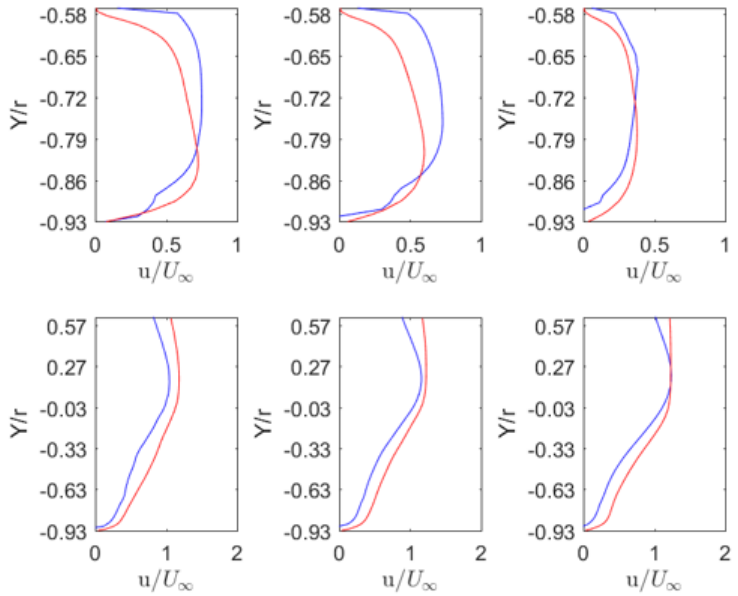

Figure 4.43: Scaled u velocity along the different lines shown in Figure 4.13. The blue line represents the result from PIV and the red line represents the result from LES. Refer Figure 4.14 for numbering.

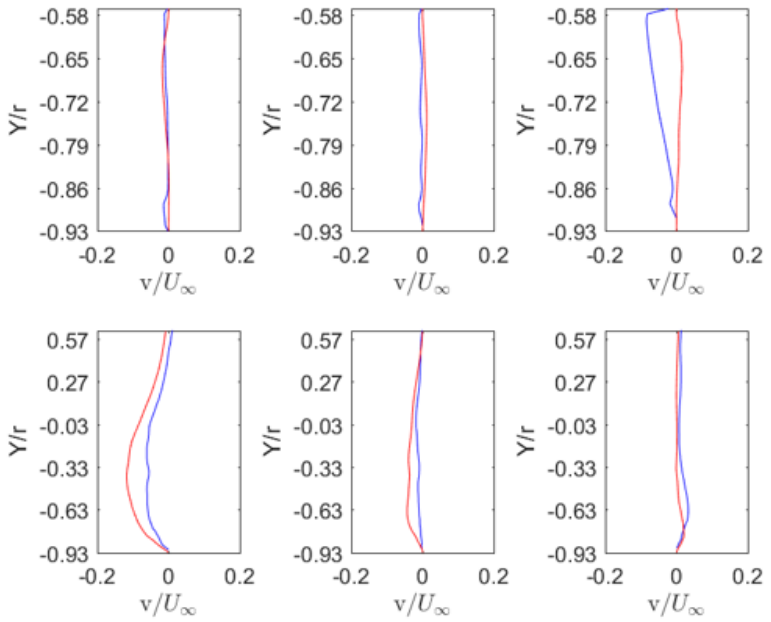

Figure 4.44: Scaled v velocity along the different lines shown in Figure 4.13. The blue line represents the result from PIV and the red line represents the result from LES. Refer Figure 4.14 for numbering.

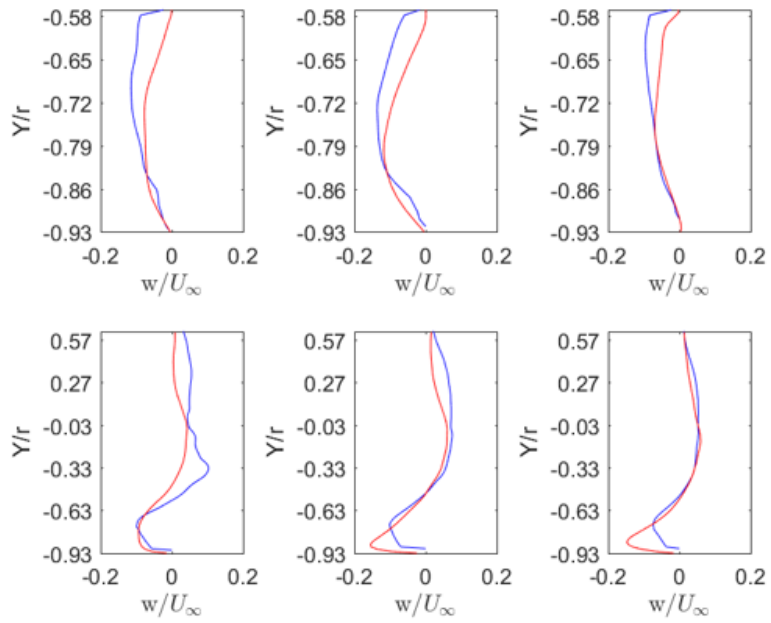

Figure 4.45: Scaled w velocity along the different lines shown in Figure 4.13. The blue line represents the result from PIV and the red line represents the result from LES. Refer Figure 4.14 for numbering.

It can be seen that all three components of velocity show a good agreement between the PIV and LES result. The maximum deviation in the streamwise velocity is 20% along line 2 in the underbody while the maximum deviation in the wall normal and spanwise component of the velocity are 6% and 8% respectively observed along line 4.

Chapter 5

Conclusions and Recommendations

5.1 Conclusions

A generic simplified car body with a wheel and a wheelhouse has been designed to study the flow behavior inside the wheelhouse as well as in the wake of the wheel. The study has been done for a rotating wheel and stationary ground configuration. Planar Particle Image Velocimetry (PIV) and Stereoscopic Particle Image Velocimetry have been used to study the flow field inside the wheelhouse and in the wake respectively. The investigation has been done for the Reynolds number based on wheel diameter of 9000 (*Case1*) and 72000 (*Case2*). The lower Reynolds number case provided data for the validation of LES simulation by Viswanathan [1].

Using planar PIV, the measurements were done at planes both inside the wheelhouse (three in total which corresponds to the wheel inner edge, the wheel centerline and the wheel outer edge) and outside the wheelhouse (one plane at 1.5 cm from the side of the body). Several vortices were observed at the planes inside the wheelhouse, which depended on the Reynolds number of the flow. The flow was found to undergo acceleration before entering the wheelhouse. The behavior of the flow upon entering the wheelhouse was different along different planes and also depended on the Reynolds number. In *Case1*, there was no flow towards the top of the wheelhouse in the wheel centerline and the wheel inner edge plane. Instead, the flow was found to bifurcate at a point near the top of the wheel with one part flowing in the direction of rotation of the wheel and the other flowing in the opposite direction. This behavior was observed in *Case2* only at the wheel inner edge. A strong outflow was observed in both the cases at the wheel outer edge plane. In the plane outside the wheelhouse, flow separation was observed at the side of the body. A streak of high velocity was observed above the ground vortex in both the cases.

Using stereo PIV, the measurements were taken both upstream (one plane) and downstream of the wheel (three planes). The measurement upstream of the wheel was used to determine the angle of the incoming flow (yaw angle) as it approaches the wheel in the underbody. The angle at the outer edge of the body was found to be around 20°. The angle was found to increase till 1 cm in the positive spanwise direction before steadily decreasing. The yaw angle was found to be almost the same for both the Reynolds numbers. Measurements in the wake of the wheel were done at X/D

= 0.6, 1 and 1.5. The behavior of the flow was again found to be dependent on the Reynolds number. In the immediate wake of the wheel (X/D = 0.6), three vortices were observed in *Case2* referred to as vortex L, B and E (refer Figure 4.12b), while only one vortex namely vortex L was observed in *Case1* (refer Figure 4.12a). It is expected that the B and E vortex in *Case1* are visualized better in a different plane. Further downstream at X/D = 1 and 1.5, the vortex E was not observed, in both the cases, indicating that it dissipated quickly. However, vortex L and B were observed in the downstream planes at X/D = 1 and 1.5 in *Case2* while only vortex L was observed in *Case1* at these planes. The propagation of the ground vortex L in the streamwise direction was found to be at an outward angle away from the body in *Case2* while in *Case1* the ground vortex L remained close to the body.

For investigating the wake, the velocity components at six different vertical lines across the three planes (X/D = 0.6, 1, 1.5) were compared for each Reynolds number. A high negative spanwise velocity indicating outflow at X/D = 0.6 was observed, which turned to inflow (positive spanwise velocity) at X/D = 1 before becoming aligned with the freestream at X/D = 1.5. Also, the streak of high velocity observed using planar PIV at 1.5 cm from the side of the body was found to extend upto 1.5D downstream of the wheel. This high velocity region was found to exist in the wake at a height close to the center of the wheel. The velocity profiles across these vertical lines were also compared between the two Reynolds numbers. A quantitative similarity in the velocity profiles does not exist between the two cases. However, a qualitative similarity could be observed.

Finally, the effect of a Vortex Generator (VG) on the flow behavior was studied. The VG was positioned 1D upstream of the wheel at an angle of 10°with respect to the incoming flow. Measurements at X/D = 0.6 showed a different flow behavior when compared to the configuration without VG for *Case1*. The strong outflow that was observed for *Case1* without VG along the wheel outer edge at X/D = 0.6 turned to inflow with the addition of VG. The addition of VG increased the streamwise velocity along the wheel outer edge. Also, at X/D = 1.5 the underbody flow was found to be different with the largest difference observed in the spanwise velocity. These two observations pointed to a significant change in the flow behavior inside the wheelhouse and in the underbody region. However, the strength of the ground vortex was not significantly affected. This was verified by comparing the swirling strength of the ground vortex between the configuration with and without VG. However, there was no effect on the flow with VG for *Case2*. This can either be due to the higher Reynolds number or the functioning of the VG itself was affected by the higher forces created by the higher Reynolds number.

5.2 Recommendations

The present study showcases the capabilities of undertaking PIV measurements to investigate the flow inside a wheelhouse and in the wake of a wheel and establishes the scope for PIV.

One of the shortcomings of the present work is the lack of a moving ground. An alternative i.e. boundary layer suction was considered (refer Appendix A) but not im-

plemented due to time constraints. Therefore, the first and obvious recommendation would be the implementation of the boundary layer suction system. It would be interesting to compare the flow behavior from the present work with that of a configuration with moving ground or boundary layer suction system.

Although the present work was able to capture the global flow features, some details were lost due to reflections either from the ground plane or from the body itself. This compromised the data near the ground as well as along the side of the body. Also, eliminating the shadow region observed in planar PIV, upstream and downstream of the wheel, would provide useful data such as stagnation point which could be used to further validate LES simulation.

In the present study, the VG was positioned such that the flow was directed inward and measurements were taken only in the wake of the wheel. A study on the wheelhouse flow with this configuration could be undertaken to determine the flow behavior inside the wheelhouse. Similarly the flow behavior with the VG positioned at an outward angle with respect to the incoming flow might be worth investigating.

Bibliography

[1] Veeraraghavan Viswanathan. Aerodynamics of a rotating wheel in a wheelhouse: A numerical investigation using les. Master's thesis, TU Delft, 2017.

[2] Satya P. Mavuri and Simon Watkins. The influence of wheel–housing shape on vehicle aerodynamic performance. *International Journal of Vehicle Design*, 57(2-3):275–291, 2011.

[3] A. F. Skea, P. R. Bullen, and J. Qiao. Cfd simulations and experimental measurements of the flow over a rotating wheel in a wheel arch. In *SAE Technical Paper*. SAE International, 03 2000.

[4] Tamas Regert and Tamas Lajos. Description of flow field in the wheelhouses of cars. *International Journal of Heat and Fluid Flow*, 28(4):616 – 629, 2007. Including Special Issue of Conference on Modelling Fluid Flow (CMFF'06), Budapest.

[5] Joseph Katz. Aerodynamics of race cars. *Annual Review of Fluid Mechanics*, 38(1):27–63, 2006.

[6] Fackrell J.E and J.K. Harvey. The flow field and pressure distribution of an isolated road wheel. In *Adv. Road Vehicle Aerodyn.,155-164*.

[7] A. P. Mears, R. G. Dominy, and D. B. Sims-Williams. The air flow about an exposed racing wheel. In *SAE Technical Paper*. SAE International, 12 2002.

[8] Alexander Wäschle. The influence of rotating wheels on vehicle aerodynamics - numerical and experimental investigations. In *SAE Technical Paper*. SAE International, 04 2007.

[9] Axerio-Cilies J, Issakhanian E, Jimenez J, and Iaccarino G. An aerodynamic investigation of an isolated stationary formula 1 wheel assembly. *ASME. J. Fluids Eng.*, 2012.

[10] McManus J and Zhang X. A computational study of the flow around an isolated wheel in contact with the ground. *ASME. J. Fluids Eng.*, 2005.

[11] A. J. Saddington, R. D. Knowles, and K. Knowles. Laser doppler anemometry measurements in the near-wake of an isolated formula one wheel. *Experiments in Fluids*, 42(5):671, Mar 2007.

[12] Issakhanian E, Elkins CJ, Lo K, and Eaton JK. An experimental study of the flow around a formula one racing car tire. *ASME. J. Fluids Eng.*, 2010.

[13] A. J. Sprot, D. B. Sims-Williams, and R. G. Dominy. The aerodynamic charac-

teristics of a fully deformable formula one wind tunnel tyre. *SAE Int. J. Passeng. Cars - Mech. Syst.*, 5:1026–1041, 04 2012.

[14] Ioannis Dimitriou and Sven Klussmann. Aerodynamic forces of exposed and enclosed rotating wheels as an example of the synergy in the development of racing and passenger cars. In *SAE Technical Paper*. SAE International, 04 2006.

[15] Lee Axon, Kevin Garry, and Jeff Howell. The influence of ground condition on the flow around a wheel located within a wheelhouse cavity. In *SAE Technical Paper*. SAE International, 03 1999.

[16] John Fabijanic. An experimental investigation of wheel-well flows. In *SAE Technical Paper*. SAE International, 02 1996.

[17] Per Elofsson and Mark Bannister. Drag reduction mechanisms due to moving ground and wheel rotation in passenger cars. In *SAE Technical Paper*. SAE International, 03 2002.

[18] Lee Axon. *THE AERODYNAMIC CHARACTERISTICS OF AUTOMOBILE WHEELS - CFD PREDICTION AND WIND TUNNEL EXPERIMENT*. PhD thesis, College of Aeronautics, Cranfield University, 1999.

[19] S KrajnoviÄ, Sasan Sarmast, and Branislav Basara. Numerical investigation of the flow around a simplified wheel in a wheelhouse. *Journal of Fluids Engineering*, 133(11):111001, 2011.

[20] Attila Schwarczkopf, Tamás Régert, and Tamás Lajos. Investigation of simple possibilities for reduction of drag due to the wheels of road vehicles. 2009.

[21] Christoffer Landström, Tim Walker, and Lennart Löfdahl. Effects of ground simulation on the aerodynamic coefficients of a production car in yaw conditions. In *SAE Technical Paper*. SAE International, 04 2010.

[22] Emmanuelle Thivolle-Cazat and Patrick Gilliéron. Flow analysis around a rotating wheel. In *13th Int. Symposium on Applications of Laser Techniques to Fluid Mechanics, Lisbon, Portugal*, pages 26–29, 2006.

[23] András Gulyás, Ágnes Bodor, Tamas Regert, and Imre M. Jánosi. Piv measurement of the flow past a generic car body with wheels at les applicable reynolds number. *International Journal of Heat and Fluid Flow*, 43(Supplement C):220 – 232, 2013. 7th International Symposium on Turbulence Heat and Mass Transfer (THMT-7), Palermo Conference on Modelling Fluid Flow (CMFF'12).

[24] CJ Baker. The turbulent horseshoe vortex. *Journal of Wind Engineering and Industrial Aerodynamics*, 6(1-2):9–23, 1980.

[25] Jigen Zhou, Ronald J Adrian, S Balachandar, and TM Kendall. Mechanisms for generating coherent packets of hairpin vortices in channel flow. *Journal of fluid mechanics*, 387:353–396, 1999.

[26] Thomas Lutz. *The effect of the boundary layer present in wind tunnels on the aerodynamic drag of a model truck*. PhD thesis, University of Cape Town, 1997.

[27] N Gregory and WS Walker. *Experiments on the Use of Suction through Perforated*

Strips for Maintaining Laminar Flow: Transition and Drag Measurements. HM Stationery Office, 1958.

[28] M Gad-el Hak. Flow control: Passive, active, and reactive flow management. 2000.

[29] Antonello Cogotti. A parametric study on the ground effect of a simplified car model. In *SAE Technical Paper*. SAE International, 02 1998.

Appendix A

Boundary layer suction

It has been shown from literature that wheel rotation is important to study the flow inside the wheelhouse, mainly due to the significant changes in the flow field caused by wheel rotation, especially the jetting vortices that are present only in a rotating wheel. One of the means of achieving wheel rotation is to employ a moving belt system. The moving belt system ensures that there is either no boundary layer growth on the ground plane or is kept to a minimum without additional growth. Typically, in a wind tunnel facility the moving ground plane starts at a certain distance from the inlet of the wind tunnel. The distance upto this inlet has stationary floor which enables the development of boundary layer. This boundary layer needs to be removed before entering the moving ground plane and a common means of removing this boundary layer are boundary layer suction, tangential blowing and distributed suction system. Unlike boundary layer suction and tangential blowing, which are present just ahead of the moving ground plane, distributed suction system is present in the moving ground plane itself. Through these methods, the boundary layer, that had previously developed ahead of the moving ground plane, can be removed effectively or its growth controlled.

A.1 Effect of boundary layer growth

An investigation into the effect of boundary layer growth on the flow has already been studied by Dimitriou and Klussmann [14]. The configuration tested included rotating wheel with grooves. Their observations were that without the boundary layer suction the amount of mass flow coming into contact with the tire is reduced resulting in the formation of a thicker boundary layer on the wheel, especially at the top as shown in Figure A.1. As a consequence, higher base pressures were recorded, which lowered the drag values compared to the case with boundary layer suction.

Even though the investigation involved moving ground plane, it is evident that removing the boundary layer that developed ahead of the moving ground plane is necessary in obtaining accurate information on the flow field.

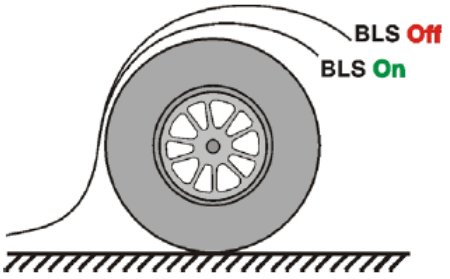

Figure A.1: Boundary layer suction effect [14]

A.2 Boundary layer suction design

For the present investigation, the water tunnel facility available at the Aero and Hydrodynamics Laboratory at TU Delft is used to study the flow field. In the water tunnel facility, a moving belt for the ground plane is not present and hence a stationary ground plane is used. Therefore alternate means have to be made use of to remove the boundary layer growth on the stationary ground. For this purpose, a ground plane with multiple rows of perforations to remove the boundary layer growth was considered. This is equivalent to the distributed suction system mentioned earlier.

The design of this ground plane is shown in Figure A.2. This design has been adopted from the work of Thomas Lutz [26], from his investigation of boundary layer effects on wind tunnels. Gregory and Walker [27] showed that with three or more rows of perforation, the ratio of pitch (distance between holes) to diameter of the holes should not exceed 3, in order to extend the region of laminar flow. This ratio has been found to hold good upto free stream speeds of 180 ft/sec.

The next criteria to be considered is the suction velocity. The velocity profile in the viscous region has been found to be asymptotic and exponential if the suction applied at the wall is such that the flow outside the boundary layer is undisturbed [28].

$$\frac{u}{U_\infty} = 1 - e^{\frac{-v_w y}{\nu}} \tag{A.1}$$

v_w in the above equation refers to the suction velocity at the wall, ν is the kinematic viscosity and y is the distance from the wall.

The displacement thickness, given in Equation A.2 in this region is found to be a constant value given by the ratio of kinematic viscosity to the suction velocity at the wall.

$$\delta^* = \int_0^\infty (1 - \frac{u}{U_\infty}) dy \tag{A.2}$$

Substituting Equation A.1 in Equation A.2 we get,

$$\delta^* = \frac{\nu}{v_w} \tag{A.3}$$

The critical Reynolds number based on this asymptotic velocity profile and displacement thickness has been found to be 70,000 [28]. Substituting the displacement thickness equation into this critical Reynolds number, one obtains the ratio of suction velocity to the freestream velocity to be greater than 1.4 x 10^{-5}. However, the typical ratio of velocities used lie in the range of 0.0001 - 0.01 as in this range, the assumptions of boundary layer theory remain valid [28].

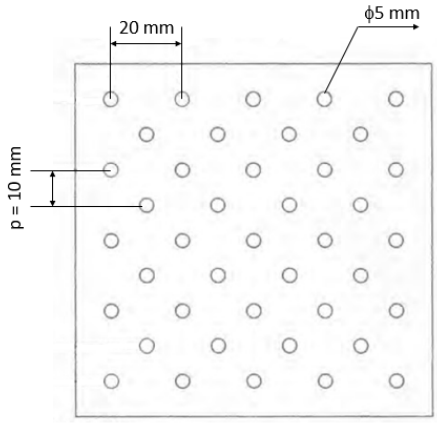

Figure A.2: A section of the ground plane with perforations for suction [26]

It is also claimed as a general rule of thumb, to ensure boundary layer stability, that the Reynolds number based on hole diameter and suction velocity should be kept below 10. However, it is also mentioned in [28] that stability of flow has been achieved with suction velocity an order of magnitude higher. Therefore for the present design considered, the ratio of velocity was chosen to be 0.01 which gave a Reynolds number based on hole diameter of 50. Lutz [26] employed the configuration shown in Figure A.2, that satisfied the criteria established by different authors and found satisfying results. The boundary layer approaching the model was reduced by 56% while the boundary layer displacement thickness was reduced by 89%.

The design discussed above has not been used for this investigation because to ensure that the suction is uniformly distributed, a validation study must be conducted. This would support the fact that the suction rate is the same across all the holes and that the suction system does not affect the flow outside the boundary layer or create unwanted disturbances to the flow especially near the wheel. However, due to time constraints this concept is left at design stage and a ground plane without any boundary layer suction would be used instead.

Appendix B

Effect of rotating wheel and stationary ground

A stationary ground is used for the present investigation along with rotating wheel. It is therefore important to establish the differences that one can expect having this configuration compared to rotating wheel and moving ground or stationary wheel and stationary ground.

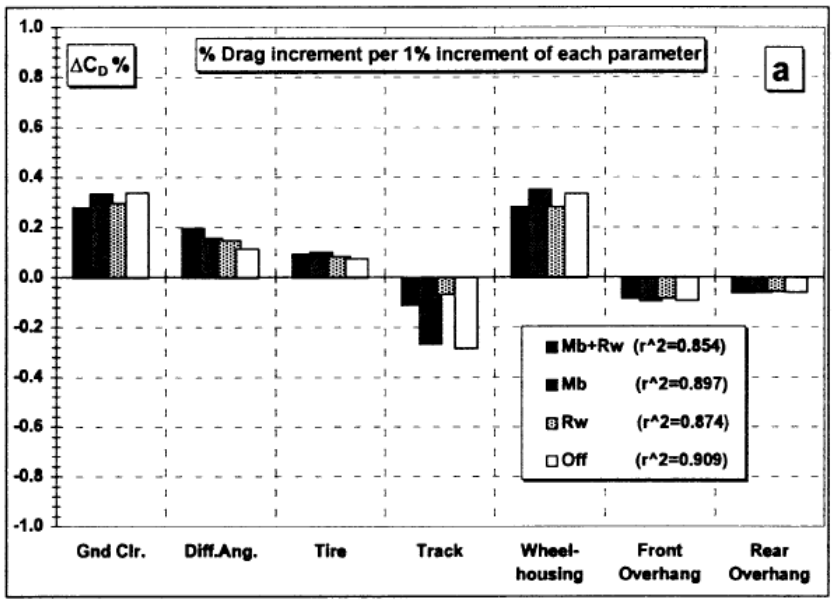

Figure B.1: Effect of different configurations on different parameters [29]. Mb+Rw refers to moving ground and rotating wheel, Mb refers to moving ground alone, Rw refers to rotating wheel alone and Off refers to stationary ground and stationary wheel

The effect of different configurations, namely moving ground and rotating wheels, moving ground only, rotating wheel only and completely stationary system have been investigated by Cogotti [29] in his parametric study on simplified car body under ground effect. It was found that when the different parameters, such as ground clearance, wheelhouse size etc., were increased by 1% the drag values were over-estimated

by the completely stationary configuration compared to moving ground and rotating wheels configuration. This is expected due to the smaller wake structures in the case of rotating wheel compared to the stationary wheel. By achieving wheel rotation alone without moving ground, Cogotti found the simulation to improve compared to the stationary configuration conditions. On some occasions, however, it was found to over-correct the values estimated under stationary configuration. This is shown in Figure B.1 where the over correction could be observed for the 'Track' parameter. Similar effect was observed for the lift values as well.

This led Cogotti to conclude that if a complete simulation is not possible i.e. having a moving ground and rotating wheel, the next best configuration was to have a completely stationary system i.e. stationary wheel and ground.

However, in this present investigation, a parametric study is not being undertaken and previous studies from literature have shown that wheel rotation is the dominating factor [17] in determining the flow field inside the wheelhouse. Therefore, it has been decided to employ rotating wheel and stationary ground configuration with the understanding that differences exist between the current configuration and having a moving ground configuration. Moreover, this configuration would still provide provide useful information that could be used to validate LES results. Also, to study the effect of VG on the jetting vortices, wheel rotation is important since jetting vortices are observed only in the case of rotating wheel.

Appendix C

Wake velocity profiles for *Case2*

The velocity profiles at different distance downstream of the wheel for *Case2* are presented here.

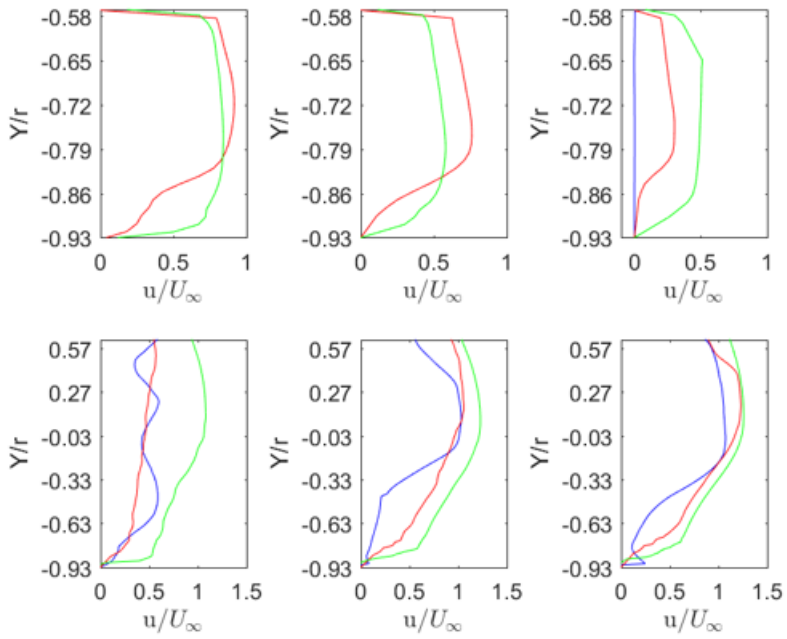

Figure C.1: Scaled u velocity along the different lines indicated earlier for Re = 72000. The blue line corresponds to x/d = 0.6, red line corresponds to x/d = 1 and green line corresponds to x/d = 1.5. Refer Figure 4.14 for numbering.

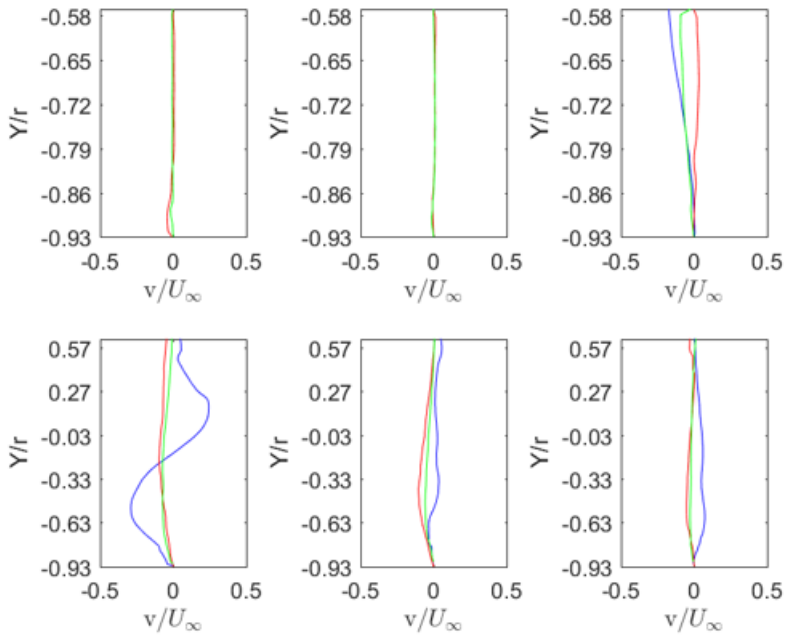

Figure C.2: Scaled v velocity along the different lines indicated earlier for Re = 72000. The blue line corresponds to x/d = 0.6, red line corresponds to x/d = 1 and green line corresponds to x/d = 1.5. Refer Figure 4.14 for numbering.

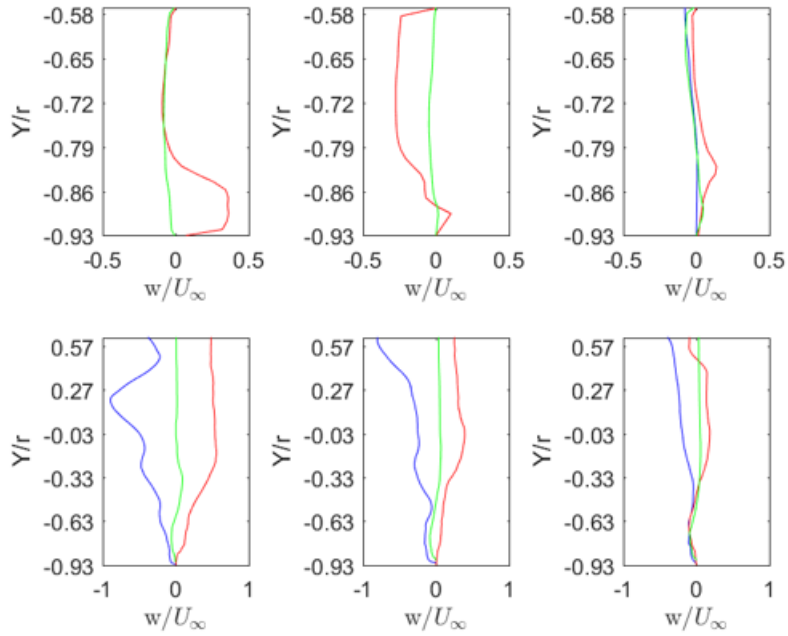

Figure C.3: Scaled w velocity along the different lines indicated earlier for Re = 72000. The blue line corresponds to x/d = 0.6, red line corresponds to x/d = 1 and green line corresponds to x/d = 1.5. Refer Figure 4.14 for numbering.

Appendix D

Wake velocity profiles for *Case2* with Vortex Generator

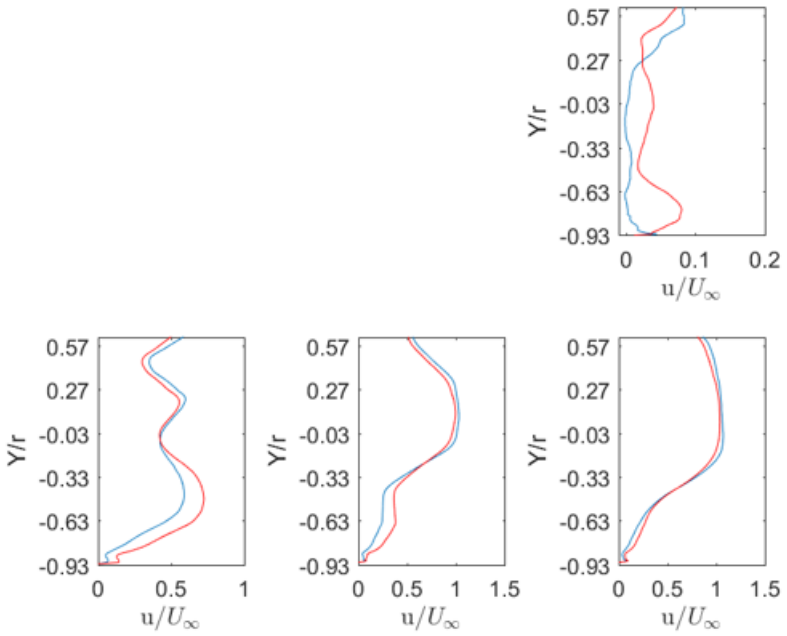

Figure D.1: u velocity along the different lines indicated earlier for $Re = 72000$ at $X/D = 0.6$. The blue line corresponds to the measurement without VG and the red line corresponds to the measurement with VG. Refer Figure 4.14 for numbering.

Figures D.1- D.3 shows the comparison of the three components of velocity along the different lines for *Case2*. It can be seen from these figures that the velocity profiles are almost similar along the different lines in both the configurations. Thus, the addition of VG did not have any effect on the flow. This is in contrast to *Case1* where the addition of VG had a significant effect on the flow, especially on the streamwise and spanwise component of velocity. It is possible that due to the high velocity, the VG, which was glued to the body, might not have withstood the force and hence had no effect on the flow behavior.

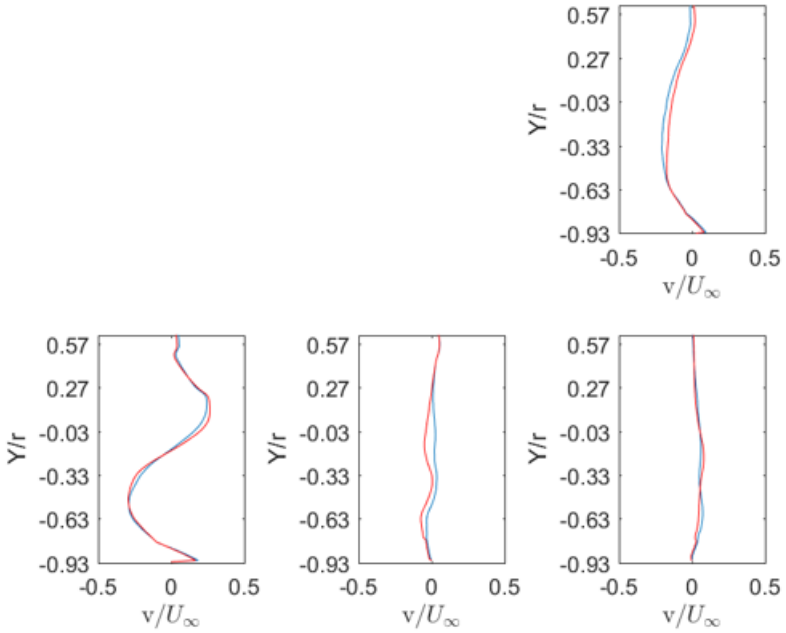

Figure D.2: v velocity along the different lines indicated earlier for $Re = 72000$ at $X/D = 0.6$. The blue line corresponds to the measurement without VG and the red line corresponds to the measurement with VG. Refer Figure 4.14 for numbering.

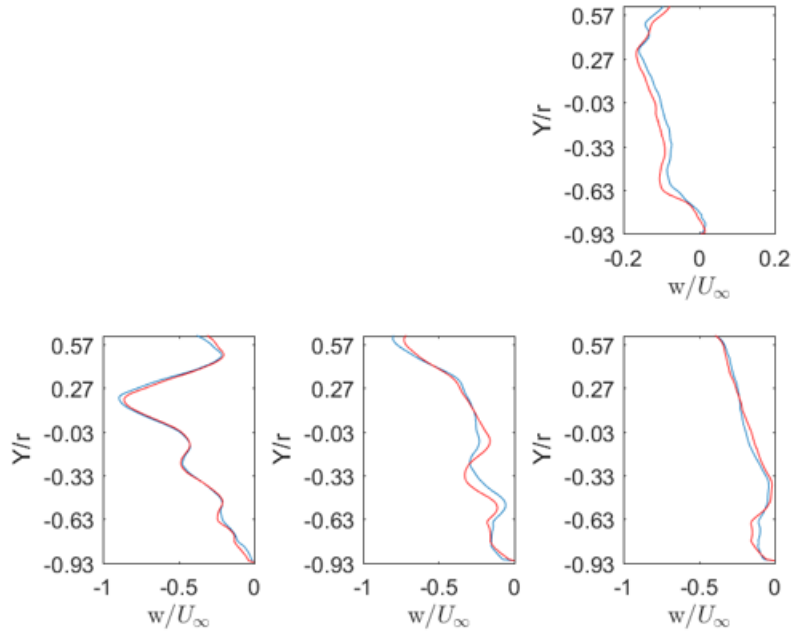

Figure D.3: w velocity along the different lines indicated earlier for $Re = 72000$ at $X/D = 0.6$. The blue line corresponds to the measurement without VG and the red line corresponds to the measurement with VG. Refer Figure 4.14 for numbering.